

國立交通大學

材料科學與工程學系

博士論文

聚亞醯胺發光二極體及奈米複合材料之  
合成與特性研究

Synthesis and Characterization of Polyimide Light-  
Emitting Diodes and Nanocomposites

研究生：徐守謙

指導教授：黃華宗 博士

中華民國九十五年七月

*To my family and ray-ray  
with gratitude.....*



# 聚亞醯胺發光二極體及奈米複合材料之合成與特性研究

## 摘要

顯示和奈米科技是近年來不管在基礎學科或高科技產業中相當熱門的兩個課題。本論文將分成兩個部分，共七個章節，針對聚亞醯胺之發光二極體及奈米複合材料的特性（2-5 章），和一維奈米材料的製備兩個主題做深入的研究（6,7 章）。

首先在第二章為 BAO 系列聚亞醯胺發光二極體特性研究。所有合成的 BAO 系列聚亞醯胺玻璃轉化溫度皆大於 250°C，5 wt.-% 熱裂解溫度也大於 510°C，顯示良好的熱安定性及機械性質。這些聚亞醯胺也均有螢光特性，而且螢光強度跟分子鏈的排列有密切的關係。進一步將合成之聚亞醯胺製作成單層發光二極體元件，只有 BAO-ODPA 和 BAO-6FDA 兩種聚亞醯胺觀察到電致發光性質，BAO-PMDA 和 BAO-BPADA 兩種聚亞醯胺可能因薄膜均勻性太差導致原件短路。另外，BAO-ODPA 在雙層發光二極體元件中（ITO/PPV-PVA/PI/Al）也具有好的電子傳輸及電洞阻障的功能，可將 PPV-PVA 發光效率提高兩個級數。

第三章為利用真空蒸鍍聚合製備以 BAO-6FDA 和 BAPF-6FDA 兩種聚亞醯胺為發光層之單層發光二極體。利用真空蒸鍍聚合，聚亞醯胺薄膜的厚度可降低至 150 Å，兩種聚亞醯胺二極體元件也都表現出 4.5V 和 6.5V 相當低的啟動電壓。經由原子力顯微鏡的分析，BAO-6FDA 和 BAPF-6FDA 兩種聚亞醯胺薄膜皆有良好的表面平整度，分別為 8.8 Å 和 4.7 Å。BAO-6FDA 發光二極體具有較寬的電致發光頻譜，其範圍從 400 nm 到 700 nm。而 BAO-BAPF 發光二極體則表現出較佳的發光效率，這可能是因為較平衡的電子/電洞注入及較強的分子間電荷轉移作用。

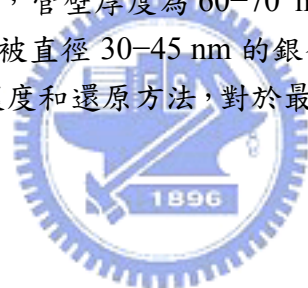
第四章敘述聚亞醯胺/ZnO 奈米混成膜的製備與特性。PMDA-ODA 和 BTDA-ODA 兩種不同柔軟度的聚亞醯胺作為高分子基材進行研究。經由 FTIR 和 XPS 的分析，推斷 ZnO 表面的 OH 基和聚亞醯胺的 C=O 官能基會形成交鏈，進而提升混成膜的熱和機械性質。另外，穿透式電子顯微照片說明，ZnO 奈米粒子分散在較剛硬的 PMDA-ODA 聚亞醯胺，粒子尺寸會大於分散在較柔軟的 BTDA-ODA 聚亞醯胺中。

第五章為利用蒸鍍/氧化二段法大量製備 ZnO 奈米單晶粒子於石英及聚亞醯

胺基材上。蒸鍍後的 Zn 金屬在 350°C 熱風循環機進行氧化 2 小時，可完全轉變成透明的 ZnO。經由高解析度 TEM 觀察，製備的 ZnO 奈米粒子為晶格規則排列的單晶結構，並無晶格缺陷，並顯示出一 395 nm 的紫外光發光特性。

第六章敘述 oleic acid/1-decanol/ammonium hydroxide 三相系統的 inverse hexagonal ( $H_{II}$ ) 液晶相的製備與特性。 $H_{II}$ 相位於此三相圖的中央，由 21/55/24, 28/27/45 和 62/5/33 (oleic acid/1-decanol/ammonium hydroxide) 三點組成的三角形區域。在此 $H_{II}$ 相區域中，隨著 1-decanol 含量的減少液晶消失溫度 (isotropic temperature) 變化從 55°C 到 142°C。經由 XRD 分析，推斷製備的 $H_{II}$ 相的圓柱直徑為 4–4.4 nm，內部水相直徑為 1–1.4 nm。在此三相系統中，ammonium hydroxide 的含量提高至 45 wt.-%，及摻入多種金屬離子，如  $Ag^+$ ,  $Cu^{2+}$ ,  $Ni^{2+}$ ,  $Co^{2+}$ ,  $Zn^{2+}$ , 和  $Cd^{2+}$ ，皆不會破壞原本規則的 $H_{II}$ 相。

本論文第七章敘述利用先合成的管狀銀離子先驅物，在室溫下即時還原製備銀奈米電纜 (nanocable)。經由 FTIR 分析，推論配位的銀離子錯合物形成交鏈，自身聚集，進而促成管狀先驅物的形成。此銀離子管狀先驅物長度達數微米，外徑為 155–200 nm，徑/長比，管壁厚度為 60–70 nm。經甲醛還原後，原本管狀先驅物的中空部份，均勻的被直徑 30–45 nm 的銀奈米線所填充，形成奈米電纜結構。還原條件，如還原劑濃度和還原方法，對於最後產物的型態有很大的影響。



# Synthesis and Characterization of Polyimide Light- Emitting Diodes and Nanocomposites

## Abstract

---

Display and nano technologies are two hottest topics in recent years not only in academic research but in high-tech industry. This thesis is divided into two parts to investigate the characterization of polyimide (PI)-based light emitting diodes (LED) and nanocomposites (*chapter 2–5*), and the preparation of one-dimensional nanostructures (*chapter 6, 7*).

*Chapter 2* describes the characteristics of a single layer and a double layer 2,5-Bis(4-aminophenyl)-1,3,4-oxadiazole (BAO)-based LED. All the resultant PIs possess high glass transition temperatures ( $>250^{\circ}\text{C}$ ) and high decomposition temperatures of 5 wt.-% weight loss ( $T_{\text{d}}$ ,  $>510^{\circ}\text{C}$ ). They also show obviously fluorescent characteristic, and the intensity is related to the arrangement of the molecular chains. Electroluminescent (EL) spectra were detected by using BAO-ODPA and BAO-4,4'-(hexafluoroisopropylidene)diphthalic anhydrid (6FDA) as an emitting layer in a single LED device. In addition, in the double layer LED device, ITO/PPV-PVA/BAO-ODPA/Al, BAO-ODPA can be used as an excellent electron transport and electron/hole blocking layer, a significant improvement in the EL efficiency by two order of magnitude.

In *chapter 3* presents that BAO and 4,4'-(9-Fluorenylidene)dianiline (BAPF) reacting with 6FDA were carried out by using vapor deposition polymerization (VDP) for single layer LED devices. The thickness of the PI thin film can be reduced to  $150\text{\AA}$ , and both PI-LEDs show low threshold voltages, 4.5V and 6.5V for BAO-6FDA and BAPF-6FDA LEDs, respectively. The root mean square of the surface roughnesses of the BAO-6FDA and BAPF-6FDA thin films are  $8.8\text{\AA}$  and  $4.7\text{\AA}$ , respectively, which are far smaller than that of wet coating process. The BAO-6FDA LED emits a broader EL band, covering the full range of visible light (400 nm to 700 nm), than the BAPF-6FDA LED. While the electroluminescent efficiency of BAPF-6FDA LED is higher than BAO-6FDA LED, it may suggest the better balance on holes and electrons injection in the former and better intermolecular charge transfer.

*Chapter 4* reports the study of a series of PI/ZnO nanohybrid films with different ZnO contents, which prepared by a rigid pyromellitic dianhydride (PMDA)-4,4'-diaminodiphenylether (ODA) and a flexible 3,3',4,4'-benzophenonetetracarboxylic acid dianhydride (BTDA)-ODA PI matrixes. Analyses of Fourier transform infrared (FTIR) and X-ray photoelectron spectroscopy depict that the ZnO nanoparticles function as a physical crosslinking agent with PI chains through hydrogen bonding between the OH on the ZnO surfaces and the C=O of the imide groups. This crosslink causes the enhancement of thermal and mechanical properties of the hybrid films. Transmission electron microscopy (TEM) images reveal that the rigid matrix induces larger ZnO particle size (30–40 nm) compared the flexible matrix (10–15 nm).

In chapter 5 describes an efficient evaporation/oxidation two-step approach to massive prepare ZnO nanocrystals on quartz and flexible PI film. Evaporated metallic Zn can quickly transform into transparent ZnO via low temperature oxidization at 350 °C for 2h in air-circulating. TEM images show that the singular ZnO nanocrystals without stacking faults were obtained. Deposited ZnO on PI film substrates can obtain individual and well distribution nanocrystals with average crystal size is 20-30 nm. In photoluminescence measurement, the produced ZnO nanocrystals exhibit strong UV emission at 395 nm, and no visible emission was detected.

*Chapter 6* presents the ternary system oleic acid/1-decanol/ammonium hydroxide exhibiting an inverse hexagonal (H<sub>II</sub>) liquid crystalline phase, which exists between the compositions 21/55/24, 28/27/45, and 62/5/33 (oleic acid/1-decanol/ammonium hydroxide). The isotropic temperature increases from 55 °C to 142 °C with decreasing 1-decanol content. X-ray diffraction reveals interdigitated columns of 4–4.4 nm diameter with an internal water channel of 1–1.4 nm diameter. The system can tolerate up to 45 wt-% of ammonium hydroxide before the hexagonal phase collapses and can be doped with up to 0.1 mM concentrations of metals such as Ag<sup>+</sup>, Cu<sup>2+</sup>, Ni<sup>2+</sup>, Co<sup>2+</sup>, Zn<sup>2+</sup>, and Cd<sup>2+</sup>.

*Chapter 7* describes a simple and efficient method to *in situ* fabricate silver nanocables at room temperature from a self-assembling tubular silver precursor. FTIR spectroscopy revealed that the organic sheath to be crosslinked via bridging-type coordination to the silver ions, which helps in the formation of the tubular aggregation. The length of these tubular precursors is in the order of several microns, with outer diameters of 155–200 nm. The wall thickness is 60–70 nm. After reduction, a sharp contrast between sheath and core can be clearly observed in the TEM micrograph.

The cores are straight and uniform with diameter of 30–45 nm. In addition, properly control of the reaction condition, such as reagent concentration and method of reduction, is important to obtain well-defined nanocables.



## 誌 謝

指導教授

黃華宗 教授

除了研究上的教導，黃老師更是一位理想的傾聽者，六年多的循循善誘，學生由衷感激。

口試委員

周卓輝 教授、韋光華 教授、楊長謀 教授、許聯崇 副教授

感謝各位老師在學生論文口試的指導與建議。

交大光電所

許根玉 教授

感謝許老師在推薦信上的美言，讓學生得以獲得 2004 三明治計畫獎學金，順利赴德研究。

DWI an der RWTH Aachen  
Germany

Prof. Dr. Martin Möller, Dr. Oliver Weichold

PD Dr. Uwe Beginn, Prof. Dr. Dimitri A. Ivanov, Dr. Ahmed Mourran, Dr. Kim-Hô Phan, Dr. Xiaomin Zhu

Yvonne Noppeney, Heidrun Keul, Linglong Yan, Irene Colicchio, Stephan Rütten

Thomas, Pooja, Britta

I appreciate your assistance during my study in DWI. A special thanks goes to my supervisor Dr. Oliver Weichold for his guidance, understanding and patience, for his encouragement and support at all levels.

駐德科技組

胡昌智組長、彭雙俊組長、淑娟姐、程芝姐、張秘書

你們就像我在德國的家人，一年半的國外生活，有你們的照料及精神上的鼓勵與支持，讓我得以堅強。

交大學長姐

慶勳學長、美慧學姐、金賢學長、男哥、佩君學姐、吳聲昌學長、旭昌、泰翔、施文慈學姐、田運宜學長、良佑、Mickey、小豬、小嘉學長、德富學長、惠晶學姐、蔡欣瑩小姐、黃昆平學長

你們在研究領域的專業，學弟仰之彌高；與老闆過招的種種情節，學弟百聽不厭。感謝你們一路上的經驗分享，讓學弟不致重蹈覆轍。



交大同學

孝蔚、黃俊清、阿家、淑慧、汪立亨、邱麗娟

每每想起交大生活，最難忘的就是那段一起當菜鳥日子，這麼多年過去，始終如此。

學弟學妹

治明、博仁、國倫、柏霖、育生、佩盈、玉芳、彥文、國容、惟升、

育銓、雅婷、昭業、中彬、老周、耀德、阿茂

學長需要你們的時候，你們都在。感謝你們給我充分的尊重與實驗上適時的協助。實驗室有你們，變的好好笑………^\_^

三明治同學

日新、敏綺、宏宜、名瑩、立鼎、衍志、小敏、其璜、美瑤、美怡、

醇鴻、正恩、文威、Céline、至玟、騰合

一個意外的緣分讓大家在德國相識，那段同甘共苦的日子，每天想都不會膩。

教會朋友

鄭姐、簡哥、焜哥

你們對信仰的執著及對我們的用心，實在令我感動。謝謝你們每週給實驗室所有成員及我們家人的祝福。



# Content

摘要.....	i
Abstract.....	iii
誌謝.....	vi
Content.....	viii
Figure list.....	xi
Table list.....	xv
<b>Preface.....</b>	<b>1</b>
<b>Chapter 1 Literature Review: Preparation and Characterization of Polyimides.....</b>	<b>5</b>
1.1 Preparation.....	6
1.1.1 Two-step method.....	6
1.1.2 One-step method.....	13
1.1.3 Vapor deposition polymerization.....	13
1.2 Characterization.....	17
1.2.1 General charge transfer theory.....	17
1.2.2 Polyimide properties influenced by CT interactions.....	20
References.....	25
<b>Chapter 2 Electroluminescence and Electron Transport Characteristics of Aromatic Polyimides.....</b>	<b>28</b>
2.1 Introduction.....	29
2.2 Experimental section.....	30
2.2.1 Materials.....	30
2.2.2 Preparation of PI films.....	30
2.2.3 Devices fabrication.....	30
2.2.4 Characterization.....	31
2.3 Results and discussion.....	32
2.4 Conclusions.....	41
References.....	42
<b>Chapter 3 Vapor Deposition Polymerization of Aromatic Polyimides for Electroluminescent Devices.....</b>	<b>44</b>
3.1 Introduction.....	45

3.2	Experimental section.....	46
3.2.1	Materials.....	46
3.2.2	Vapor deposition polymerization.....	47
3.2.3	Characterization.....	47
3.3	Results and discussion.....	48
3.4	Conclusions.....	55
	References.....	56
<b>Chapter 4</b>	<b>Characterization of Polyimide/ZnO Nanohybrid Films.....</b>	<b>57</b>
4.1	Introduction.....	58
4.2	Experimental section.....	59
4.2.1	Materials.....	59
4.2.2	Synthesis of ZnO-TPM nanoparticles.....	59
4.2.3	Preparation of PI/ZnO nanohybrid films.....	59
4.2.4	Characterization.....	61
4.3	Results and discussion.....	61
4.4	Conclusions.....	70
	References.....	72
<b>Chapter 5</b>	<b>Fabrication of ZnO Nanocrystals by Evaporating Oxidizing Two-step Approach.....</b>	<b>73</b>
5.1	Introduction.....	74
5.2	Experimental section.....	74
5.3	Results and discussion.....	75
5.4	Conclusions.....	79
	References.....	81
<b>Chapter 6</b>	<b>Formation of Inverted Hexagonal Liquid Crystal in Mixtures of Amine-metal Hydroxides.....</b>	<b>82</b>
6.1	Introduction.....	83
6.2	Experimental section.....	84
6.2.1	Materials.....	84
6.2.2	Preparation of H <sub>II</sub> phase liquid crystals.....	84
6.2.3	Characterization.....	85
6.3	Results and discussion.....	85
6.4	Conclusions.....	91
	References.....	92

<b>Chapter 7</b>	<b>Preparation of Silver Nanocables from Self-assembling</b>	
	<b>Tubular Silver ion Precursors</b> .....	94
7.1	Introduction.....	95
7.2	Experimental section.....	95
	7.2.1 Materials.....	95
	7.2.2 Preparation of silver nanocables.....	96
	7.2.3 Characterization.....	96
7.3	Results and discussion.....	97
7.4	Conclusions.....	104
	References.....	105
	Summary.....	106
	Publication.....	109
	Curriculum vitae.....	110



# Figure list

## Preface

Figure 1	Chemical structure of Kapton H.....	1
----------	-------------------------------------	---

## Chapter 1 Literature Review: Preparation and Characterization of Polyimides

Figure 1.1	Chemical reaction of polyimide formation.....	6
Figure 1.2	Formation mechanism of poly(amic acid).....	7
Figure 1.3	Mechanism of thermal imidization.....	12
Figure 1.4	Schematic setup of vapor deposition system.....	14
Figure 1.5	Reaction mechanism for the formation of VDP polyimides.....	16
Figure 1.6	Orbital charge density for HOMO and LUMO in PMDA-ODA.....	18
Figure 1.7	Schematic diagrams for: (a) HOMO-LUMO and HOMO-second LUMO transitions; (b) CT emission in PMDA-ODA.....	19
Figure 1.8	Torsional angle $\omega$ and the intramolecular donor/acceptor nature of the polyimide.....	20
Figure 1.9	Fluorescence spectra of several commercial PI films (50 $\mu\text{m}$ thick) upon excitation at 300 nm.....	21
Figure 1.10	Photocurrent responses as a function of applied electric field for 7.5 $\mu\text{m}$ thick Kapton film and DMA-loaded Kapton film upon excitation at 480 nm.....	22

## Chapter 2 Electroluminescence and Electron Transport Characteristics of Aromatic Polyimides

Figure 2.1	Monomer structures and the synthesis route of poly(amic acid) and polyimides.....	31
Figure 2.2	Absorption spectra of the API films with 20 $\mu\text{m}$ thickness.....	34
Figure 2.3	Fluorescence spectra of the APIs films with 20 $\mu\text{m}$ thickness.....	35
Figure 2.4	WAXD patterns of the APIs films with 20 $\mu\text{m}$ thickness.....	35
Figure 2.5	Polyimide chain-chain interaction (a)CT interaction and (b)crystal..	36
Figure 2.6	Normalized electroluminescence spectra of the single layer API-LED device.....	37
Figure 2.7	Current density-voltage characteristic (closed mark) and EL intensity-voltage (open mark) for the single layer API-LED devices.....	37
Figure 2.8	EL efficiency of single layer API-LED devices.....	38
Figure 2.9	Normalized electroluminescence spectra of the LED devices.....	39

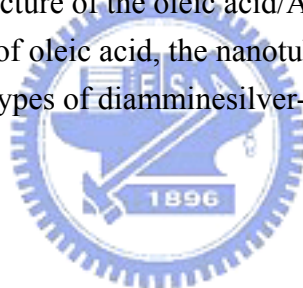
Figure 2.10	EL efficiency of the LED devices: ITO/PPV–PVA/Al and ITO/PPV–PVA/BAO–ODPA/Al.....	39
Figure 2.11	Band diagram of ITO/PPV–PVA/BAO–ODPA/Al LED device.....	40
<b>Chapter 3</b>	<b>Vapor Deposition Polymerization of Aromatic Polyimides for Electroluminescent Devices</b>	
Figure 3.1	Monomer structures and the preparation route of PIs.....	46
Figure 3.2	FT-IR spectra of PI thin films (a) BAO–6FDA and (b) BAPF–6FDA before and after imidization.....	48
Figure 3.3	Surface morphologies of the PI thin films (800Å) (a) BAO–6FDA and (b) BAPF–6FDA by vapor deposition; (c) BAO–6FDA by wet coating.....	49
Figure 3.4	UV–Vis absorption spectra of BAO–6FDA and BAPF–6FDA PI thin films.....	50
Figure 3.5	Electroluminescent spectra of PI–LED devices: ITO/BAO–6FDA/Al and ITO/BAPF–6FDA/Al.....	51
Figure 3.6	(a) Current density-voltage and (b) brightness-voltage characteristics of PI-LED devices ITO/BAO-6FDA/Al with different PI thickness: 150Å, 300Å and 600 Å.....	52
Figure 3.7	(a)Current density-voltage and (b)brightness-voltage characteristics of PI-LED devices ITO/BAPF-6FDA/Al with different PI thickness: 150Å, 300Å and 600Å.....	52
Figure 3.8	Brightness-current density characteristics of PI-LED devices with different PI thickness.....	53
Figure 3.9	Cyclic voltammograms of polyimides (a) oxidation curves (b) reduction curves.....	54
Figure 3.10	Band diagrams of ITO/BAO-6FDA/Al (left) and ITO/BAPF-6FDA/Al (right).....	54
<b>Chapter 4</b>	<b>Characterization of Polyimide/ZnO Nanohybrid Films</b>	
Figure 4.1	Monomer structures and the synthetic route of PI/ZnO hybrid films.....	60
Figure 4.2	FT-IR spectra of BTDA–ODA/ZnO hybrid films.....	62
Figure 4.3	XPS wide-scan spectrum of BTDA–ODA/ZnO 5 wt.-% film.....	62
Figure 4.4	Thermal gravimetric profiles of unmodified ZnO nanoparticles and TPM–stabilized ZnO nanoparticles.....	63
Figure 4.5	Zn 2p core-level spectra of various BTDA–ODA/ZnO hybrid films With different ZnO content.....	64

Figure 4.6	Illustration of the interaction between ZnO nanoparticles and PI chains.....	64
Figure 4.7	Dynamic mechanical storage moduli of BTDA–ODA/ZnO and PMDA–ODA/ZnO hybrid films.....	66
Figure 4.8	Dynamic mechanical tan $\delta$ curves of the PI/ZnO hybrid films BTDA–ODA/ZnO and PMDA–ODA/ZnO.....	66
Figure 4.9	Deconvolution of tan $\delta$ curves of BTDA–ODA/ZnO nanohybrid films...	67
Figure 4.10	Dynamic thermal gravimetric profiles of BTDA–ODA/ZnO and PMDA–ODA/ZnO nanohybrid films.....	68
Figure 4.11	TEM images of (a) TPM–stabilized ZnO nanoparticles (b) BTDA–ODA/ZnO–5 wt.-%, and (c) PMDA–ODA/ZnO–5 wt.-% hybrid films.....	69
<b>Chapter 5</b>	<b>Fabrication of ZnO Nanocrystals by Evaporating Oxidizing Two-step Approach</b>	
Figure 5.1	XRD pattern of ZnO samples as-deposited and after oxidized at 350 °C for 2h.....	76
Figure 5.2	Top view (a–c) and side view (d–e) FE-SEM images of the ZnO samples fabricated on quartz substrate at three different deposition time 2 min, 5 min and 10 min, respectively, and then oxidized at 350 °C for 2 h.....	77
Figure 5.3	(a) Low magnification TEM image of the ZnO nanocrystals and high magnification TEM images (inset); (b) HRTEM image and the SAED patten (inset).....	78
Figure 5.4	(a) FE-SEM images of the ZnO samples fabricated on PI substrates; (b) TEM image of the same sample.....	78
Figure 5.5	Room temperature PL spectra of the ZnO nanocrystals for deposited 10 min on quartz substrates.....	79
<b>Chapter 6</b>	<b>Formation of Inverted Hexagonal Liquid Crystal in Mixtures of Amine-metal Hydroxides</b>	
Figure 6.1	Phase diagram for the ternary mixture oleic acid/1-decanol/ ammonium hydroxide system at 25 °C.....	86
Figure 6.2	POM textures of oleic acid/1-decanol/ ammonium hydroxide (35/38/27) at (a) 70 °C and (b) 25 °C recorded during the cooling from $T_i$ (95 °C).....	87
Figure 6.3	X-ray diffraction patterns of oleic acid/1-decanol/ ammonium hydroxide solution (52/15/33) at (a) 25 °C and (b) 55 °C.....	88

Figure 6.4	Schematic representation of a three-dimensional network of the inverted hexagonal phase.....	89
------------	--	----

**Chapter 7      Preparation of Silver Nanocables from Self-assembling  
                         Tubular Silver ion Precursors**

Figure 7.1	Images of the dark-field optical microscopy for a diamminesilver-(I) oleate gel at a molar ratio of 30 before (a, b) and after (c) dispersion in ethanol.....	97
Figure 7.2	TEM micrographs (unstained) of a diamminesilver-(I) oleate gel at a molar ratio oleic acid/Ag <sup>+</sup> of 30 (a) and 50 (b-d).....	98
Figure 7.3	Bright-field TEM micrographs of nanocables after reduction of a gel with a molar ration oleic acid/Ag <sup>+</sup> of 50 (a-c) and a dark-field TEM micrographs (d, top) and the corresponding silver profile across the nanocable (d, bottom).....	99
Figure 7.4	TEM micrographs of the reduction products made by fast addition of KOH (a-c) and substituting NaBH <sub>4</sub> for formaldehyde (d).....	100
Figure 7.5	Schematic structure of the oleic acid/Ag <sup>+</sup> nanotube.....	101
Figure 7.6	FT-IR spectra of oleic acid, the nanotubes, and silver nanocables...	103
Figure 7.7	Coordination types of diamminesilver-(I) oleate.....	104





# *Table list*

<b>Chapter 1</b>	<b>Literature Review: Preparation and Characterization of Polyimides</b>	
Table 1.1	Electron affinity of aromatic dianhydrides .....	9
Table 1.2	Basicity $pK_a$ of diamines and their reactivities toward PMDA.....	9
<b>Chapter 2</b>	<b>Electroluminescence and Electron Transport Characteristics of Aromatic Polyimides</b>	
Table 2.1	Inherent viscosity of the PAAs and thermal properties of the APIs... 33	
<b>Chapter 3</b>	<b>Vapor Deposition Polymerization of Aromatic Polyimides for Electroluminescent Devices</b>	
Table 3.1	Electrochemical potentials and energy levels of the polyimides.....	55
<b>Chapter 4</b>	<b>Characterization of Polyimide/ZnO Nanohybrid Films</b>	
Table 4.1	Coefficient of thermal expansion of pure PI and PI/ZnO nanohybrid films.....	65
Table 4.2	Glass transition temperatures <sup>a</sup> of pure PI and PI/ZnO nanohybrid films.....	68
Table 4.3	Thermogravimetric analysis of pure PI and PI/ZnO nanohybrid films.....	69
<b>Chapter 6</b>	<b>Formation of Inverted Hexagonal Liquid Crystal in Mixtures of Amine-metal Hydroxides</b>	
Table 6.1	Phase behaviour of the ternary mixtures.....	87

# Preface

Polyimide (PI) is a class of representative high-performance polymer possessing cyclic imides and aromatic groups in the main chain. The most familiar PI is widely known as Kapton H<sup>®</sup> (Figure 1.1), which was first commercialized in early 1960s. Thereafter, a number of PIs have been synthesized and investigated extensively in aspects of structure and property relationships and applications<sup>[1,2]</sup>.

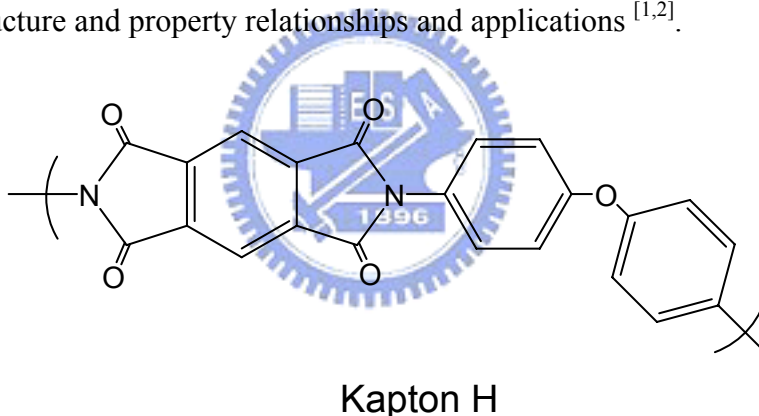


Figure 1.1 Chemical structure of Kapton H.

In general, PI is known to be thermally stable due to its heterocyclic imide rings on the backbone, and the thermal stability is further significantly improved by incorporating aromatic rings on the backbone and/or side groups. In addition to such high thermal stability, the nature of the chemical structure consisting rigid imide and aromatic rings always provides excellent mechanical and dielectric properties as well as high chemical resistance. Beyond these advantageous properties, a variety of functionalities, for instance, photoreactivity, molecular recognition ability, nonlinear optical responsibility, light-emitting ability and so on, can be added into the backbone and/or side groups of PIs, depending on their demands in applications<sup>[3]</sup>. Due to these advantageous properties and the functionalities, PIs have found diverse applications in the microelectronics, flat panel display, aerospace, and chemical and environmental

industries as flexible circuitry carriers, stress buffers, interdielectric layers, passivation layers, liquid crystal alignment layers, varnishing resins, fibers, matrix materials, and gas and chemical separation membranes<sup>[4-7]</sup>.

Display and nano technology are two hottest topics no matter in academic research or high-tech industries in recently years. To further understand the potential application of PI in these two fields, the first five chapters of this thesis work aims at the studies as shown below:

1. PI-based polymer light-emitting diodes
2. PI/ZnO nanocomposites

In *Chapter 1*, the state of the literature is summarized regarding the objective of this thesis. This chapter first highlights in different preparation methods of PIs, including two-step and one -step wet-chemical approach, vapor deposition polymerization, thermal and chemical imidization. The reaction mechanisms and the effect of monomers and experimental conditions are also described. The second part of this chapter focuses on the charge transfer in PIs and the influence on PI properties.

*Chapter 2* describes the newly synthesized 2,5-Bis(4-aminophenyl)-1,3,4-oxadiazole (BAO) based PIs. The relationship between the different dianhydride structures and molecular aggregation were studied by X-ray diffraction analysis, and the leading charge transfer interaction in PIs and the fluorescence behavior were also discussed. Furthermore, single layer and double layer PI based light-emitting diodes were prepared. The electron transport characteristics of the PIs and the device characteristics were further investigated.

In *Chapter 3* is focus on using vapor deposition polymerization to fabricate BAO/4,4'-(hexafluoro-iso-propylidene) diphthalic anhydride (6FDA) and 4,4'-(9-Fluorenylidene)dianiline (BAPF)/6FDA single layer light-emitting diode. A series of the device character are presented. The morphology and quality of PI films were observed by atomic force microscopy and compared with that prepared by wet chemical route. In addition, the effect of the diamine structure on device efficiency was discussed.

*Chapter 4* presents the study of the incorporation of ZnO nanocrystals in PI matrix in formation of PI/ZnO nanohybrid films. Two PIs with different rigidity, 3,3',4,4'-benzophenonetetracarboxylic acid dianhydride (BTDA)/

4,4'-diaminodiphenylether (ODA) and pyromellitic dianhydride (PMDA)/ODA, were used in this study. The thermal, mechanical and morphology characteristics of the hybrid films were established. Also the effect of PI structures on the variation of ZnO particle size, and the structural change of ZnO nanoparticles before and after thermal imidization were reported.

*Chapter 5* describes using a convenient thermal coater and an air-circulating to carry out thermal evaporation and oxidization processes, respectively, in formation of ZnO nanocrystals at low temperature on quartz and flexible PI film substrates. The structure and photoluminescence properties of the resultant ZnO nanocrystals are studied.

In addition, an additional research subject, which is about preparation of one-dimension nanomaterials, is incorporated in chapter 6 and 7. This is the research results when I gained the scholarship of 2004 NSC-DAAD Sandwich Program and worked in DWI an der RWTH Aachen, Germany, supervised by Oliver Weichold, in the last one and a half year of my PhD program.

*Chapter 6* presents the lyotropic liquid crystal that preferentially forms the inverted hexagonal phase by using ternary system consisting of oleic acid/1-decanol/ammonium hydroxide solution. Oleic acid was further replaced by stearic acid and elaidic acid in order to understand the effect of monomer structures on liquid crystalline phase. Besides, various metal ions, such as  $\text{Ag}^+$ ,  $\text{Cu}^{2+}$ ,  $\text{Ni}^{2+}$ ,  $\text{Co}^{2+}$ ,  $\text{Zn}^{2+}$ , and  $\text{Cd}^{2+}$ , were doped in the prepared the inverted hexagonal liquid crystalline phase. This inverted hexagonal phase system is suggested that may serve an easy route in preparation of nanorods and nanowires.

*In Chapter 7* describes a simple and efficient method to fabricate silver/oleic acid nanocables. The tubular diamminesilver (I) oleate which acted as template was prior prepared. And then directly reduced the tubular precursor by formaldehyde, the silver/oleic acid nanocables can be obtained. The reducing conditions and the molar ratio of oleic acid/silver ion show great influence on the morphology of the final products.

## References

---

- [1] M. K. Ghosh and K. L. Mittal, *Polyimides: Fundamentals and Applications*, Marcel Dekker: New York, 1996.
- [2] D. Wilson and P. Hergenrothe (Ed:H. D. Stenzenberger), *Polyimides*, Chapman & Hall, London, 1990.
- [3] Z. Ahmad, J. E. Mark. *Chem. Mater.* 2001, **13**, 3320.
- [4] M. J.M. Abadie, V. Y. Voytekunas, A. L. Rusanov. *Iranian Polym. J.* 2006. **15**. 65.
- [5] M. Ree, T. J. Shin, S. W. Lee. *Korea Polym. J.* 2001, **9**, 1.
- [6] M. Ree. *Macromol. Res.* 2006, **14**, 1.
- [7] Y. N. Sazanov. *Russ. J. Appl. Chem.* 2001, **74**, 1217.



# *Chapter 1*

**Literature Review:**

**Preparation and Characterization of Polyimides**



## 1.1 Preparation

Polyimides (PIs) are generally classified as soluble and nonsoluble polymers depending on their solubilities <sup>[1-3]</sup>. A few soluble aliphatic and aromatic PIs have been reported so far <sup>[4,5]</sup>. Most aromatic polyimides cannot be processed because they are insoluble and have a high glass transition temperature. Thus, they are first synthesized in a soluble precursor form and then processed in various ways, before finally being converted to PIs. Poly(amic acid) (PAA) and poly(amic dialkyl ester), which are representative soluble precursors, are usually processed first as a specific form depending on applications and then imidized in formation of PIs.

### 1.1.1 Two-step method

In the typical method of PI synthesis, a tetracarboxylic acid dianhydride is added to a solution of diamine in a polar aprotic solvent, such as *N*-methyl-2-pyrrolidone (NMP), dimethyl sulfoxide (DMSO), *N,N*-dimethylacetamine (DMAc), and *N,N*-dimethylformamide (DMF) at 15 to 75 °C <sup>[1]</sup>. The generated PAA is then cyclodehydrated to the corresponding PI by extended heating at elevated temperatures or by treatment with chemical dehydrating agents (Figure 1.1).

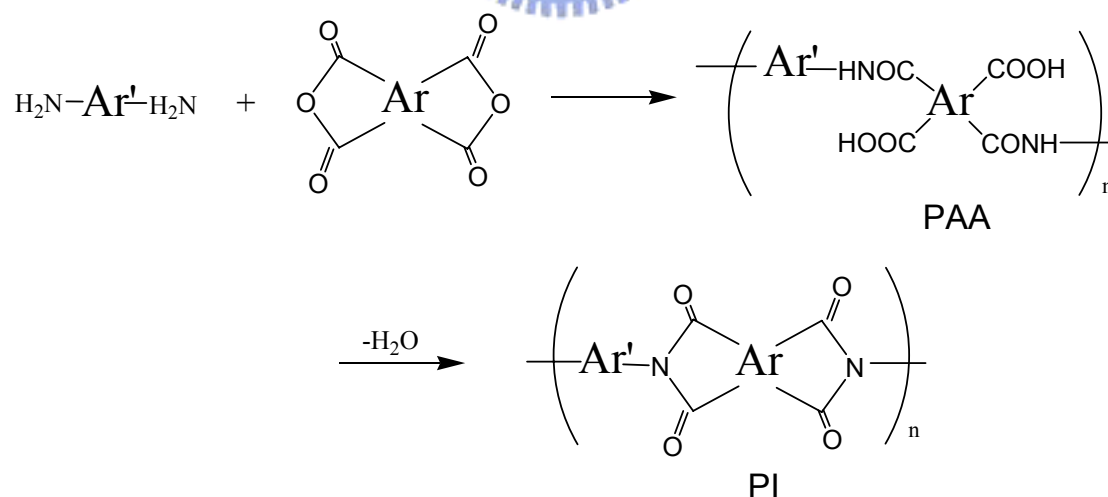


Figure 1.1 Chemical reaction of polyimide formation.

## Poly(amic acid)

The molecular weight of the resultant PAA has great influence on final PI's physical properties; simply speaking, higher PAA molecular weight possesses better PI physical properties<sup>[2]</sup>. The reaction mechanism of PAA formation involves the nucleophilic attack of the amino group on the carbonyl carbon of the anhydride group, followed by the opening of the anhydride ring to form amic acid group (Figure 1.2).

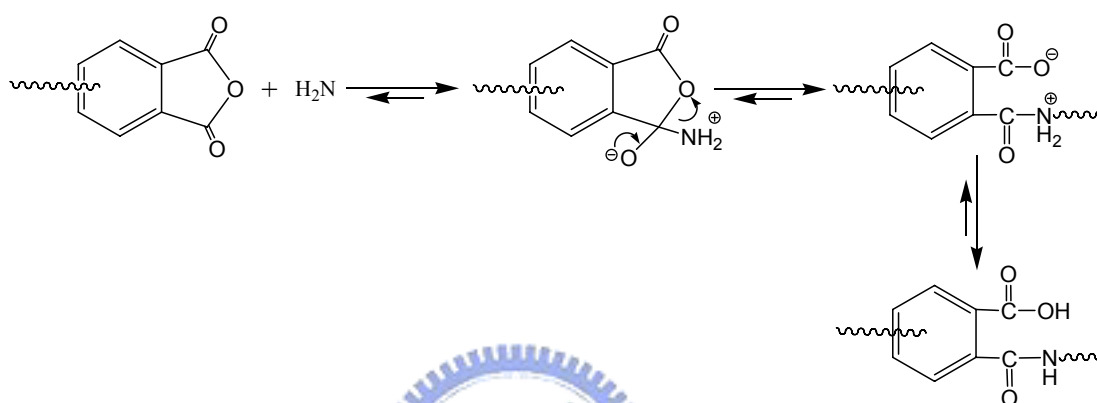


Figure 1.2 Formation mechanism of poly(amic acid)

The most important aspect of this process is that it is an equilibrium reaction<sup>[6]</sup>. Often it appears to be an irreversible reaction because a high molecular weight PAA is readily formed in most cases as long as pure reagents are used. This is because the forward reaction is much faster than the reverse reaction, often by several orders of magnitude. If the large reaction rate difference is not met, the high molecular weight PAA is not formed. Therefore, it is important to examine the driving forces that favor the forward reaction over the reverse reaction. It should be noted that the acylation reaction of amines is an exothermic reaction and that the equilibrium is favored at lower temperatures. The forward reaction in dipolar solvents is a second order reaction and the reverse reaction is a first order reaction. Therefore, the equilibrium is favored at high monomer concentrations to form higher molecular weight PAAs.

## Solvent effect

Solvents play an important role in the rate of PAA formation. The rate generally



increases as the solvent becomes more polar and more basic <sup>[7,8]</sup>. For instance, the results of one model compound study showed that the rate of acylation increases with solvent in the order tetrahydrofuran (THF) < acetonitrile < DMAc < *m*-cresol <sup>[1]</sup>. The large rate constant obtained in *m*-cresol suggests that the solvent also functions as an acid catalyst.

### Monomer reactivity

As mentioned above the mechanism of PAA formation is a nucleophilic substitution reaction at one of the carbonyl carbon atoms of the dianhydride with diamine. Therefore, it is expected that the reaction rate is primarily governed by the electrophilicity of the carbonyl groups of dianhydride and the nucleophilicity of the amino nitrogen of the diamine. The two carbonyl groups on a dianhydride are situated at the ortho position to each other and their strong electron-withdrawing effect activates each other towards nucleophilic reaction. The effect is particularly enhanced by the preferred carbonyl conformation locked in the coplanar aromatic ring.

Pyromellitic dianhydride (PMDA) displays the most reactive among the commercially available dianhydrides. It possesses four carbonyl groups attached to the same benzene ring in a coplanar conformation and, therefore, shows the strongest tendency to accept an electron. The electrophilicity of carbonyl carbons of each dianhydride can be measured in terms of the electron affinity ( $E_a$ ), a tendency to accept an electron, of the molecule (Table 1.1). For dianhydrides with the bridged bisphthalic anhydride structure, the bridge groups strongly influence  $E_a$  of dianhydrides. Compared with 3,3',4,4'-biphenyltetracarboxylic dianhydride (BPDA), which lacks a bridge group, the electron-withdrawing bridge group such as SO<sub>2</sub> and C=O increase the  $E_a$  values substantially, while electron-donating group such as ethers decrease it. The reactivity of ether-containing dianhydrides is significantly reduced so that they are practically not affected by the atmospheric moisture <sup>[6]</sup> while PMDA and 3,3',4,4'-benzophenonetetracarboxylic dianhydride (BTDA) must be handle under strictly moisture-free conditions at all times.

Unlike the  $E_a$  value of dianhydrides, the ability of diamines to give off an electron, the ionization potential, does not seem to correlate well in a simple manner, although the reaction rates of diamines towards a given dianhydride generally increase with increase in their ionization potential. The reactivity of diamines instead correlates well with its basicity ( $pK_a$ ) in Hammett's relation <sup>[7]</sup>. The reaction rates ( $k$ ) of various

diamines toward PMDA are shown in Table 1.2 in relation to their  $pK_a$ . The structure of diamines seems to influence the rate of acylation reaction more than the variation in dianhydrides structure. It should be noted that the rate constants differ by four orders of magnitude between amines with electron donating substituents and those with electron withdrawing ones. If reactive dianhydrides such as ether containing dianhydride are reacted with 4,4'-diaminodiphenylsulfone or 4,4'-diaminobenzophenone, it is expected that the molecular weight of the resulting PAAs would be lower.

Table 1.1 Electron affinity of aromatic dianhydrides<sup>[1]</sup>

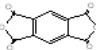
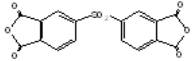
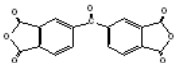
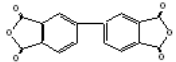
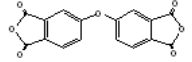
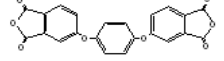
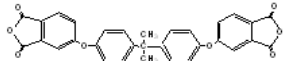
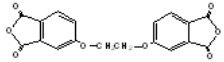
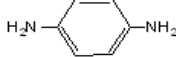
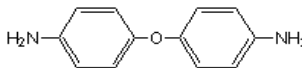
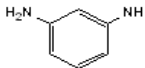
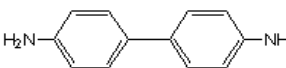
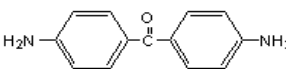
Dianhydrides	Abbreviation	$E_a$ (eV)
	PMDA	1.90
	DSDA	1.57
	BTDA	1.55
	BPDA	1.38
	ODPA	1.30
	HQDA	1.19
	BPADA	1.12
	EDA	1.10

Table 1.2 Basicity  $pK_a$  of diamines and their reactivities toward PMDA<sup>[1]</sup>

Diamine	$pK_a$	$\log k$
	6.08	2.12
	5.20	0.78
	4.80	0
	4.60	0.37
	3.10	-2.15

## Effect of reaction conditions

Early workers in the field of PI chemistry found that a higher molecular weight PAA could be produced by using higher concentrations of monomers<sup>[2]</sup>. It was also discovered that the molecular weight of the product was influenced by the order and mode of monomer addition, with the highest molecular weight being obtained when solid dianhydride was added to a solution of diamine. In fact, a slight stoichiometric excess of dianhydride was used to enhance the molecular weight. Temperature was also found to be critical, with the best result being obtained when polymerization was run between  $-20^{\circ}\text{C}$  and  $70^{\circ}\text{C}$ <sup>[9,10]</sup>.

The fact that the highest molecular weight PAA was obtained when solid dianhydride was added to a diamine solution was first thought to be due entirely to the avoidance of side reactions<sup>[11]</sup>. Aromatic dianhydrides were known to react with water and other impurities in amide solvents. However, since it was known that their reactions with diamines were considerably faster, it was correctly reasoned that competing reactions could be minimized by adding the dianhydride as a solid.

The solubility of dianhydrides is another important factor that influences the molecular weight of PAA. The solid dianhydride does not dissolve immediately upon its addition to a diamine solution<sup>[10]</sup>. In fact, its rate of dissolution is slow and dependent upon the concentration of monomers. Above, a certain critical concentration, which depends on the solubility of the dianhydride in the solvent and reactivity of the monomer, the rate of dissolution becomes slower than the rate of polymerization. The consequence of this is that some very high molecular weight product is formed almost immediately, long before all the dianhydride has dissolved and a stoichiometric balance of monomers has been achieved<sup>[12]</sup>. Some low molecular weight product is also formed in regions where the monomer stoichiometric is out of balance. Thus, the final polymer has a broad molecular weight distribution (MWD,  $>2$ ) that is often bimodal. Its weight-average molecular ( $M_w$ ) and intrinsic viscosity are also considerably higher than those that could be obtained in a reaction-controlled, step-growth process<sup>[13]</sup>.

Another early observation was that the viscosities of PAAs rapidly decreased when they were stored after preparation<sup>[9,11]</sup>. This was most often attributed to the sensitivity of amic acid to hydrolysis. Later work, however, showed that the phenomenon is associated with the reversibility of the propagation reaction and the fact that the polymers were produced by interfacial polymerizations<sup>[14]</sup>. The rate

constant for the reverse reaction is quite small, which means that only a few reactions take place during the first few hours and days of storage. These reactions, however, have a dramatic effect on the  $M_w$  of the polymer. The longest chains, which are a result of the interfacial nature of the polymerization and are the most significant in the determination of  $M_w$ , are the ones most affected by a single chain cleavage. PAAs will re-equilibrate in solution leading to the  $M_w$  decrease. The decrease in  $M_w$  can be slowed and often prevented by storing the solutions below 10°C. Of course, if the temperature is allowed to increase, the  $M_w$  will immediately begin to decrease. The most effective way to maintain the artificially high  $M_w$  values is to prevent the reverse reaction completely. This can be accomplished by neutralizing the carboxylic acid groups with bases, such as tertiary amines, so that there are no protons available to initiate the reverse reaction. Similar reasoning can be used to explain why esterified PAAs decrease in molecular weight upon storage<sup>[15]</sup>.

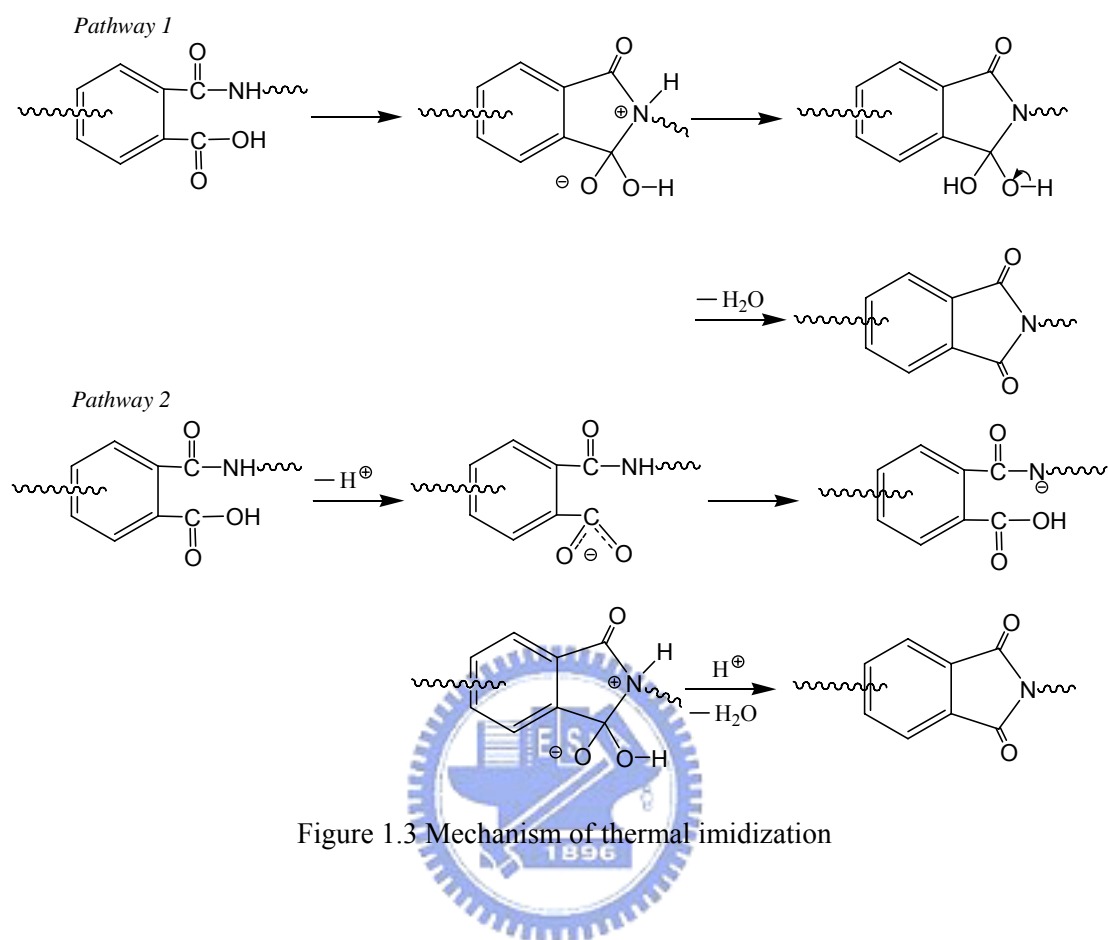
### Thermal imidization

The most widely used second step in the two-step method of PI synthesis involves heating the PAA in the solid state to 250–400°C. This is usually preceded by a processing operation, whereby a PAA solution is used to cast a film, form a coating, or spin a fiber. Molding powders are also prepared by the precipitation of PAAs from various solutions<sup>[11]</sup>. Too rapid a heating may cause the formation of bubbles in the sample. One of the most popular heating cycles consists of one hour at 100°C, followed by one hour at 200°C, and followed by one hour at 300°C<sup>[1,2]</sup>. However, in one study on thin films, the maximum degree of imidization that could be obtained with such a stepwise cycle was 85%. Much higher degree of imidization, i.e. >99% was obtained by constant heating at 230–250°C for 10 minutes<sup>[16]</sup>.

The imidization proceeds rapidly at the initial stage and tapers off at plateau, which is a typical diffusion-limited kinetic process. As the degree of imidization increases, the  $T_g$  or stiffness of the polymer chain increases. When the  $T_g$  approaches the reaction temperature, the imidization rate slows down markedly<sup>[1]</sup>.

Possible reaction pathways for the imidization process are shown in Figure 1.3<sup>[17]</sup>. The first point to note is that the time at which the proton attached to the nitrogen is lost is different in the two pathways. In the first, the proton is lost after cyclization; while in the second, it is removed prior or during the ring closure. Since the conjugate base of the amide is a considerably stronger nucleophile than the amide, ring

cyclization should occur considerably faster in the latter case.



The most commonly used method to determine the degree of chemical transformations in PIs is Fourier-transform infrared (FTIR) spectroscopy. Several characteristic absorption bands are used for the quantification of five-membered aromatic imides. The strongest absorption occurs at  $1720\text{ cm}^{-1}$  (C=O symmetrical stretching). However, the band partially overlaps with strong carboxylic acid band ( $1700\text{ cm}^{-1}$ , C=O) of PAA. The more useful bands of imide groups are  $1780\text{ cm}^{-1}$  (C=O asymmetrical stretching),  $1380\text{ cm}^{-1}$  (C–N stretching), and  $725\text{ cm}^{-1}$  (C=O bending). The absorption of anhydrides also occurs at  $1780$  and around  $720\text{ cm}^{-1}$ . When a mixture of imide and anhydride groups is analyzed, these bands may partially overlap with those of imide group, requiring proper correction. The carboxylic acid bands,  $1700\text{ cm}^{-1}$  (C=O) and  $2800\text{--}3200\text{ cm}^{-1}$  (OH), and amide bands,  $1600\text{ cm}^{-1}$  (C=O, amide I),  $1550\text{ cm}^{-1}$  (C–NH, amide II) and bands at  $3200\text{--}3300\text{ cm}^{-1}$  (NH) often appear as broad peaks, particularly when they are strongly associated with hydrogen bonds <sup>[1]</sup>.

## Chemical imidization

PAAs can be converted to the corresponding PIs at ambient temperature by treatment with mixture of aliphatic carboxylic acid dianhydrides and tertiary amines [18,19]. Acetic anhydride and pyridine or triethyl amine are normal used. Although this chemical method does not have the energy requirement of thermal imidization, it is generally not used commercially because of the problems associated with handling the reagents. The one exception is in the manufacture of molding powders, which are often prepared by this technique.

### 1.1.2 One-step method

Pis that are soluble in organic solvents are often prepared by the so called one-step or single stage method [1,2]. In this procedure, the dianhydride and diamine are stirred in a high-boiling organic solvent at 180–220 °C. Under these conditions, chain growth and imidization essentially occur spontaneously. The water generated by imidization is usually allowed to distill from the reaction mixture. Nitrobenzene,  $\alpha$ -chloronaphthalene and *m*-cresol containing isoquinoline are the most widely used solvents.

The one-step method is especially useful in the polymerization of unreactive dianhydrides and diamines. For example, phenylated dianhydrides cannot be used to prepare high molecular weight PAAs. These sterically hindered monomers, however, react rapidly with diamines at elevated temperature to give high molecular weight PIs [20,21]. Another interesting feature of the one-step method is that it can yield a material with a higher degree of crystallinity than can be obtained from the two-step method. The excellent solubility of the polymer at high temperature may allow it to obtain a more favorable conformation for packing.

### 1.1.3 Vapor deposition polymerization

Vapor deposition polymerization (VDP) is an alternative to the industrially important spin-coating method to prepare PI films [22, 23]. In the VDP process the diamine and the dianhydride are co-evaporated onto a substrate where they react to form a PI precursor, which converts to PI upon thermal curing. VDP is a dry process and does not require the use of solvents. This can be advantageous in some

applications, where the use of solvents can have deleterious effects or where contaminations have to be strictly avoided. VDP can be used to prepared thin PI films in nonplanar substrates, which is not possible using the spin-coating method. However, VDP is a slower and more expensive process compared to spin coating and this makes it less suitable for large-scale production.

The preparation of PI films by VDP was introduced independently by Iijima et al. in Japan<sup>[22]</sup> and by Salem et al.<sup>[23]</sup> in the United States in 1985 and 1986, respectively. In 1987 Grunze and Lamb demonstrated its feasibility for in situ PI/metal interface studies<sup>[24,25]</sup>. In most of subsequent investigations of PI films prepared by vapor depositing oxydiamine (ODA) and PMDA were used as diamine and dianhydride components, respectively. Only in a few cases other diamine and/or dianhydride precursors, such as decamethylene diamine (DMDA)<sup>[26,27]</sup>, *m*- and *p*-phenylene diamine (*m*- and *p*- PDA)<sup>[28,29]</sup>, 4,4'-diaminobiphenyl disulfide (DAPS)<sup>[30,31]</sup>, benzidine (BZD), 2,2'-bis(trifluoromethyl)-4,4'-diaminobiphenyl (TFDB), and 2,2-bis(3,4-dicarboxyphenyl)hexafluoropropane dianhydride (6FDA)<sup>[32]</sup> have been used.

### Deposition system

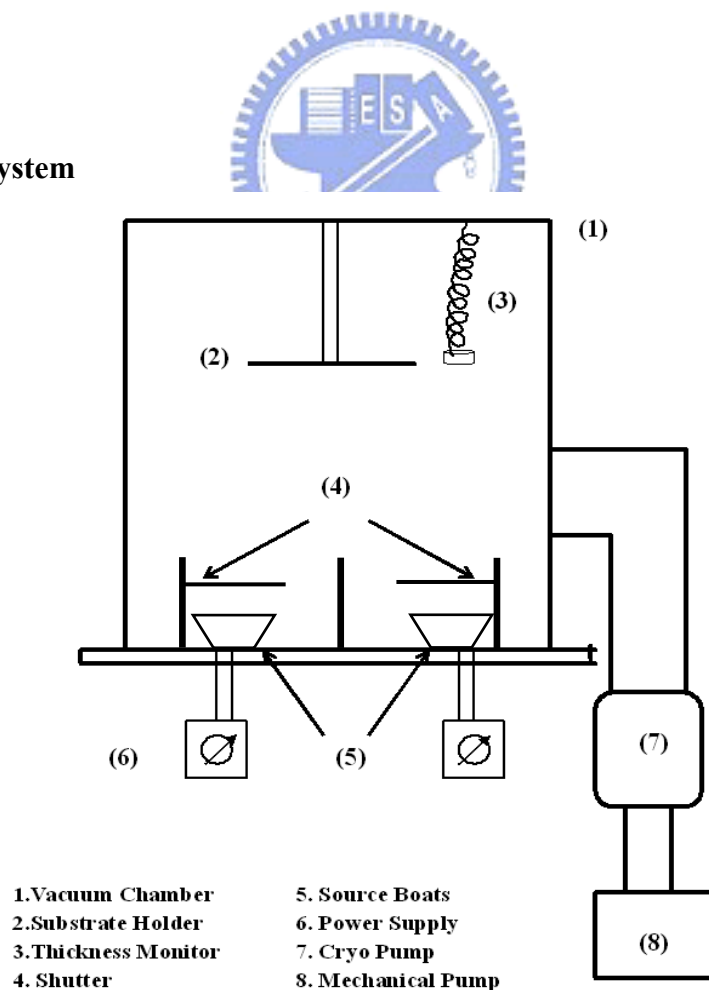


Figure 1.4 Schematic setup of vapor deposition system<sup>[33]</sup>.

A typical VDP system consists of a vacuum chamber equipped with two separately heatable sources for the diamine and the dianhydride components, a system to control the fluxes from the sources, a shutter system, and a sample holder (Figure 1.4)<sup>[33]</sup>. The source cells which are commonly made out of metals or metal alloys are heated resistively or radiatively to temperature up to 200°C in an ultra-high-vacuum. A fast and uniform heat transfer to the cells is necessary to obtain a good control over evaporation rate and ratio of the precursors. Quartz crystal oscillators are frequently used to monitor the evaporation rates from the source cells. Once calibrated, the source cells are heated to predetermined temperatures to obtain the desired deposition rate and ratio. A shutter is placed between evaporator and sample to avoid contamination of the sample prior to deposition. Any solid sample can be used as a substrate. The deposition is conformal rather than planar and the coverage of the substrate is determined by the distance and orientation of the substrate relative to the evaporator.

### **Mechanism of the VDP polyimides**

The reaction scheme for the formation of PMDA/ODA PI by VDP is shown in Figure 1.5. After co-deposition on to a substrate kept at room temperature, a mixture between reacted and unreacted material is obtained<sup>[22,23]</sup>. The FTIR spectrum shows bands at 1850 and 1780 cm<sup>-1</sup> due to anhydride carbonyl groups. They have been interpreted as unreacted trapped PMDA molecules. As an alternative, these bands could indicate anhydride end groups of short oligomer chains. The line-shape of the anhydride bands of a room temperature deposit does not agree well with line-shape observed for unreacted PMDA in PMDA/ODA mixture. It rather resembles the line-shape for terminal anhydride groups in short oligomer chains<sup>[34]</sup>.

XPS and FTIR measurements reveal that the room temperature deposit consists mostly of the intermediate C or an ammonium carboxylate salt of PAA (D) formed through the reaction of the carboxylic acid with free amino groups<sup>[35]</sup>. The carbonyl band for the carboxylic acid group of form E expected at 1720 cm<sup>-1</sup> is almost entirely absent. The intermediate C is formed through the attack of the amine at an anhydride carbonyl group and opening of anhydride ring. High-resolution electron energy loss spectroscopy measurements on PMDA/*p*-PDA and PMDA/aniline further confirmed that intermediate C can be formed and that it is stable at room temperature.

Raising the deposited temperature of the PMDA/ODA to 100°C leads to chain



growth. This step is accompanied by forming carboxylic acid groups of PAA. Complete imidization is achieved after heating at 250°C for 30 min. Subsequent heating at 400°C for 30 min does not result in significant additional changes in FTIR spectrum. Similar to spin-coated films the VDP films remains stable at this temperature.

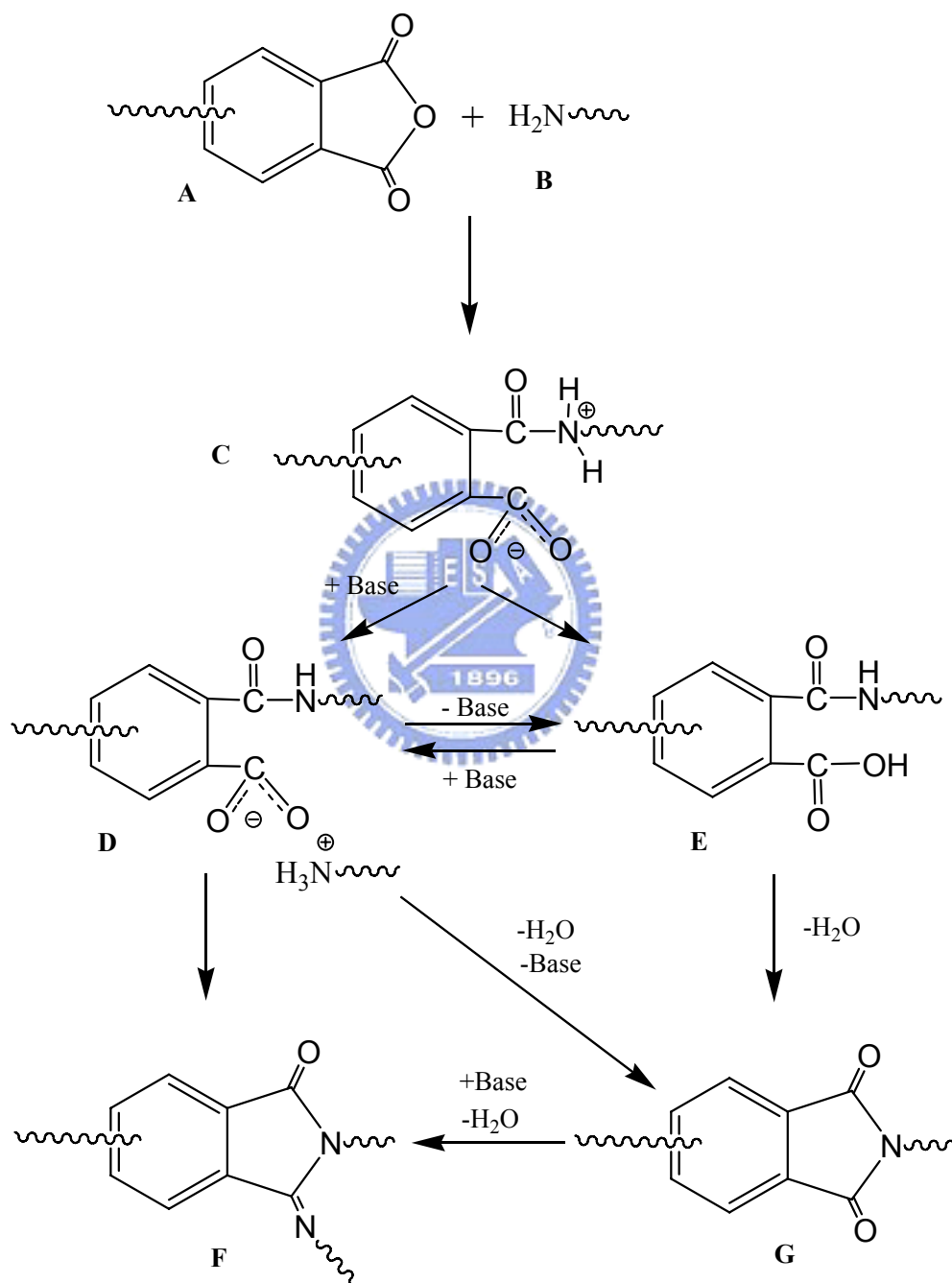


Figure 1.5 Reaction mechanism for the formation of VDP polyimides. A, anhydride endgroup; B, amino endgroup; C, intermediate carboxylate form; D, ammonium carboxylate salt of poly(amic acid); E, poly(amic acid); F, polyimide with imine branching; G, polyimide.

## 1.2 Characterization

Wholly aromatic PIs, like Kapton, have such incredible mechanical and thermal properties that they are used in replace of metals and glass in many high performance applications in the electronics, automotive, and even the aerospace industries. These properties come from strong intermolecular forces between the polymer chains <sup>[1]</sup>.

As mentioned above, the PAA polymerization rates are dominated by dianhydrides as an electron acceptor and diamines as an electron donor. This suggests that the PAA polymerization proceeds via a charge transfer (CT) complex intermediate <sup>[36]</sup>. Indeed, one often observes the formation of a yellow-green solution due to the CT complex at the initial polymerization stage, followed by yield of a viscous light-yellowish PAA solution.

Dine-art and Wright originally proposed that CT may occur in PIs and imides, based on color, melting point, and solubility data of model compounds <sup>[37]</sup>. Since that study, many workers have described aromatic PIs as chains of alternating segments of electron-donating and electron-accepting character in which either intramolecular or intermolecular CT occurs. Furthermore, they have used CT theory to explain a number of properties of imides and PIs, such as color, photodegradation, fluorescence, photoconductivity, electroconductivity, glass transition and melting temperatures <sup>[38]</sup>.

This sector reviews the accumulated fundamental research results for the CT theory, CT in PIs and the effect of CT in PI properties.

### 1.2.1 General charge transfer theory

#### Intermolecular CT in polyimides

Mulliken developed a general theory for charge transfer that many have found useful for describing intermolecular charge transfer complex <sup>[39]</sup>. The CT complex is comprised of two species, one acting as an electron donor, the other acting as an electron acceptor. For most complexes, the ground state CT interactions are small; upon excitation by UV/Vis light, an intermolecular CT transition occurs such that electron density transfers from the donor to the acceptor. The resulting excited state is mostly comprised of the CT state. The lowest energy transition is often a result of interactions between the highest occupied molecular orbital (HOMO) of the donor

and the lowest unoccupied molecular orbital (LUMO) of the acceptor, which correspond closely to the ionization potential of the donor and the electron affinity of the acceptor, respectively. The schematic orbital charge density for HOMO and LUMO in the PMDA-ODA is shown in Figure 1.6. It should be noted that the charge at HOMO and LUMO is localized on the ODA and PMDA residues, respectively. This means that CT can take place via the one-electron HOMO to LUMO transition.

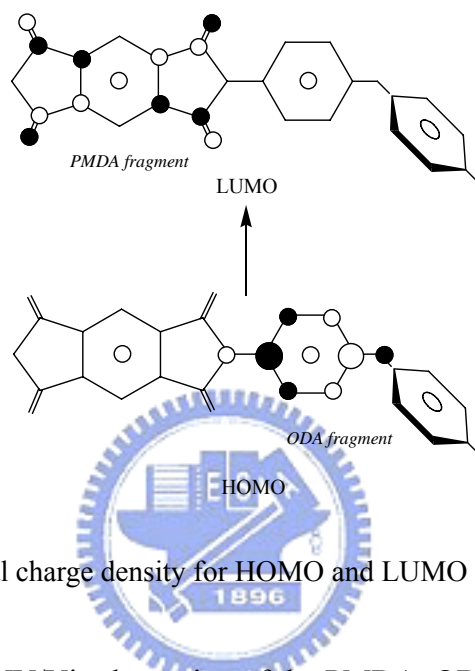


Figure 1.6 Orbital charge density for HOMO and LUMO in PMDA-ODA.

It is known that the UV/Vis absorption of the PMDA-ODA film consists of three peaks centered at 194 nm (6.4 eV), 210 nm (5.9 eV), 280 nm (4.4 eV), and a very weak absorption tail around 376 nm (3.3 eV)<sup>[40]</sup>. LaFemina et al.<sup>[40]</sup> on the basis of the experimentally measured adsorption spectrum, computed the electronic transition energies in PMDA-ODA using the spectroscopically parameterized CNDO/S3 model and compared with the experimental results.

The results of LaFemina et al. led to 413 nm (3.0 eV) as the HOMO-LUMO transition with a considerably low oscillator strength, corresponding the very weak lowest energy absorption tail in the PMDA-ODA film. The superjacent (second) LUMO also displays similar charge localization on the PMDA fragment, indicating that the HOMO-superjacent LUMO transition also causes CT. This transition at 280 nm (eV), which corresponds well to the actual absorption peak, occurs with a much higher transition probability (oscillator strength) than the HOMO-LUMO transition at 3.0 eV. In addition to these calculated transitions, the 320 nm band due to the pyromellitimide fragment, which is actually observed as a shoulder in the PMDA-ODA spectrum, should also be involved. Nonetheless, no 320 nm transition

was shown in the calculated transitions. Figure 1.7a shows an energy diagram drawn by the present authors according to the descriptions mentioned above. LaFemina et al. also observed the very weak CT fluorescence upon excitation at 290 nm and proposed a simple emission mechanism in PMDA-ODA as shown in Figure 1.7b.

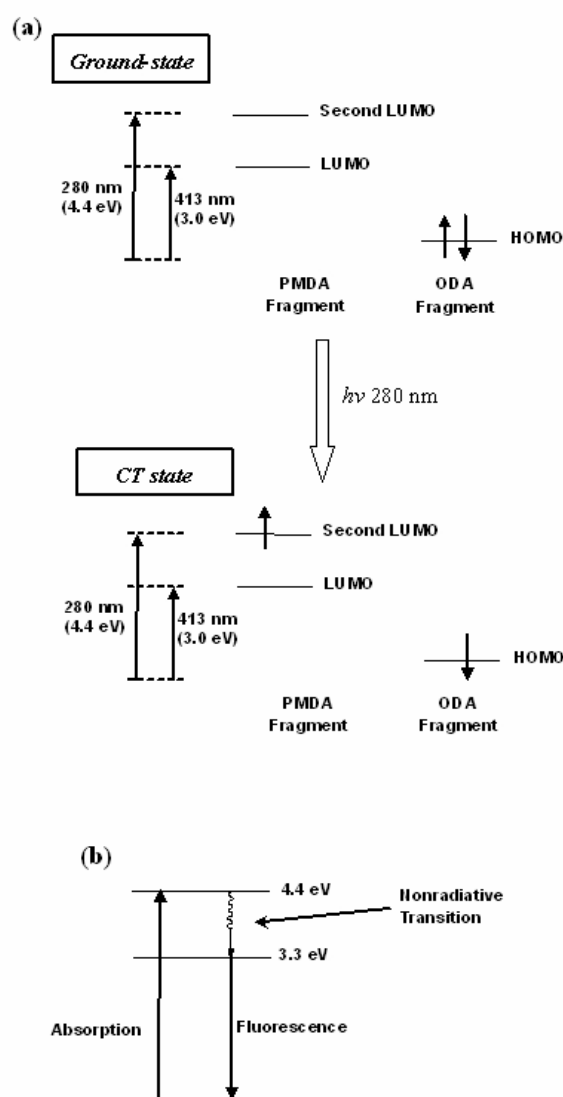


Figure 1.7 Schematic diagrams for: (a) HOMO-LUMO and HOMO-second LUMO transitions; and (b) CT emission in PMDA-ODA.

### Intramolecular CT in polyimides

Analogous to the intermolecular charge transfer, intramolecular charge transfer can occur between contiguous donor and acceptor fragments<sup>[1]</sup>. One can describe the

electronic transitions of such systems in terms of two types: local transitions that correspond to the transitions of the unperturbed fragments, and intramolecular CT transitions that correspond to the transfer of electron density from the bonding molecular orbital of one fragment to the antibonding molecular orbital of adjacent fragment. An essential feature of this charge transfer is its dependence on the torsional angle,  $\omega$ , defined as the angle between the planes of the donor and acceptor fragments (Figure 1.8). The probability for the intramolecular CT absorption transition should be highest in the limit of maximal  $\pi$  overlap, when the fragments are orthogonal. Furthermore, the intensity of the corresponding CT band has been shown experimentally to be proportional to  $\cos^2\omega$ . Although deviations may occur for various reasons, Suzuki has explained this relationship with approximations leading to the  $\cos^2\omega$  dependence of the dipole strength, oscillator strength, and molar extinction coefficient of the intramolecular CT complex.

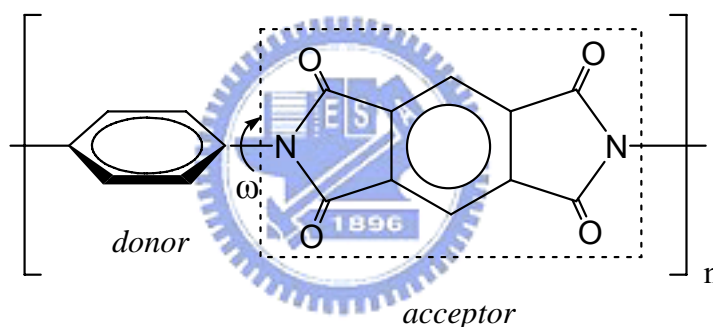


Figure 1.8 Torsional angle  $\omega$  and the intramolecular donor/acceptor nature of the polyimide.

### 1.2.2 Polyimide properties influenced by CT interactions

#### Fluorescence

Hasegawa et al. <sup>[41]</sup> first demonstrated experimentally that wholly aromatic PIs films show CT fluorescence. The first approach was to measure the fluorescence spectra of several commercial PI films (50  $\mu\text{m}$  thick). All the commercial samples used exhibited broad and structureless fluorescence in the long-wavelength range as shown in Figure 1.9. Another spectral feature is that the fluorescence intensity tends to reduce as the peak positions shift toward lower energy. This phenomenon is

characteristic of low molecular weight CT complex systems.

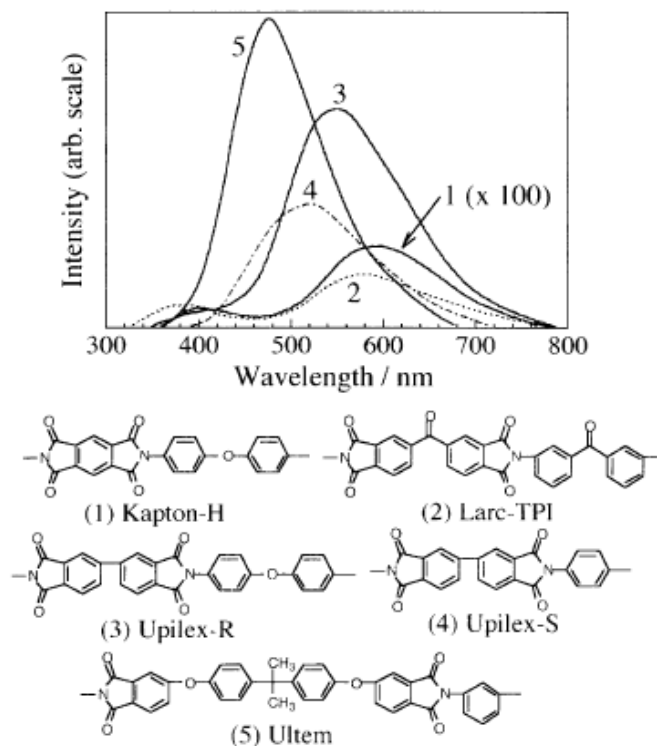


Figure 1.9 Fluorescence spectra of several commercial PI films (50  $\mu\text{m}$  thick) upon excitation at 300 nm<sup>[41]</sup>.

Wachsman and Frank<sup>[42]</sup> observed a fluorescence intensity enhancement with increasing final cure temperature for the PMDA-ODA system and proposed that this behavior is caused either by coplanarization between the benzimide and *N*-phenyl molecular conformational rearrangement, or by intermolecular CT complex formation promoted by dense molecular aggregation.

It seems not easy to separate the intermolecular and intramolecular CT fluorescence as for the CT absorption. However, it is most likely that the intermolecular CT mainly contributes to the fluorescence in the solid state of wholly aromatic PIs. This is according to the fact that the fluorescence intensity of the PI film prepared at 400  $^{\circ}\text{C}$  for 1h (rapid cure) was approximately 10 times higher than that cured upon the mildest condition (250  $^{\circ}\text{C}$ /5h)<sup>[43]</sup>. In other words, the intramolecular CT fluorescence is much weaker than the intermolecular one. This may be rationalized in terms of a model compound result in which the benzimide-phenyl coplanarization leads to an essentially non-fluorescent character.

## Photoconductivity

High-temperature PIs are used as an excellent electrical insulator in microelectronic devices. This is due to the fact that the CT complexes formed in PI films are classified into a category of weak CT complex, and therefore, have practically no contribution to the charge-separated structure at the ground state. Fainshtein et al.<sup>[44]</sup> showed that the increases in pressured and temperature cause a decrease in the electrical resistance in the dark for PIs derived from a fixed ODA with PMDA, BTDA, and 3,3',4,4'-diphenylsulphonetetracarboxylic dianhydride. These results were explained in terms of an electron conductance mechanism based on interchain CT complex formation.

Freilich<sup>[45]</sup> reported that electron donor-loaded Kapton film results in a striking photocurrent enhancement by five orders of magnitude as compared to the donor-free film. Figure 1.10 displays the photocurrent of the 7.6  $\mu\text{m}$  thick Kapton films containing 7.6 wt.-% DMA as a function of applied electric field ( $10^5$ – $10^6$   $\text{V cm}^{-1}$ ) upon illumination at 480 nm. The difference absorption spectrum between DMA-loaded and DMA-free Kapton films showed a new broad band peaking at 460 nm, which coincides with the photocurrent action spectrum in position. Also, a linear relationship was observed between the transition energy and the ionization potential of the dopants. From these, he concluded that this photocurrent enhancement results from CT complex formation between the pyromellitimide fragment in the PI backbone and DMA.

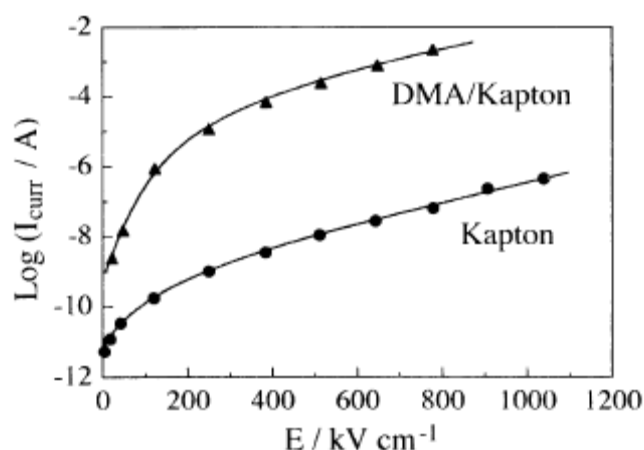


Figure 1.10 Photocurrent responses as a function of applied electric field for 7.5  $\mu\text{m}$  thick Kapton film and DMA-loaded Kapton film upon excitation at 480 nm<sup>[45]</sup>.

Lee et al.<sup>[46]</sup> measured the photoconductivity of a semi-aromatic PI derived from PMDA and an alicyclic diamine, 4,4'-methylene bis(cyclohexylamine) (MBCHA). Unexpectedly, this CT-inhibiting semi-aromatic PI showed somewhat higher photoconductivity than CT-allowing PMDA-ODA over the whole electric field examined. For PMDA-MBCHA film cured at 200°C/1h, prolonged annealing at 200 °C increased the photocurrent by one order of magnitude. In contrast, dimethyl-substituted PI remains loosely packed owing to the steric hindrance even if annealed. On the basis of these results, a mechanism of charge carrier photogeneration was proposed for the PMDA-MBCHA: the pyromellitimide fragments weakly interact with the alicyclic portions of different chains under an assumption that PI chains take the mixed layer packing arrangement. Then, upon photoirradiation, the electron transfer occurs from the ground-state alicyclic portions to the excited state pyromellitimide fragment, finally charge carriers are produced by field-assisted thermal dissociation of the photogenerated exciplex to form separated ion pairs.

### **Thermal, mechanical and melt viscosity properties**

Weak CT complexes look like exciplex in the viewpoint that both undergo charge separation only at the excited state. However, the latter has no attractive interaction between the donor-acceptor molecules at the ground state, whereas the former possesses a few kcal mol<sup>-1</sup> of bonding energies even in solution at the ground state, comparable or lower than the hydrogen bonding energies<sup>[47]</sup>. The CT complexes in PIs may also be the case. An electron donor-acceptor miscible blend between poly[(*N*-alkylcarbazol-3-yl)methyl methacrylate] and poly{2-[(3,5-dinitrobenzoyl)oxy]ethyl methacrylate} is a typical example. The interchain donor-acceptor attractive interactions results in a pronounced positive deviation from the additive property in the  $T_g$ -composition curve<sup>[48]</sup>. DSC thermograms confirmed that the blend includes the CT complexes formed exothermically.

Interchain CT interaction also may improve the mechanical properties of PI films. Sulzberg et al.<sup>[49]</sup> reported that 1:1 blending of anisylimino group-containing polycarbonate and nitro group-containing polycarbonate resulted in a higher tensile modulus (360,000 psi) than those of the component polymers (3335,000 psi for the donor polymer and 260,000 psi for the acceptor polymer). Similar mechanical property improvement was also observed in the 1:1 blend composed of *N,N*-dimethylamino-group and dinitro group pendant poly(propylene terephthalate)



polymers.

The interchain CT interactions in PIs tend to influence the softening behavior above  $T_g$  rather than the  $T_g$ 's themselves. St. Clair et al.<sup>[50]</sup> found that the addition of a small amount of a low molecular weight diimide compound into high molecular weight thermoplastic PIs has resulted in considerably decreased melt viscosities without significant  $T_g$  decrease. Two possible mechanisms were proposed for the pronounced results: the first is that the additives possessing a higher molecular mobility can have stronger interaction with the PI chains than the chains have with each other. Namely, the PI–additives CT interaction can break up the interchain CT interactions. In other words, this mechanism means that the CT interaction survive even in the molten state above the  $T_g$ . The second hypothesis is an  $M_w$  decrease of the PI caused by transimidation during melt mixing above the  $T_g$ , although measurements of the  $M_w$  were not conducted.

### **Voltage holding ratio in alignment layers for liquid crystal displays**

One of the most important necessary conditions in recent LCD such as thin film transistor and super twisted nematic modes is to have higher voltage holding ratio ( $R_v > 95\%$ ) even in a high-temperature range ( $60^\circ\text{C}$ ), which is required for the display stability of LCD. Kikuchi et al.<sup>[38]</sup> synthesized a large numbers of PIs and measured the  $R_v$  values to clarify a relation with the PI structures using a cyano-containing LC. Wholly aromatic PIs have a trend to show low values (40–70%). On other hand, in addition to wholly aliphatic PIs, semi-aromatic PIs exhibited very high values exceeding 90% except for the PIs using BAPP and BDAF as diamine components. These results lead to a speculation that the  $R_v$  is related to CT interactions in PIs, although the detailed mechanism is still poorly understood.  $R_v$  depends on not only the PI structure but also on the LC used. Much work has been carried out to improve this parameter through the chemical modification of LCs themselves, rather than through the survey of low  $R_v$  PIs.

## References

---

- [8] M. K. Ghosh and K. L. Mittal, *Polyimides: Fundamentals and Applications*, Marcel Dekker: New York, 1996.
- [9] D. Wilson and P. Hergenrothe (Ed:H. D. Stenzenberger), *Polyimides*, Chapman & Hall, London, 1990.
- [10] C. E. Sroog. *Prog. Polym. Sci.* 1991, **16**, 561.
- [11] M. Ree, K. J. R. Chen, G. Czornyj, *Polym. Eng. Sci.* 1992, **32**, 924.
- [12] S. W. Lee, S. I. kim, B. W. Choi, B. Chae, S. B. Kim, M. Ree, *Macromolecules* 2003, **36**, 6527.
- [13] T. Takekoshi, J. E. Kochanowski, J. S. Manello, M. J. Webber, *J. Polym. Sci.* 1985, **23**, 1759.
- [14] A. Y. Ardashnikov, I. Y. Kardash, A. N. Pravednikov, *Polym. Sci.* 1971, **13**, 2092.
- [15] Y. S. Vygodskii, T. N. Spirina, P. P. Nechayev, *Polym. Sci.* 1977, **19**, 1738.
- [16] G. M. Bower, L. Frost, *J. Polym. Sci.* 1963, **A1**, 3135.
- [17] C. E. Sroog, A. L. Endrey, S. V. Abramo, C. E. Berr, *J. Polym. Sci.* 1965, **A3**, 1373.
- [18] R. A. Dine-Hart, W. W. Wright, *J. Polym. Sci.* 1967, **11**, 609.
- [19] R. A. Orwoll, T. L. St. Clair, K. D. Dobbs, *J. Polym. Sci., Polym. Phys. Ed.*, 1981, **19**, 1385.
- [20] C. C. Walker, *J. Polym. Sci. Polym. Chem.* 1988, **26**, 1649.
- [21] W. Volksen, P. M. Cotts, in *Polyimides: Synthesis, Characterisation and Properties*, Plenum, New York, 1984, pp. 163-170.
- [22] J. B. Huang, B. M. Gong, *J. Vac. Sci. Technol.* 1985, **B3**, 253.
- [23] A. I. Baise, *J. Appl. Polym. Sci.* 1986, **32**, 4043.
- [24] J. A. Kreuz, A. L. Endrey, F. P. Gary, C. E. Sroog, *J. Polym. Sci.* 1966, **A1-4**, 2607.
- [25] M. M. koton, T. K. Meleshko, V. V. Kudryavtsev, *Polym. Sci. USSR*, 1982, **A24**, 791.
- [26] M. M. koton, T. K. Meleshko, V. V. Kudryavtsev, *Polym. Sci. USSR*, 1982, **26**, 2839.
- [27] F. W. Harris, S. L. C. Hsu, *High Perf. Polym.* 1989, **1**, 3.
- [28] F. W. Harris, S. O. Norris, L. H. Lanier, n *Polyimides: Synthesis, Characterisation and Properties*, Plenum, New York, 1984, pp. 3-14.
- [29] M. Iijima, Y. Takahashi, Ki Inagawa, A. Itoh, *J. Vac. Soc. Jpn.* 1985, **28**, 437.
- [30] J. R. Salem, F. O. Sequeda, J. Duran, W. Y. Lee, R. M. Yang, *J. Vac. Sci.*

- Technol.* 1986, **A4**, 369.
- [31] M. Grunze, R. N. Lamb, *Chem. Phys. Lett.* 1987, **133**, 283.
- [32] M. Grunze, R. N. Lamb, *J. Vac. Sci. Technol.* 1987, **A5**, 1685.
- [33] K. Iida, T. Nohara, K. Totani, S. Nakamura, G. Sawa, *Jpn. J. Appl. Phys.* 1989, **28**, 2552.
- [34] A. Kubono, H. Higuchi, S. Umemoto, N. Okui, *Thin Solid Films* 1993, **232**, 256.
- [35] B. G. Frederick, M. R. Ashton, N. V. Richardson, T. S. Jones, *Surface Sci.* 1993, **292**, 33.
- [36] N. V. Richardson, B. G. Frederick, W. N. Unertl, A. El Farrash, *Surface Sci.* 1994, **307**, 124.
- [37] A. Götzhäuser, S. Panov, Ch. Wöll, *Surface Sci.* 1994, **314**, 849.
- [38] A. Götzhäuser, S. Panov, Ch. Wöll, *Surface Sci.* 1995, **334**, 235.
- [39] Y. Y. Maruo, Y. Andoh, S. Sasaki, *J. Vac. Sci. Technol.* 1993, **A11**, 2590.
- [40] S. C. Chen, W. T. Whang, *Thesis, A study on vapor deposition polymerization of polyimides and their electroluminescent characteristics in light emitting diodes* (in Chinese), 2001, National Chiao Tung university, Taiwan.
- [41] A. K. Saini, C. M. Carlin, H. H. Patterson, *J. Polym. Sci. Polym. Chem. Ed.* 1992, **30**, 419.
- [42] C. Hahn, T. Strunskus, D. Frankel, M. Grunze, *J. Electron spectrosc. Relat. Phenom.* 1990, **54/55**, 1123.
- [43] M. I. Bessonov, M. M. Koton, V. V. Kudryavtsev, L. A. Laius, *Polyimides: thermally stable polymers*, Plenum, New York, 1987.
- [44] R. S. Dine-Hart, W. W. Wright, *Makromol. Chem.* 1971, **143**, 189.
- [45] M. Hasegawa, K. Horie, *Prog. Polym. Sci.* 2001, **26**, 259.
- [46] R. S. Mulliken, *Molecular Complexes*, John Wiley & Sons, New York, 1969.
- [47] J. P. LaFemina, G. Arjavalingham, G. Hougham, *J. Chem. Phys.* 1989, **90**, 5154.
- [48] M. Hasegawa, M. Kochi, I. Mita, R. Yokota, *Polym. Prepr. Jpn.* 1987, **36**, 1158.
- [49] E. D. Wachsman, C. W. Frank, *Polymer* 1988, **29**, 1191.
- [50] M. Hasegawa, M. Kochi, I. Mita, R. Yokota, *Eur. Polym. J.* 1989, **25**, 349.
- [51] Y. Fainshtein, L. A. Igonin, G. A. Lushcheikin, *Polym. Sci. USSR*, 1976, **18**, 661.
- [52] S. C. Freilich, *Macromolecules* 1987, **20**, 973.
- [53] S. A. Lee, T. Yamashita, K. Horie, *J. Polym. Sci. B* 1998, **36**, 1433.
- [54] N. Mataga, T. Kubota, *Molecular interactions and electronic spectra*, Marcel Dekker, New York, 1970.
- [55] J. M. R. Parada, V. Percec, *Macromolecules* 1986, **19**, 55.

- [56] T. Sulzberg, R. J. Gotter, *J. Polym. Sci. A1* 1970, **8**, 2747.
- [57] T. L. S. Clair, J. R. Pratt, D. M. Stoakley, H. D. Burks, *Polyimides: materials, chemistry, and characterization*, Elsevier, Amsterdam, 1989.



# *Chapter 2*

## **Electroluminescence and Electron Transport Characteristics of Aromatic Polyimides**



## 2.1 Introduction

Aromatic polyimides (APIs) are usually synthesized through a two-step method: preparation of the poly (amic acid) (PAA) and then thermal or chemical imidization. The PAA polymerization rates relate to the electron affinity ( $E_a$ ) of dianhydrides as an electron acceptor and the ionization potential ( $I_p$ ) of diamines as an electron donor. This suggests that the charge transfer (CT) interaction may occur between the electron-donor and electron-acceptor fragments of APIs<sup>[1]</sup>. Many previous works had reported the relationship of CT and fluorescence in APIs<sup>[2-13]</sup>. Wachsmann and Frank<sup>[2]</sup> observed a significant increase in the CT fluorescence intensity with increased molecular aggregation by increased imidization temperature. Haobin et al.<sup>[3]</sup> reported increased concentration of polyimide solution led to more dense packing in the polymer chains then increasing the CT fluorescence. However, aggregation would be one of the main barriers to high luminescence quantum yield in the conjugated polymer<sup>[14,15]</sup>. This hints that APIs could develop a different fluorescence mechanism in comparison with conjugated polymers.

Polymer light-emitting diodes (PLEDs) have attracted much interest in display application due to their excellent mechanical properties, tunable emission and low fabrication cost. However, one of the serious problems of PLED is the poor durability under operation owing to the intrinsically flexible and soft characteristics, crystallization, oxidation and photodegradation of the organic materials<sup>[16,17]</sup>. The glass transition temperature ( $T_g$ ) of polymer is an important property for the application of PLED, because an emission layer would be easily relaxed by the Joule heating during operation and results in a device destruction<sup>[18]</sup>. Application of thermostable polymers in PLED can improve the lifetime of polymer-based devices. Some research groups have demonstrated significant improvements in photoluminescence (PL) or electroluminescence (EL) by using polyimides as a hole transport material<sup>[19-24]</sup>. Polyimides which contain the moieties of anthracene, perylene, metal complex, tetraphenyl terabiphenyl-*p*-quinquephenyl, 2,5-distyrylpyrazine, dibenzofurane, and furyl-substituted biphenylene were used as light emitting materials<sup>[25-36]</sup>.

In this chapter presents the study of the newly synthesized BAO-based APIs in application of PLED. The relationship between the different dianhydride structures and aggregation were investigated, and was used to examine the CT interaction in polyimides and the fluorescence behavior. The single layer and double layer API-LED devices were further fabricated to understand the electron transport characteristics of

the APIs and the influence on light emitting characteristics.

## 2.2 Experimental section

### 2.2.1 Materials

2,5-Bis(4-aminophenyl)-1,3,4-oxadiazole (BAO, 98%) from Lancaster was prior dried in a vacuum oven at 120°C for 3 hours. 3,3'-Oxydiphthalic anhydride (ODPA, 98%), pyromellitic dianhydride (PMDA, 98%) from Tokyo Chemical Industry and 4,4'-(hexafluoro-iso-propylidene) diphthalic anhydride (6FDA), 4,4'-(4,4'-isopropylidenediphenoxy)bis(phthalic anhydride) (BPADA) from Aldrich Chemical Co. Inc. were purified by recrystallization from acetic anhydride and then dried in a vacuum oven at 125°C over night. *N,N*-dimethylacetamide (DMAc) from Tedia Company was dehydrated with molecular sieves.

### 2.2.2 Preparation of PI films

A typical procedure of the APIs preparation was shown in Figure 2.1. The reaction was carried out in a flask by the polycondensation of diamine BAO (1.00 mmol) and the dianhydride (1.01 mmol) in DMAc (4 ml) under a nitrogen stream at room temperature. The solid dianhydride was added into the diamine solution by five portions. After the dissolution of all dianhydride, the reaction mixture was further stirred at room temperature for 3 hours. The PAA solutions (15 wt.-%) were cast on glass plates, and then step-heated at 100°C, 150°C, 200°C, 250°C, each one for an hour to get API films with 20µm thickness.

### 2.2.3 Devices fabrication

The PAA solutions were diluted with DMAc to solid content (w/w) of 6%. Then spin-coated the PAA solutions on a 2×2 cm ITO glass at 2000 rpm and step-heated to 100°C, 150°C, 200°C, 250°C, each one for an hour in vacuum to obtain API thin films with 800 Å thickness. The metal Al was deposited on the surface of the API thin films by thermal evaporation under  $5 \times 10^{-6}$  torr to form ITO/API/Al LEDs. For ITO/PPV-PVA/API/Al LED, The detailed procedure for synthesis of PPV precursor has been shown in our previous research<sup>[37]</sup>. The PPV precursor aqueous solution (0.5

wt.-%) was the homogeneously mixed with predissolved PVA (Mw=72000) (aqueous solution, 4.0%) at the weight ratio of 100/7. The PPV-PVA precursor was spin-coated on a 2×2 cm ITO glass and then step-heated to 50°C, 150°C, 200°C, 300°C each one for an hour to form PPV-PVA thin film with 200Å thickness. PAA was then spin-coated on the PPV thin film and followed the same imidization process and evaporated Al layer as aforementioned.

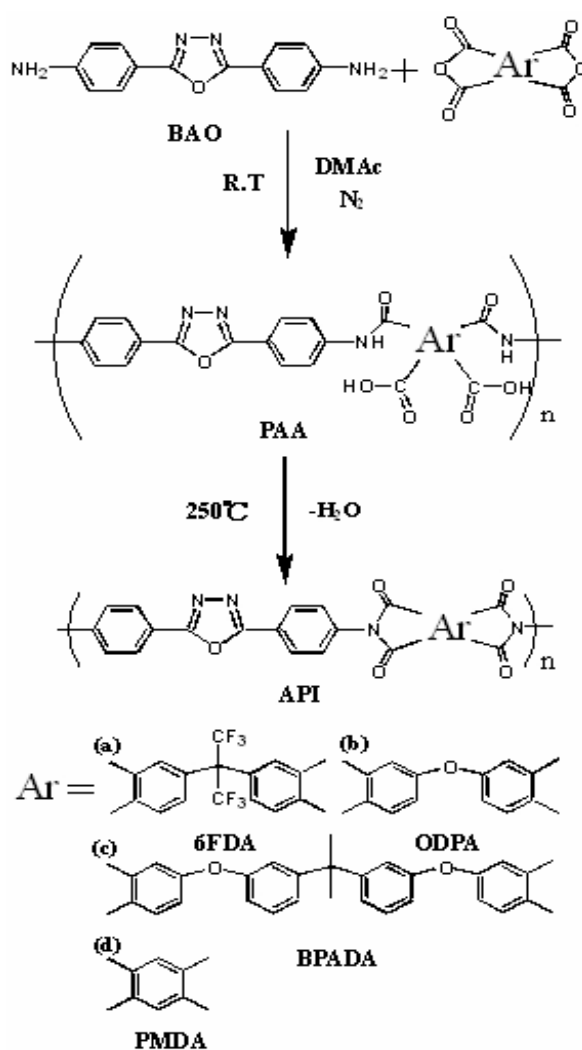


Figure 2.1 Monomer structures and the synthesis route of poly (amic acid)s and polyimides.



## 2.2.4 Characterization

TA Instruments TGA 2950 was used to measure decomposition temperature ( $T_d$ ) by a heating rate of 20°C/min from 30–900°C under Nitrogen. The coefficient of linear thermal expansion (CTE) were measured by thermomechanical analysis (TMA) with a TA Instruments TMA 2940 at heating rate of 10°C/min, and the specimens were 12 mm long, 4 mm wide, and 20µm thick. The glass transition temperature ( $T_g$ ) measurement with dynamic mechanical experiments was performed using a TA Instruments DMA 2980 Dynamic Mechanical Analyzer at 5°C/min and a frequency 1 Hz. The modulus was measured as a function of temperature with a tension clamp to hold the sample (15×5 mm).

Infrared (IR) spectra were measured with Nicolet Protégé 460. Fluorescence spectra of all films were measured using Shimadzu RF-5301 PC Spectrofluorophotometer with the excitation source at 330 nm. The absorption spectra were taken with HP8453 UV-VIS spectrometer. The energy level of electronic structure of the polymers is determined using UV-Vis absorption spectra and the data of cyclic voltammetry using CHI600A Electrochemical Analyzer. The cyclic voltammetry was carried out using Pt counter electrode and a Ag/Ag<sup>+</sup> reference at the scan rate of 10 mv/s. The electrolyte was 0.1 M tert-BuNClO<sub>4</sub> in acetonitrile.

Film thickness was measured using Alpha Step Dektak ST surface profiler. The electroluminescence (EL) spectra were measured by Jasco FR-770 spectrometer. The current-voltage characteristics of the LEDs were measured by Keithley 237 electrometer. The intensity-voltage characteristics were measured using Keithley 237 electrometer with a photodiode detector of New Port power meter (Model 1815-C). The wide-angle X-ray diffraction (WAXD) patterns were obtained by MacScience MXP using Cu K $\alpha$  radiation (50 KV, 200 mA,  $\lambda$ = 1.54 Å) with Monochromator.

## 2.3 Results and discussion

The structures of the APIs are determined by IR spectra. The complete imidization of the APIs are confirmed by the absence of C=O vibration band at 1670 cm<sup>-1</sup> and O–H vibration band at about 3000 cm<sup>-1</sup> of PAA, and the C=O vibration band of anhydride at 1850 cm<sup>-1</sup>. Furthermore, the characteristic absorption peaks of the imide group at 1780 cm<sup>-1</sup>, 1720 cm<sup>-1</sup>, and 1380 cm<sup>-1</sup> are observed. The former two peaks are due to the asymmetric and symmetric C=O stretching, and the last peak is

associated with the C–N stretching <sup>[1]</sup>.

The inherent viscosity of the PAAs in DMAc (0.5g/dL) were measured at 30°C with a Ubbelohde viscometer and listed in Table 2.1. The inherent viscosities of the PAAs relate to the  $E_a$  of the dianhydrides. The order of  $E_a$  for the dianhydrides is: PMDA>6FDA>ODPA>BPADA <sup>[1,12]</sup>. The higher  $E_a$  of dianhydrides show stronger electron-withdrawing ability in the nucleophilic substitution reaction of PAAs formation, and that would form higher molecular weight and viscosities of the resultant PAAs.

Table 2.1. Inherent viscosity of the PAAs and thermal properties of the APIs

APIs	$\eta_{inh}$ (dL/g) <sup>a</sup>	$T_d$ <sup>b</sup> (°C)	$T_g$ (°C)	CTE <sup>c</sup> (ppm/K)
<b>BAO-PMDA</b>	1.048	562	425	16.6
<b>BAO-6FDA</b>	0.993	540	350	49.9
<b>BAO-ODPA</b>	0.973	531	297	31.2
<b>BAO-BPADA</b>	0.401	514	257	86.1

a: Measured in DMAc (C = 0.5g/dL) at 30°C

b: 5 wt.-% decomposition temperature measured under N<sub>2</sub>

c: The CTE values are determined from 50 to 250°C

The thermal properties of the APIs were determined by TGA, DMA and TMA, and the results were listed in Table 2.1. The synthesized APIs exhibit excellent thermal stability with the  $T_d$  of 5 wt.-% weight loss higher than 500°C. The APIs also showed high  $T_g$  ranging from 257 to 425°C. Especially in BAO-6FDA, the  $T_g$  value is 350°C, which is higher than that of typical 6FDA-derived polyimides <sup>[38]</sup>. This may result from the oxadiazole-containing diamine, BAO, stiffening the main chain of the APIs <sup>[39,40]</sup>. The presented CTEs of the APIs are from 50 to 250°C. BAO-PMDA has the lowest CTE, BAO-ODPA and BAO-6FDA next, and BAO-BPADA is the highest. Shunichi et al. <sup>[41]</sup> pointed out that thermal expansion is an expansion of free volumes, and a low CTE results from small free volumes. BAO-PMDA with rod-like structure has dense molecular aggregation and exhibits small free volume as well as low CTE. While BAO-BPADA contains bulky –CH<sub>3</sub> groups and two kink points of O groups in the dianhydride fragment. These disturb chain packing and increased the free volume.

Figure 2.2 shows the UV/Vis absorption spectra of the APIs. There is a little difference between the absorption spectra of these APIs. BAO-PMDA and BAO-6FDA have closely maxima absorption peaks at about 300 nm, and the shoulders are observed at 400 nm and 375 nm, respectively. However, both BAO-ODPA and BAO-BPADA show significant red-shift at about 350nm and no shoulders are observed. The long-wavelength absorption in polyimides results from intermolecular CT interactions and the red-shift enhances with increasing the intermolecular CT interactions <sup>[39]</sup>. BAO-ODPA and BAO-BPADA may exhibit stronger intermolecular CT interactions than BAO-PMDA and BAO-6FDA.

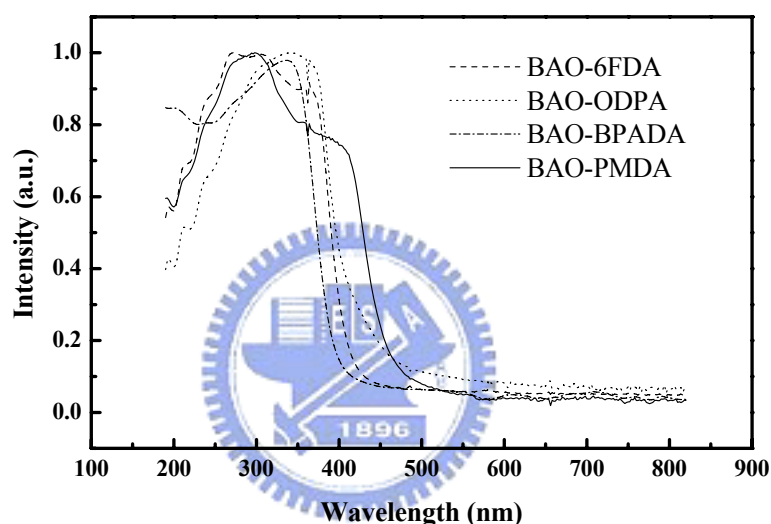


Figure 2.2 Absorption spectra of the API films with 20  $\mu\text{m}$  thickness.

Figure 2.3 shows the fluorescence spectra of the APIs. The APIs exhibit broad and structureless fluorescence in the long-wavelength range <sup>[2-13]</sup>. The BAO-ODPA has the strongest fluorescence intensity than the others. The tendency of fluorescence intensity does not agree with the degree of the molecular packing. This suggests that CT fluorescence not only relates to the molecular aggregation, but also sensitive to the orientation of local structures in polyimides. The WAXD was used to characterize the local ordering of these APIs and shown in Figure 2.4. All the APIs have similar diffraction patterns and contain crystalline structures. The degree of crystal is: BAO-PMDA > BAO-6FDA > BAO-BPADA > BAO-ODPA, and this tendency is opposite to the order of fluorescence intensity (Figure 2.3).

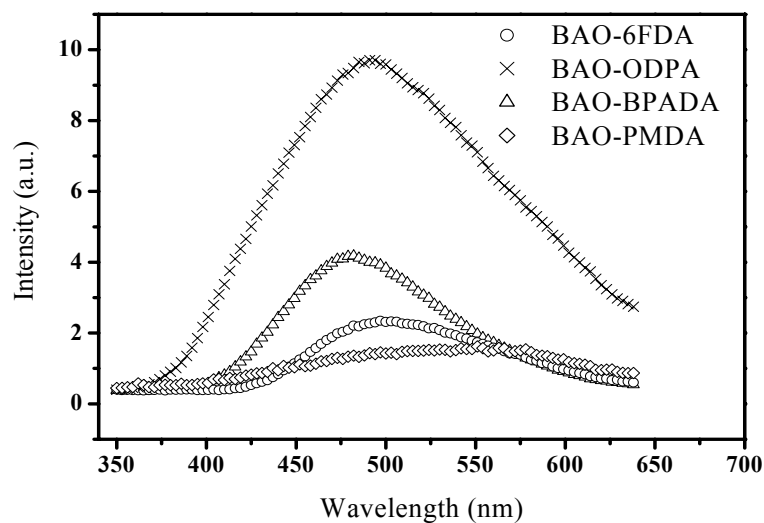


Figure 2.3 Fluorescence spectra of the APIs films with 20  $\mu\text{m}$  thickness

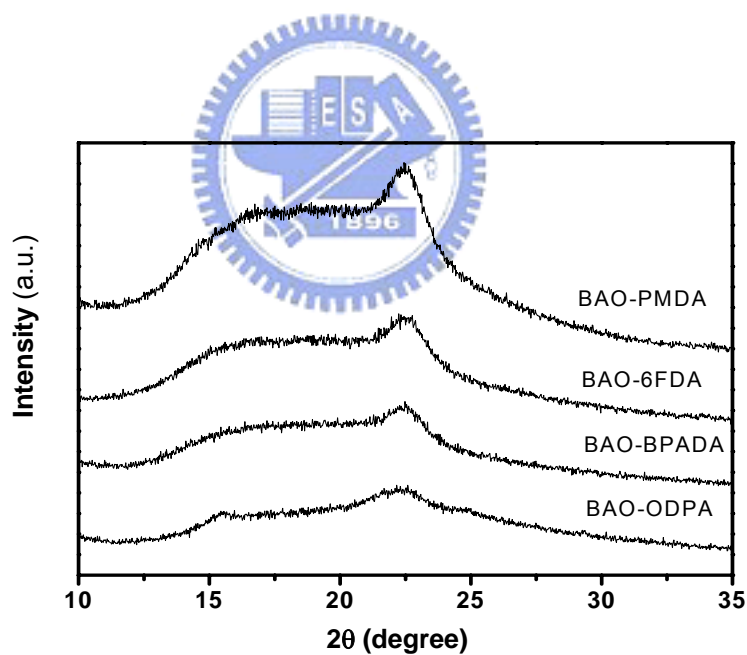


Figure 2.4 WAXD patterns of the APIs films with 20  $\mu\text{m}$  thickness.

Figure 2.5 shows the chain-chain interaction of the intermolecular CT and the crystal along two neighboring chains<sup>[38]</sup>. In polyimides, the charge at HOMO and LUMO is localized at the electron-donating aminophenyl fragment and the electron-accepting imide fragment. This means charge transfer can occur via the

electron HOMO to LUMO transition, and the intermolecular CT are formed by the electron-donor (aminophenyl rings) and electron-acceptor (imide rings) belonging to adjacent molecular chains (Figure 2.5a). However, when the molecular chains align in the form that the imide rings and the amine phenyl rings constitute separate layer (Figure 2.5b), the intermolecular CT interaction would be reduced. Because exhibiting lower extent of the crystal, on the other hand, BAO-ODPA API has more imide rings-aminophenyl rings face-to-face stacking, and shows the strongest fluorescence intensity than the others.

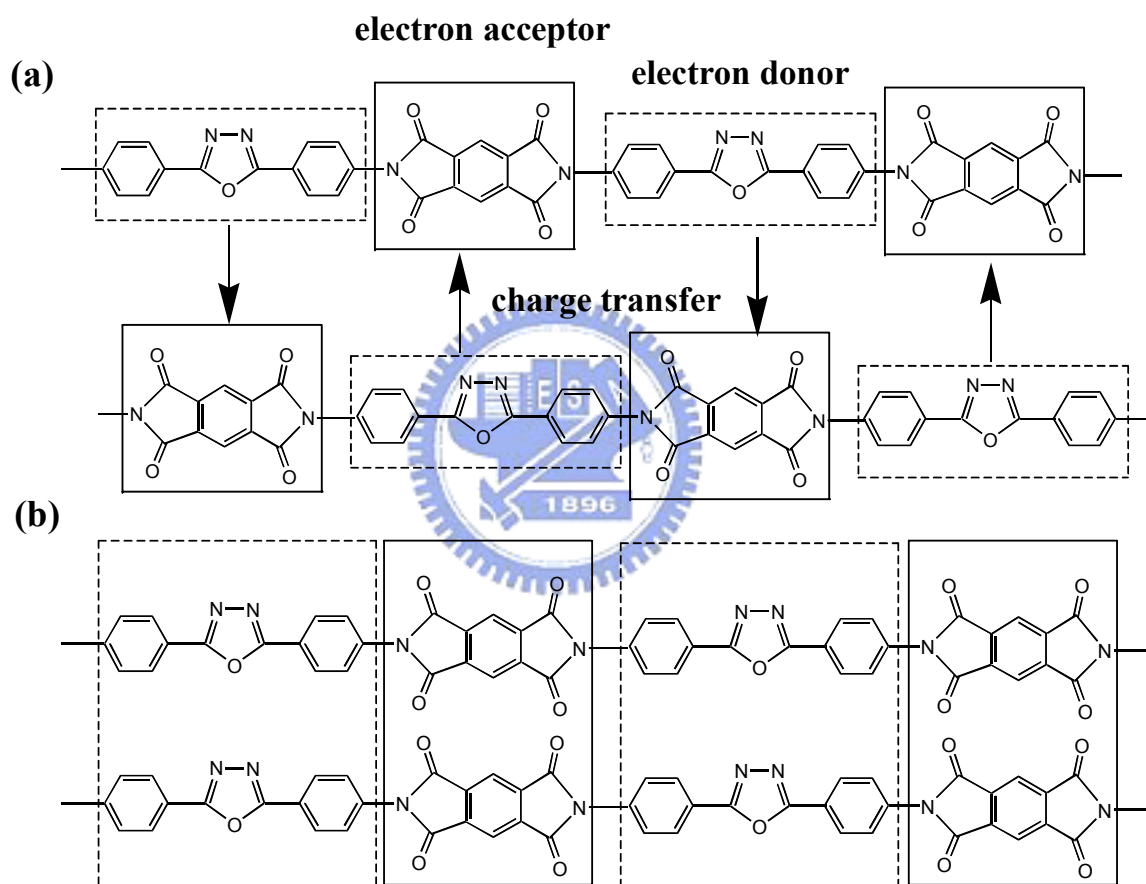


Figure 2.5 Polyimide chain-chain interaction (a) CT interaction and (b) crystal.

EL spectra were detected in BAO-ODPA and BAO-6FDA. The weaker EL intensity of BAO-BPADA than BAO-6FDA in this study may result from higher CTE (Table 1). Large CTE would lead to cracking and delaminating between polyimide films and substrates to affect adversely the devices reliability<sup>[1]</sup>. As shown in Figure 2.6, the EL spectra of the APIs are similar to their fluorescence spectra (Figure 2.3) indicating that both EL and fluorescence may proceed the same radiative excited

states in these APIs [42].

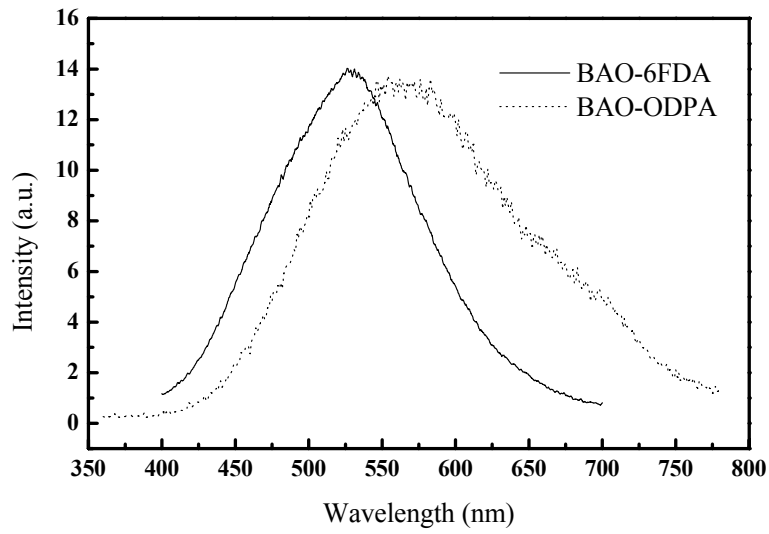


Figure 2.6 Normalized electroluminescence spectra of the single layer API-LED devices

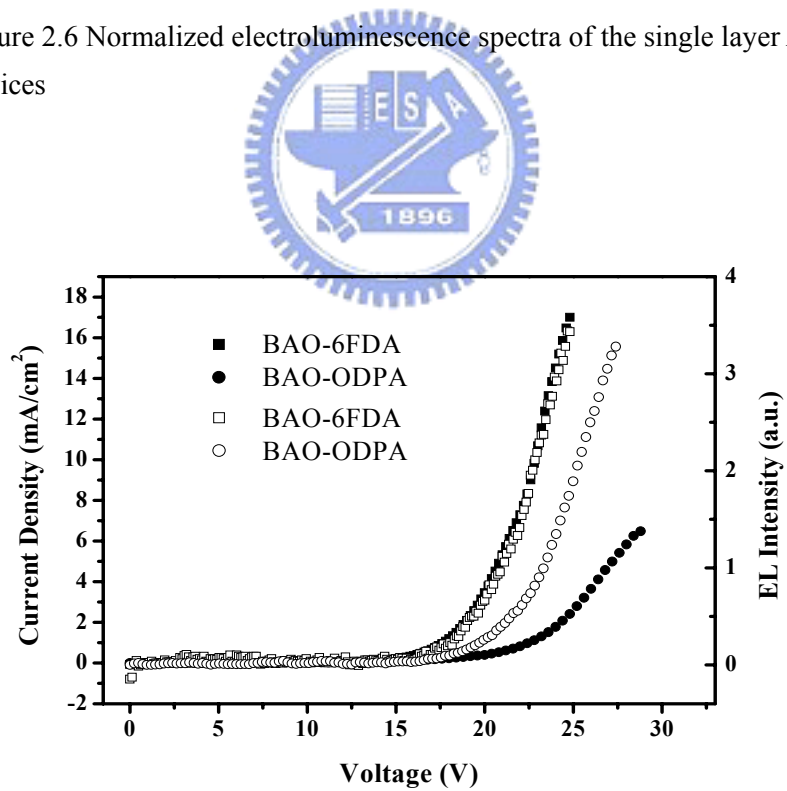


Figure 2.7 Current density-voltage characteristics (closed mark) and EL intensity-voltage (open mark) for the single layer API-LED devices.

Figure 2.7 shows the curves of current-voltage (I-V) and EL intensity-voltage (EI-V) of the single-layer API LED devices for BAO-6FDA and BAO-ODPA. The current and emission intensity increases with the applied voltage, and both LED devices show distinct diode characteristics. In the EI-V curves, the threshold voltages ( $V_{th}$ ) are 18V and 22V for BAO-6FDA and BAO-ODPA, respectively. The EL efficiency can be evaluated from the slope of the EL intensity versus current density and shown in Figure 2.8. The BAO-ODPA LED has a higher EL efficiency than the BAO-6FDA LED although the former has a higher  $V_{th}$ . It may suggest that the dianhydride structure has certain effects on the EL characteristics.

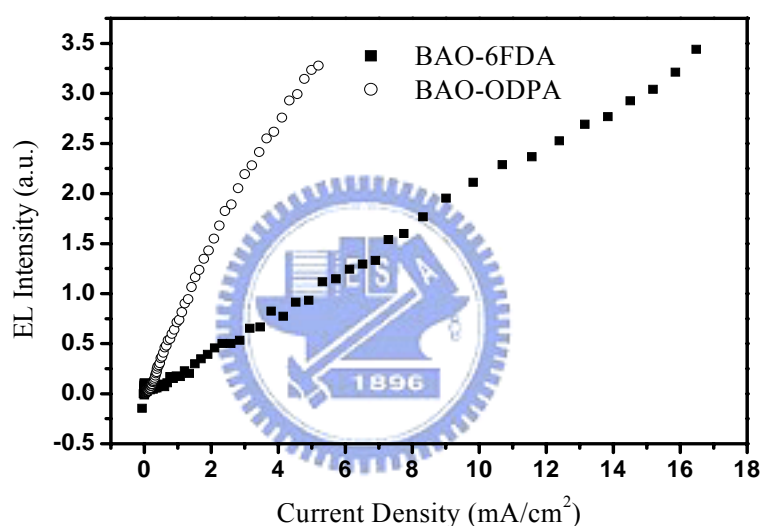


Figure 2.8 EL efficiency of single layer API-LED devices.

As shown in Figure 2.9, the EL spectrum of the double layer LED, ITO/PPV-PVA/BAO-ODPA/Al, is very close to that of the single-layer PPV-PVA device, indicating PPV acts as the emitting layer in the double layer device. For the double layer device, the turn-on electric field is about  $2.5 \times 10^6$  V/cm, and the operating voltage is higher than that of the single-layer device ( $1.6 \times 10^6$  V/cm) due to significant resistive voltage drop across the BAO-ODPA layer. The similar phenomenon has also been reported in other system<sup>[43]</sup>. The EL efficiency of these devices is shown in Figure 2.10 (both axes are plotted in logarithmic scale). It shows that the double layer device with BAO-ODPA layer has a high EL efficiency than single-layer PPV-PVA device, indicating that BAO-ODPA PI film indeed significantly

improve the EL efficiency of PPV-PVA light emitting layer by two order of magnitude.

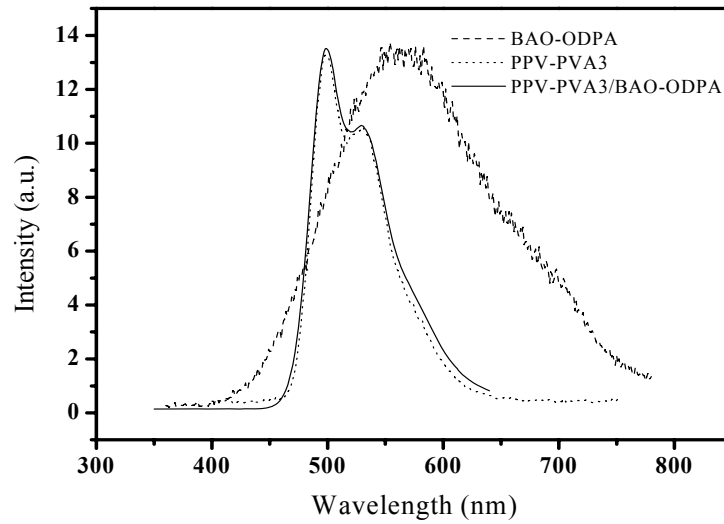


Figure 2.9 Normalized electroluminescence spectra of the LED devices.

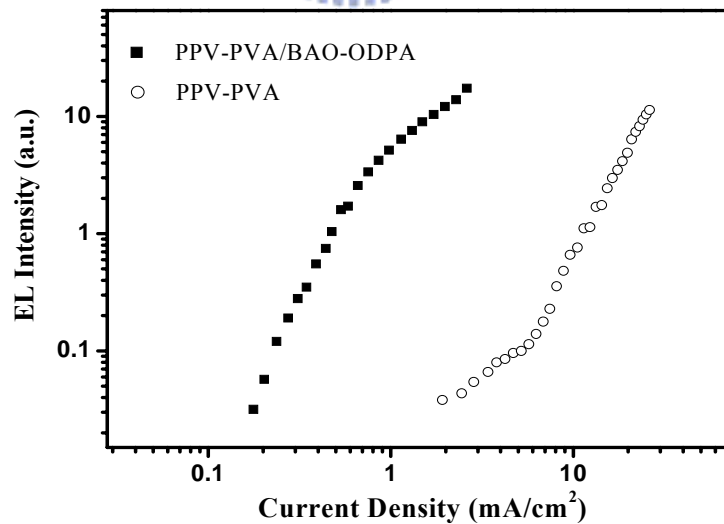


Figure 2.10 EL efficiency of the LED devices: ITO/PPV-PVA/Al and ITO/PPV-PVA/BAO-ODPA/Al.



The energy band diagram of the double layer ITO/PPV-PVA/BAO-ODPA/Al device is shown in Figure 2.11. The energy barrier for electron injection decreases from 1.6 eV (in the single-layer PPV-PVA device) to 1.0 eV (in the double layer device). Moreover, the HOMO of BAO-ODPA (5.9 eV) is larger than that of PPV-PVA (5.1 eV); thus the BAO-ODPA layer provides both electron transport and hole blocking effect. Since BAO-ODPA has high HOMO and LUMO, electron injection from the cathode is enhanced. The probability of radiative recombination in the light-emitting layer PPV-PVA is increased and enhancement of the EL efficiency. In addition, the BAO-ODPA layer separates the recombination zone from the metal electrode so that the recombination at the metal/polymer interface is avoided.

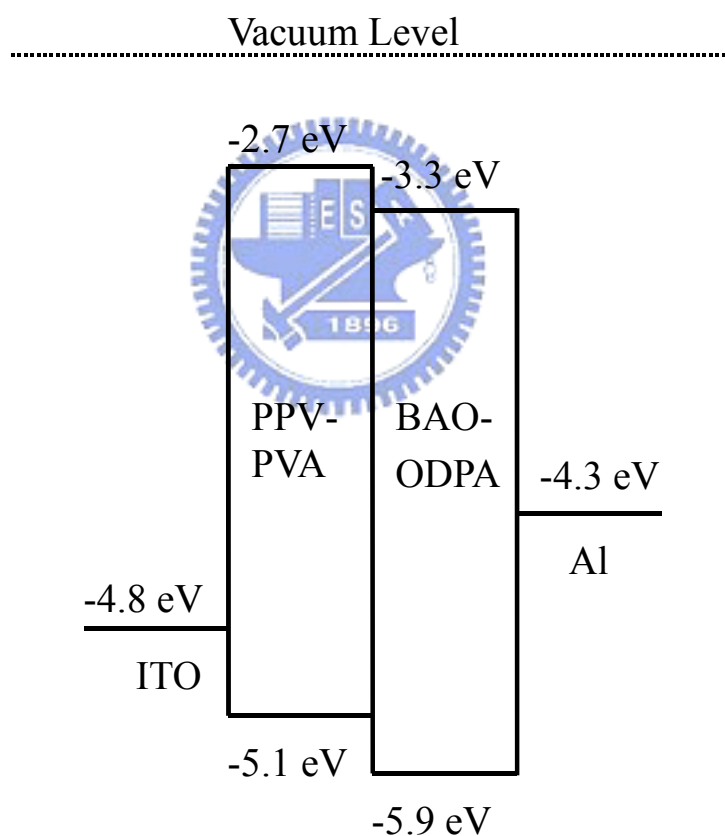


Figure 2.11 Band diagram of ITO/PPV-PVA/BAO-ODPA/Al LED device.

## 2.4 Conclusions

A series of BAO-based APIs have been synthesized. These APIs exhibit obvious fluorescent behavior and the intensities decrease with increasing the crystalline degree. It suggests that high crystalline degree would decrease the population of the imide rings-aminophenyl rings face-to-face stacking. Hence, the CT interactions and fluorescence intensity would be reduced. The resultant APIs not only can be a light-emitting layer in a single layer LED, but also act as an electron transport and an electron/hole blocking layer in a double layer PPV-PVA based LED. The incorporation of BAO-ODPA layer into the PPV-PVA LED provides a significant improvement in the EL efficiency by two order of magnitude.



## References

---

- [58] M. K. Ghosh and K. L. Mittal, *Polyimides: Fundamentals and Applications*, Marcel Dekker: New York, 1996.
- [59] E. D. Wachsman, C. W. Frank, *Polymer* 1988, **29**, 1191.
- [60] H. Luo, L. Dong, H. Tang, F. Teng, *Macromol. Chem. Phys.* 1999, **200**, 629.
- [61] H. Ghassemi, J. H. Zhu, *J. Poly. Sci. B: Polym. Phys.* 1995, **33**, 1633.
- [62] J. P. Lafamina, S. A. Kafafi, *J. Phys. Chem.* 1993, **97**, 1455.
- [63] M. Hasegawa, I. Mita, M. Kochi, R. Yokota, *Polymer* 1991, **32**, 3225.
- [64] L. Qinghua, Y. Takashi, H. Kazutuki, Y. Hiroshi, *J. Polym. Sci. A: Polym. Chem.* 1998, **36**, 1329.
- [65] H. Masatoshi, J. Ishii, Y. Shindo, *J. Poly. Sci. B: Polym. Phys.* 1998, **36**, 827.
- [66] L. Weijin, A. F. Marye, *J. Phys. Chem. B.* 1997, **101**, 11068.
- [67] H. Masatoshi, J. Ishii, Y. Shindo, *Macromolecules* 1999, **32**, 6111.
- [68] C. S. Ha, H. D. Park, C. W. Frank, *Chem. Mater*, 2000, **12**, 839.
- [69] M. Hasegawa, K. Horie, *Prog. Polym. Sci.* 2001, **26**, 259.
- [70] J. W. Yu, C. S. P. Sung, *Macromolecules* 1997, **30**, 1845.
- [71] R. Jakubiak, C. J. Collison, W. C. Wan, *J. Phys. Chem. A.* 1999, **103**, 2394.
- [72] S. Setayesh, A. C. Grimsdale, T. F. Weil, *J. Am. Chem. Soc.* 2001, **123**, 946.
- [73] R. D. Scurlock, B. J. Wang, P. R. Ogilby, *J. Am. Chem. Soc.* 1995, **117**, 10194.
- [74] T. Zyung, J. Kim, *Appl. Phys. Lett.* 1995, **67**, 3420.
- [75] Y. Kim, J. G. Lee, D. K. Choi, Y. Y. Jung, B. Park, *Synth. Met.* 1997, **91**, 329.
- [76] Y. F. Wang, T. M. Chen, K. Okada, M. Uekawa, T. Nakaya, M. Kitamura, H. Inoue, *J. Polym. Sci. A: Polym. Chem.* 2000, **38**, 2032.
- [77] Y. Kim, J. G. Lee, K. J. Han, H. K. Hwang, *Thin Solid Films* 2000, **363**, 263.
- [78] J. G. Lee, S. Kim, D. K. Choi, Y. Kim, K. Kim. *Phy. Soc.* 1999, **35**, S604.
- [79] H. O. Ha, W. J. Cho, C. S. Ha, *Mol. Cryst. Liq. Cryst.* 2000, **349**, 443.
- [80] J. G. Lee, Y. Kim, S. H. Jang, S. N. Kwon, *Appl. Phys. Lett.* 1998, **72**, 1757.
- [81] E. I. Maltsev, M. A. Brusentseva, V. A. Kolesnikov, *Appl. Phys. Lett.* 1997, **71**, 3480.
- [82] E. I. Maltsev, V. I. Berendyaev, M. A. Brusentseva, *Polym. Int.* 1997, **42**, 404.
- [83] W. Y. Ng, X. Gong, W. K. Chan, *Chem. Mater.* 1999, **11**, 1165.
- [84] A. P. Wu, T. Akagi, M. Jikei, M. Kakimoto, *Thin Solid Films* 1996, **273**, 214.
- [85] P. Posch, M. Thelakkat, H. W. Schmidt, *Syn. Met.* 1999, **102**, 1110.
- [86] I. K. Spiliopoulos, J. A. Mikroyannidis, *Macromolecules* 1998, **31**, 515.
- [87] S. M. Pyo, S. I. Kim, T. J. Shin, *Macromolecules* 1998, **31**, 4777.
- [88] S. M. Pyo, S. I. Kim, T. J. Shin, M. Ree, *Polymer* 1998, **40**, 125.

- [89] Y. Kim, J. G. Lee, D. K. Choi, Y. Y. Jung, *Synth. Met.* 1997, **91**, 329.
- [90] Y. Kim, W. J. Cho, C. S. Ha, *Mol. Cryst. Liq. Cryst.* 1997, **294**, 329.
- [91] T. Matsumoto, K. Nishimura, T. Kurosaki, *Eur. Polym. J.* 1999, **35**, 1529.
- [92] W. Lu, J. P. Gao, Z. Y. Wang, G. G. Sacripante, *Macromolecules* 1999, **32**, 8880.
- [93] E. I. Mal'tsev, M. A. Brusentseva, V. I. Berendyaev, *Mendeleev Commun.* 1998, **1**, 31.
- [94] W. P. Chang, W. T. Whang, *Polymer* 1996, **37**, 3493.
- [95] D. Wilson, P. Hergenrothe, H. D. Stenzenberger, *Polyimides*; Chapman & Hall, London, 1990.
- [96] M. Zheng, L. Ding, P. M. Lahti, F. E. Karasz, *Macromolecules* 2001, **34**, 4124.
- [97] X. Zhan, Y. Liu, X. Wu, S. Wang, D. Zhu, *Macromolecules* 2002, **35**, 2529.
- [98] S. Numata, K. Fujisaki, N. Kinjo, *Polymer* 1987, **28**, 2282.
- [99] Z. Peng, J. Zhang, *Chem. Mater.* 1999, **11**, 1138.



# *Chapter 3*

## **Vapor Deposition Polymerization of Aromatic Polyimides for Electroluminescent Devices**



### 3.1 Introduction

Conventionally a polyimide (PI) thin film is usually prepared from its soluble precursor polymer solution by spin coating or casting. There are some disadvantages by using this wet process. First of all, it is difficult to remove impurities from monomers and solvents causing formation of microvoids or pinholes in thin films <sup>[1-6]</sup>. Second, these impurities or defects may reduce or destroy the luminescent efficiency of devices. In addition, the film thickness and thickness uniformity are hard to control. The vapor deposition polymerization (VDP) method can overcome the disadvantages of the wet processes. This dry process may generate fewer impurities so that the film thickness and surface smoothness can be easier controlled.

There are only few research papers about the preparation of PI-based light-emitting diodes (LED) via VDP have been reported. J. H. Jou et al. <sup>[1]</sup> prepared single-layer molecularly doped electroluminescent polymer by co-evaporating pyromellitic dianhydride (PMDA), 4,4'-oxydianiline (ODA), *N,N'*-Bis(3-methylphenyl)-*N,N'*-diphenylbenzidine (TPD) and 8-Hydroxyquinoline aluminum salt (Alq<sub>3</sub>). In this case, polyimide is used as a binder but not an active light emitting material. Kim's group <sup>[2]</sup> reported the polyimide as a hole-transporting layer with newly synthesized diamine containing TPD moiety.

In this chapter, aromatic polyimide acting as an active emitting layer in LED device was studied. The poly(amic acid)s are prepared from 2,5-Bis(4-aminophenyl)-1,3,4-oxadiazole (BAO) and 4,4'-(9-fluorenylidene)dianiline ( BAPF ) by vapor deposition polymerization with 4,4'-(Hexafluoroisopropylidene)diphthalic anhydride ( 6FDA ). They were then thermally converted into PIs. The 6FDA was used according to the study in last chapter, that the PIs made from 6FDA exhibited lower driving voltage than other common dianhydrides <sup>[7]</sup>. Oxadiazole-base conjugated polymers are very attractive as active components in LED due to their high electron affinity. Aromatic oxadiazole compound BAO provided the electron-transporting and hole-blocking properties. BAPF is the conjugated materials composed of fluorene and aromatic rings. Fluorene derivatives have shown thermal and chemical stability and high fluorescence quantum yield in the solid state. Therefore, the PIs from BAPF and BAO with 6FDA were expected to exhibit excellent electroluminescence by using vapor deposition polymerization.

## 3.2 Experimental section

### 3.2.1 Materials

The monomer structures and the reaction route are shown in Figure 3.1. 2,5-Bis(4-aminophenyl)-1,3,4-oxadiazole (BAO, 98%) from Lancaster, 4,4'-(hexafluoro-iso-propylidene)diphthalic anhydride (6FDA, purity >99.99%) and 4,4'-(9-fluorenylidene)dianiline (BAPF) from Aldrich without further purification were first dried in a vacuum oven at 120°C for 3 hours.

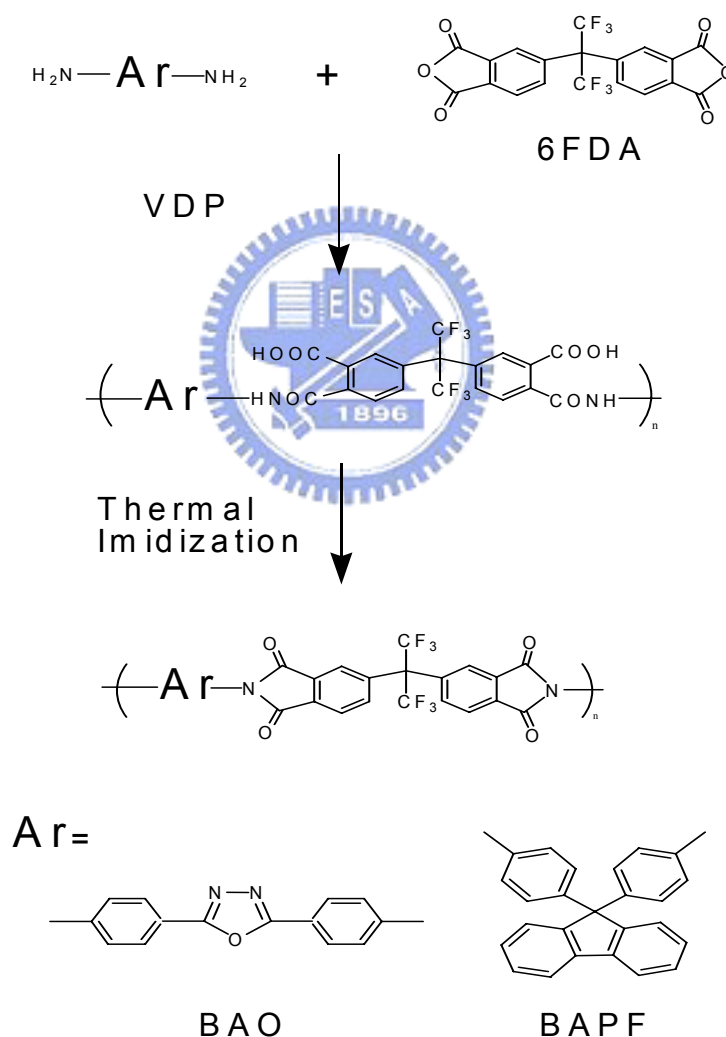


Figure 3.1 Monomer structures and the preparation route of PIs.

### 3.2.2 Vapor deposition polymerization

Poly(amic acid) films were prepared from two kinds of diamines: BAO and BAPF reacting with 6FDA by vapor deposition polymerization on the precleaned ITO glass. The deposition rate was controlled by the boat temperature. BAO or BAPF and 6FDA were vapor co-deposited on a ITO glass from the tantalum boats in a vacuum chamber of  $5 \times 10^{-6}$  torr at the deposition rate of 1 Å/sec. Thermal imidization was then carried out in a furnace at 100 °C for 1h and 250 °C for 2h under vacuum. The PI films with varied thickness, 150 Å, 300Å, 600Å and 800Å, were prepared. The metal Al was finally evaporated on the surface of the PI films to form ITO/PI/Al light-emitting device.

### 3.2.3 Characterization

Fourier transform infrared (FTIR) spectra were measured with Nicolet Protégé 460. Photoluminescence (PL) spectra were measured by using HITACHI F-4500 Spectrofluorophotometer with the excitation source at 355 nm. The UV-Vis spectroscopy was taken by HP8453 UV-Vis spectrometer. The energy level of electronic structure of the polymers was determined by UV-Vis absorption spectra and the data of cyclic voltammetry were measured by using CHI600A Electrochemical Analyzer. The cyclic voltammetry was carried out by using Pt counter electrode and a Ag/Ag<sup>+</sup> reference at the scan rate of 10 mv/s. The electrolyte was 0.1 M of tert-BuNClO<sub>4</sub> in acetonitrile. The results were compared with a ferrocene/ferrocenium (FOC) couple measured in the same solution. The deposition rates and film thickness were monitored by using Maxtek MDC-360 quartz oscillation thickness monitor in deposition. The real thickness was measured by Alpha Step Dektak ST surface profiler. The calibration curve of real thickness vs quartz oscillation thickness was then used in the following deposition to get the correct thickness. The electroluminescence (EL) spectra were measured by using Jasco FR-770 spectrometer. The current-voltage characteristics of the LEDs were measured by Keithley 237 electrometer. The intensity-voltage characteristics were measured by a Keithley 237 electrometer and a photodiode detector connected with a New Port power meter (Model 1815-C). Atomic force microscopy (AFM) images were obtained by using Digital NanoscopeE+AFM at the scan rate of 1Hz. All measurements were carried out at room temperature.



### 3.3 Results and discussion

Figure 3.2 shows the FTIR spectra of the PI thin films before and after imidization. Both as-deposited films show the absorption peaks at  $1850\text{ cm}^{-1}$ , and  $1780\text{ cm}^{-1}$  due to the carboxylic anhydride. This indicates that the monomers in as-deposited films still unreacted even at the deposition rate ratio of 1:1. After imidization, the peaks of the dianhydride at  $1850\text{ cm}^{-1}$  and  $1780\text{ cm}^{-1}$  disappear, and new absorption peaks at  $1780\text{ cm}^{-1}$ ,  $1720\text{ cm}^{-1}$  and  $1380\text{ cm}^{-1}$  appear; these peaks are associated with the characteristic absorption of the imide group. The former two peaks are due to the asymmetric and symmetric C=O stretching and the last peak is associated with the C-N stretching. Judging from the IR spectra, no dianhydride groups are left after imidization.

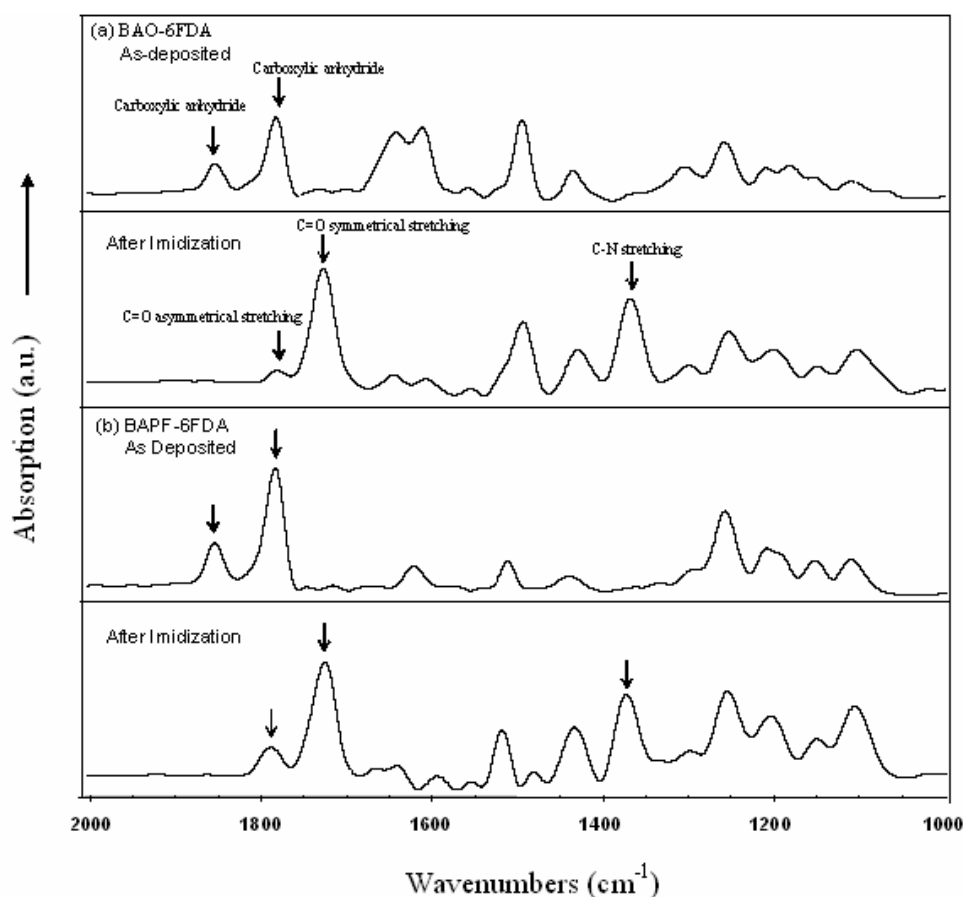


Figure 3.2 FT-IR spectra of PI thin films (a) BAO-6FDA and (b) BAPF-6FDA before and after imidization.

Figure 3.3 shows the surface morphology of PI thin films obtained from two different processes: VDP and spin coating. For the samples prepared by vapor deposition, the root mean-squared (RMS) roughnesses of the BAO-6FDA (800Å) and BAPF-6FDA (800Å) are 8.8Å and 4.7Å, respectively. While for those prepared by wet coating, the RMS roughness of the BAO-6FDA (800Å) is 37.1Å [7]. The VDP PI film has smaller the RMS value of the surface roughness. Apparently VDP process is the better way to produce smooth PI thin film than the wet coating process.

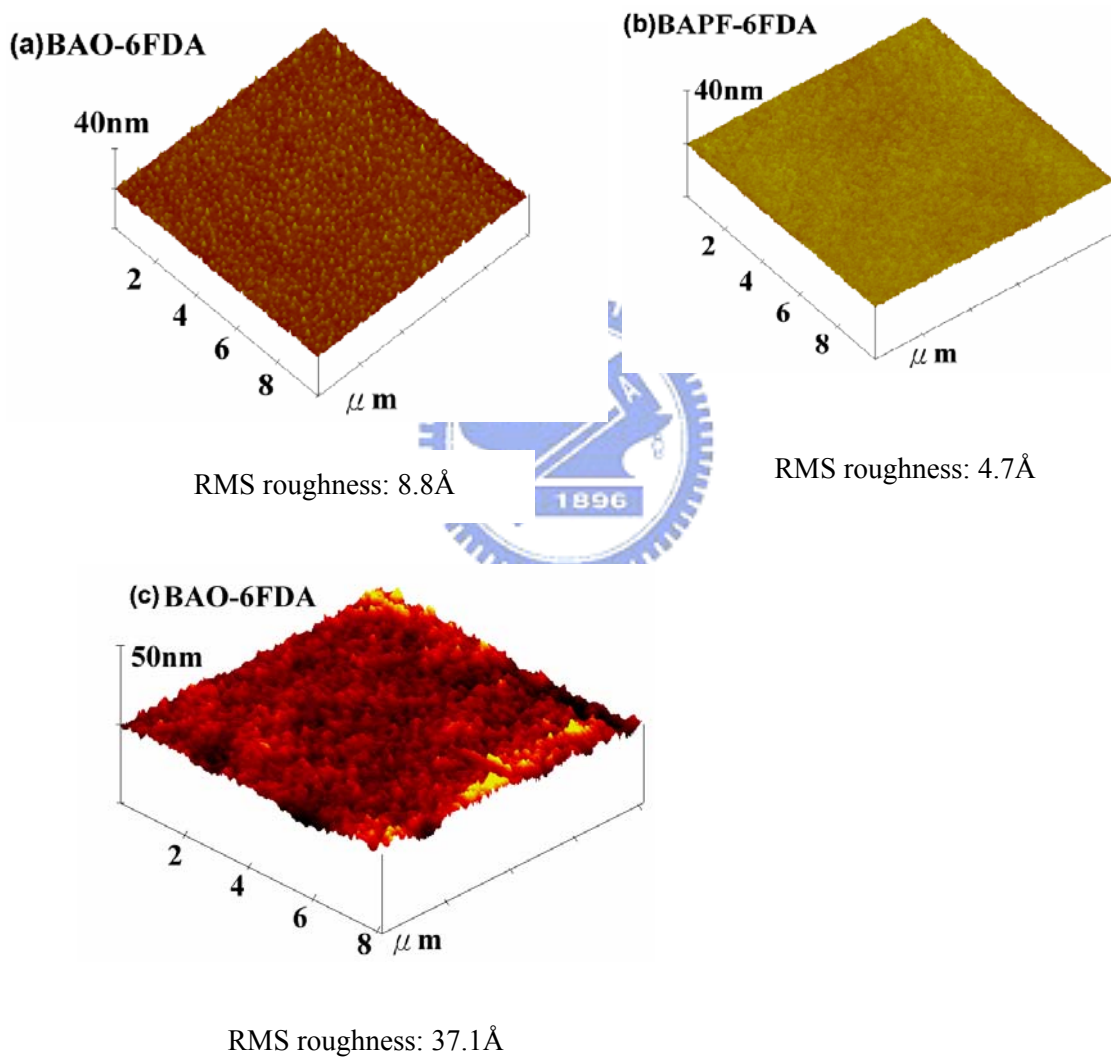


Figure 3.3 Surface morphologies of the PI thin films (800Å) (a) BAO-6FDA and (b) BAPF-6FDA by vapor deposition; (c) BAO-6FDA by wet coating.

Figure 3.4 shows the UV-Vis absorption spectra of the PI thin films. Absorption of BAO-6FDA ranges from 280 nm to 400 nm with the absorption peak at 306 nm. Absorption of BAPF-6FDA ranges from 280 nm to 450 nm with the absorption peak at 302 nm. The onsets of UV-Vis absorption are located at 370 nm and 429 nm for BAO-6FDA and BAPF-6FDA, respectively. The onset of UV-Vis absorption is used to calculate the energy gap between the highest occupied molecular orbital (HOMO) and the lowest occupied molecular orbital (LUMO). The corresponding energy gaps are 3.35 eV and 2.89 eV, respectively.

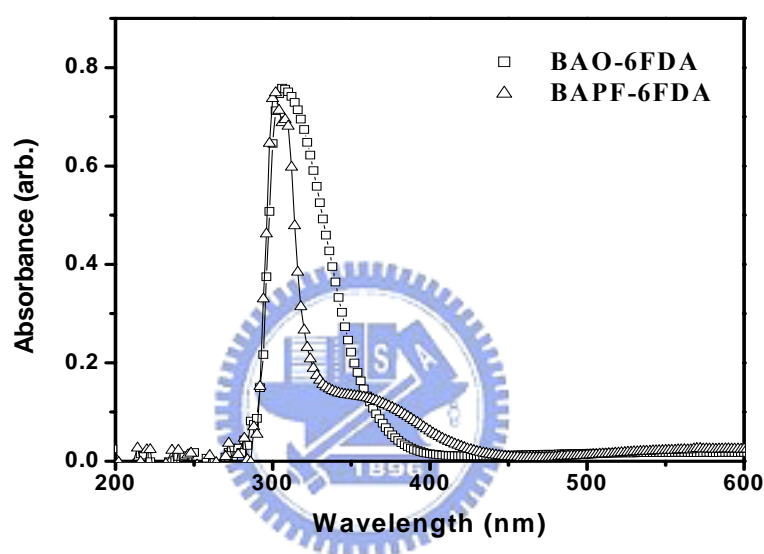


Figure 3.4 UV-Vis absorption spectra of BAO-6FDA and BAPF-6FDA PI thin films.

Figure 3.5 shows the EL spectra of the PI LED ITO/PI/Al for the BAO-6FDA and BAPF-6FDA. Both devices show broad EL spectra. The emissive peaks are located at 550 nm and 530 nm with the full-width half maximum (FWHM) of 196 nm and 135 nm for BAO-6FDA and BAPF-6FDA PI films, respectively. The emission of BAO-6FDA PI film is broader and shifts towards longer wavelength compared with that of BAPF-6FDA PI film. Both LED devices give uniform light emission when a DC positive voltage is applied to the ITO electrode.

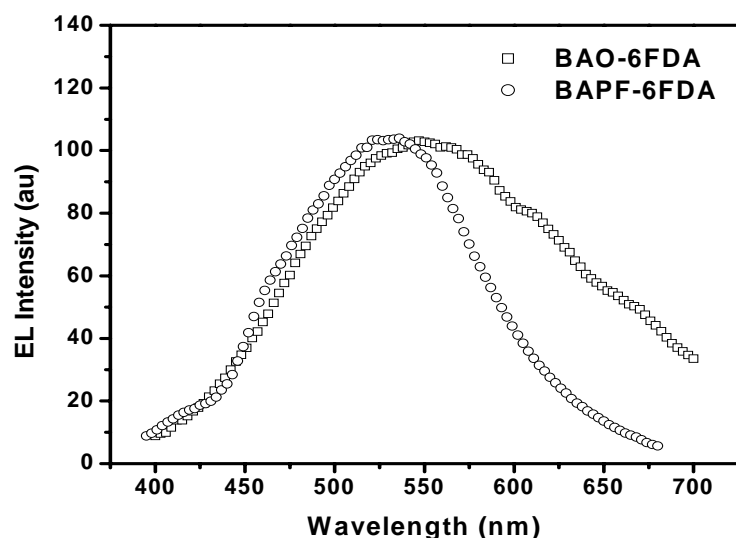


Figure 3.5 Electroluminescent spectra of PI-LED devices: ITO/BAO-6FDA/Al and ITO/BAPF-6FDA/Al.

Figures 3.6 and 3.7 present the current density-voltage (I-V) and brightness-voltage (B-V) characteristics for single-layer ITO/PI/Al LED with three different PI film thicknesses. The I-V curves of both devices (Figure 3.6a and 3.7a) show the characteristics of typical Schottky-type diode. The threshold voltages of ITO/BAO-6FDA/Al single-layer device are about 4.5V, 6V and 17V for thickness of 150Å, 300Å, and 600Å, respectively (Figure 3.6b). ITO/BAPF-6FDA/Al single-layer devices show the threshold voltage 6.5V, 8V and 18V for thickness of 150Å, 300Å and 600Å respectively (Figure 3.7b). The current density of the latter devices is much lower. The EL efficiency of single-layer devices can be evaluated from the slope of the brightness versus current density in Figure 3.8. It is found that thicker PI films exhibit higher efficiencies for both devices, and BAPF-6FDA LED has a higher EL efficiency than BAO-6FDA LED although the former has a higher threshold voltage.

Many papers have revealed that wholly aromatic PI show a broad fluorescence originating from intermolecular charge transfer (CT) complex <sup>[8-12]</sup>. The charge at HOMO and LUMO is localized at the electron-donating aminophenyl fragment and the electron-accepting imide fragment. This means charge transfer can occur via the electron HOMO to LUMO transition, and CT can be improved by higher electron-acceptability of dianhydrides and higher electron-donatability of diamines as monomers <sup>[11]</sup>. The electron-drawing oxadiazole in diamine decreases the

electron-donability of BAO, and also reduces the CT effect. It results in the lower efficiency of BAO-6FDA LED than that of BAPF-6FDA LED. Besides, CT is also affected by the concentration. Increase in concentration leads to increase in the amount of intermolecular CT sites<sup>[12]</sup>. That could be the reason that thicker PI films show higher EL efficiency.

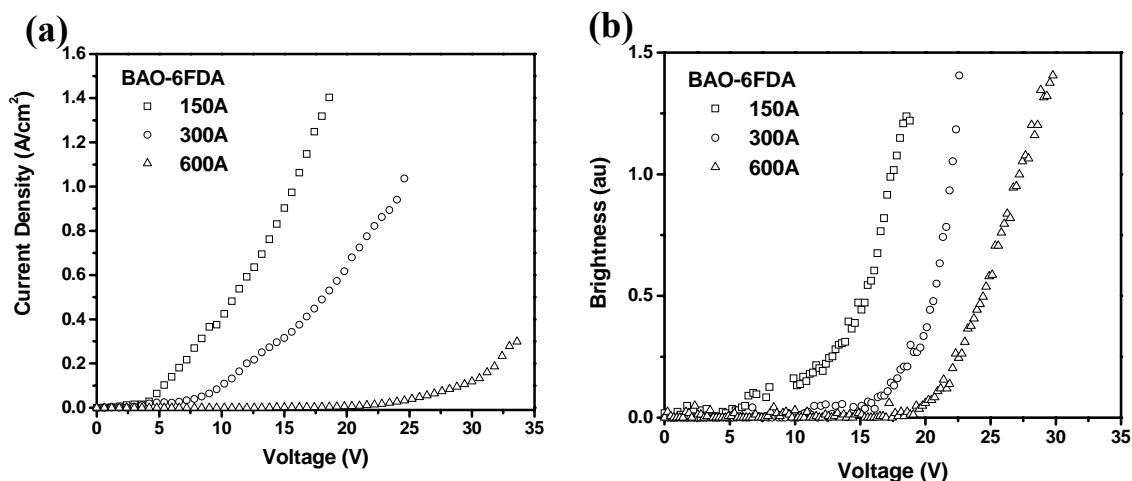


Figure 3.6 (a) Current density-voltage and (b) brightness-voltage characteristics of PI-LED devices ITO/BAO-6FDA/Al with different PI thickness: 150Å, 300Å and 600 Å.

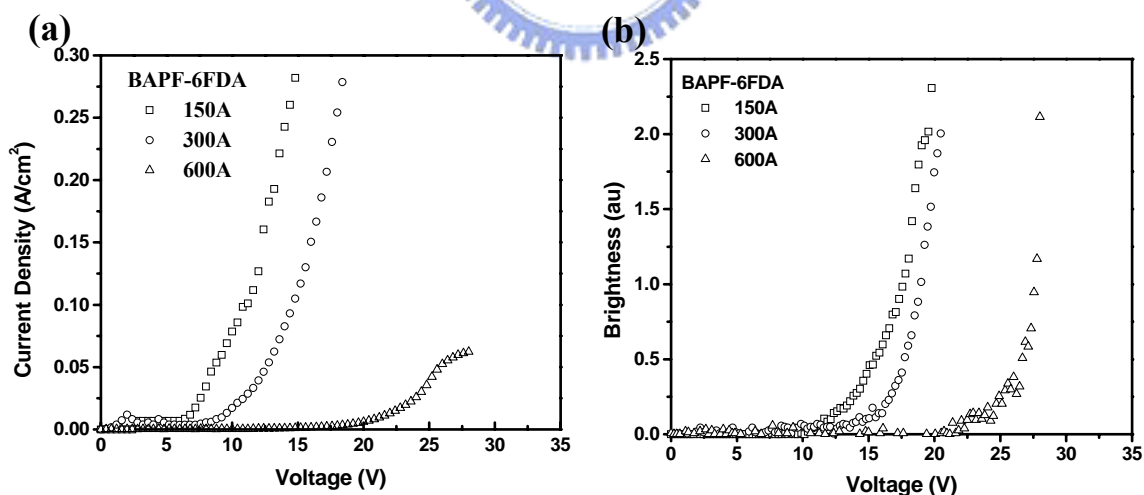


Figure 3.7 (a) Current density-voltage and (b) brightness-voltage characteristics of PI-LED devices ITO/BAPF-6FDA/Al with different PI thickness: 150Å, 300Å and 600 Å.

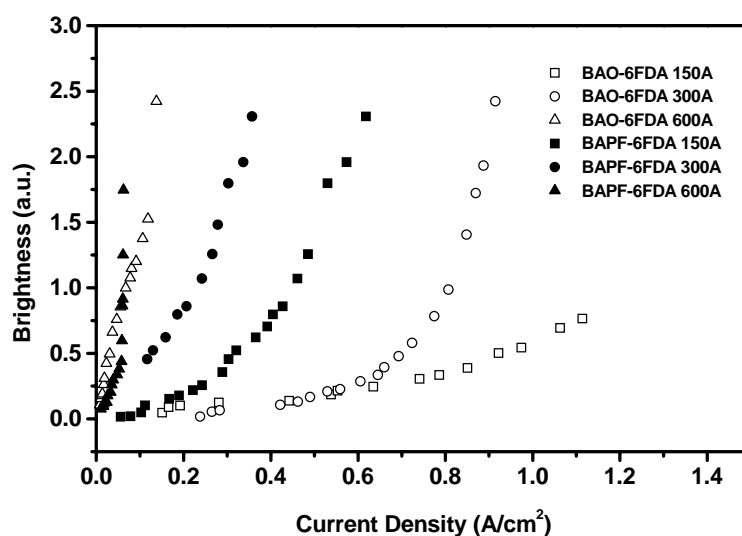


Figure 3.8 Brightness-current density characteristics of PI-LED devices with different PI thickness

Cyclic Voltammetry is a useful tool to study the electrochemical properties and energy level of charge transport materials. Figure 3.9 shows the cyclic voltammograms of polyimide thin films. For BAPF-6FDA and BAO-6FDA, the onset of oxidation ( $E_{ox}$ ) occurred at 1.04V and 1.71V respectively, and the onset of reduction ( $E_{re}$ ) occurred at  $-1.64V$  and  $-1.48V$  respectively. The energy levels of the PIs can be estimated from the following equation:

$$\begin{aligned} \text{HOMO} &= (-4.8 - E_{ox}) \text{ eV} \\ \text{LUMO} &= (-4.8 - E_{re}) \text{ eV} \end{aligned}$$

where the constant  $-4.8$  is the energy level of ferrocence related to the vacuum level<sup>[13]</sup>. The energy levels of two PI-LED are displayed in Figure 3.10 and summarized in Table 3.1. The energy levels of the HOMO and the LUMO are  $-6.51$  eV and  $-3.32$  eV referred to the vacuum level for BAO-6FDA;  $-5.84$  eV and  $-3.16$  eV for BAPF-6FDA. It indicates that BAO-6FDA has a lower electron injection barrier than BAPF-6FDA due to the electron transporting oxadiazole unit. On contrast, BAPF-6FDA has a lower hole injection barrier than BAO-6FDA. It is due to more hole transporting arylene structure in BAPF-6FDA. Compared the energy barrier to each electrode for both LED devices, ITO/BAPF-6FDA/Al LED exhibits the more balanced charge injection from the two electrodes (1.14 eV and 1.04 eV) than ITO/BAO-6FDA/Al LED. The energy barriers of the ITO/BAO-6FDA interface and

the BAO-6FDA/Al interface are 1.71 eV and 0.98 eV respectively. Hole injection is more difficult than electron injection in this device. The electron injection and the hole injection become imbalanced. Thus, the EL efficiency of BAO-6FDA is lower than that of BAPF-6FDA LED.

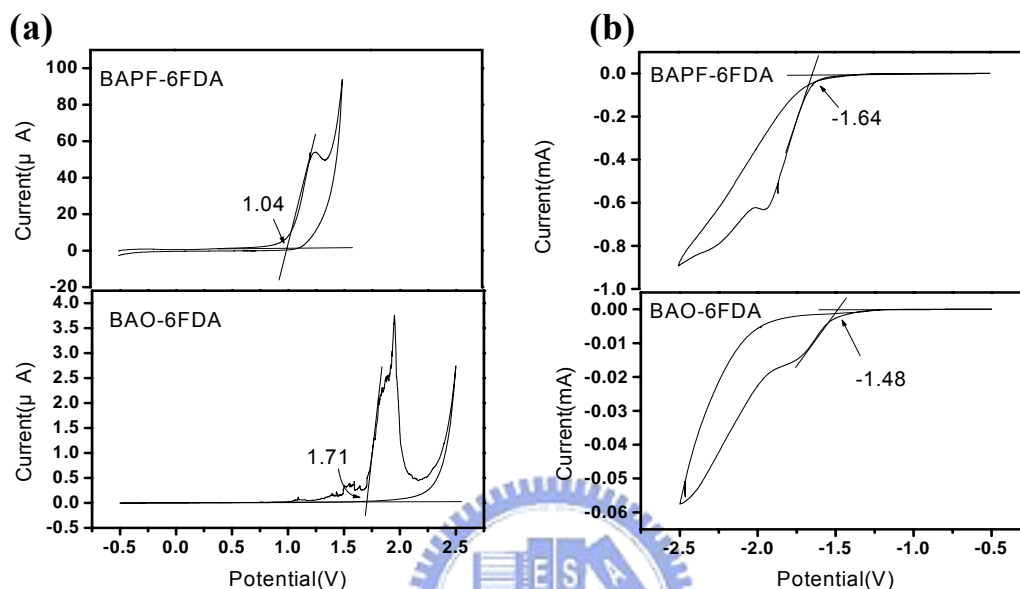


Figure 3.9 Cyclic voltammograms of polyimides (a) oxidation curves (b) reduction curves.

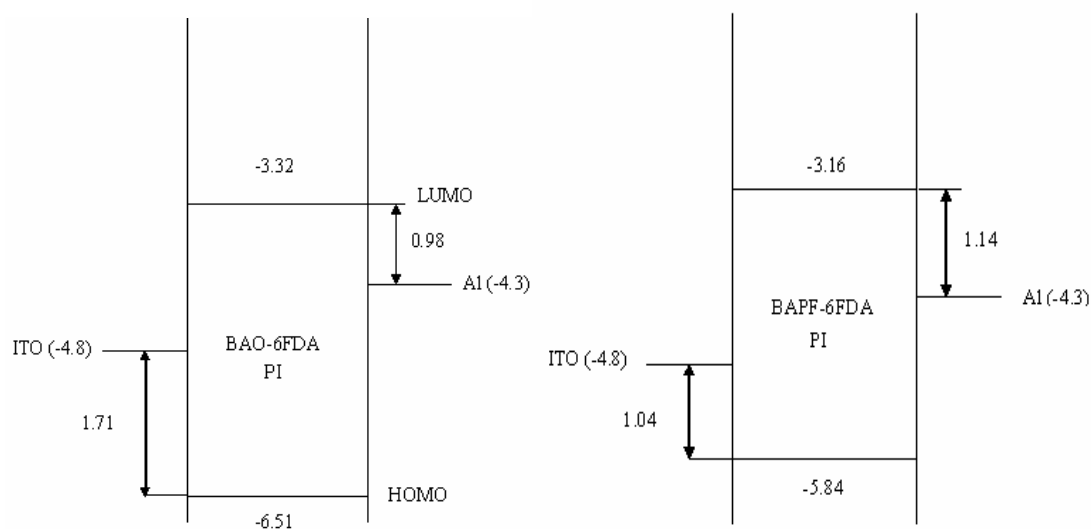


Figure 3.10 Band diagrams of ITO/BAO-6FDA/Al (left) and ITO/BAPF-6FDA/Al (right).

Table 3.1. Electrochemical potentials and energy levels of the polyimides

<b>Polymer</b>	$E_{onset}^{ox}$ vs $E_{FOC}$ (eV)	$E_{onset}^{red}$ vs $E_{FOC}$ (eV)	HOMO (eV)	LUMO (eV)	$E_{gap}$ (eV)
<b>BAO-6FDA</b>	1.71	-1.48	-6.51	-3.32	-3.19(-3.35 <sup>[a]</sup> )
<b>BAPF-6FDA</b>	1.04	-1.64	-5.84	-3.16	-2.68(-2.89 <sup>[a]</sup> )

[a]:  $E_{gap}$  stand for the band gap energy estimated from the onset wavelength of the optical absorption .

### 3.4 Conclusions

Single layer PI-LEDs have been successfully prepared by vapor deposition polymerization from diamine BAO and BAPF with dianhydride 6FDA. Using VDP process, smoother surface morphology of the LED devices can be obtained than using wet coating process. Effective active PI thin film can be performed as low as 150Å. The threshold voltage of the PI-LED decreases with decreasing thickness, which can be as low as 4.5V. Both BAO-6FDA and BAPF-6FDA single layer LED show broad EL spectra. Thicker PI film exhibits higher efficiencies in both types of LEDs. It could be resulted from the more CT sites in the thicker PI film in favor of increasing the intermolecular CT. BAPF-6FDA LED has a higher EL efficiency than BAO-6FDA LED because of the more balanced charge injection from both electrodes and the stronger intermolecular CT.



## References

---

- [100] W. K. Wen, J. H. Jou, H. S. Wu, C. L. Chen, *Macromolecules* 1998, **31**, 6515.
- [101] J. G. Lee, S. Kim, *J. Korean. Phys. Soc.* 1999, **35**, S604.
- [102] W. K. Wen, J. H. Joe, J. F. Chiou, *Appl. Phys. Lett.* 1997, **71**, 1302.
- [103] H. Yanagisita, D. Kitamoto, K. Haraya, T. Nakane, T. Tsuchiya, N. Koura, *J. Membrane Sci.* 1997, **136**, 121.
- [104] S. Ukishima, M. Iijima, M. Sato, Y. Takahashi, E. Fukada, *Thin Solid Film* 1997, **308**, 475.
- [105] G. Maggioni, S. Carturan, D. Boscarino, G. Dellamea and U. Pieri, *Mater. Lett.* 1997, **32**, 147.
- [106] C. S. Chao, W. T. Whang, S. C. Hsu (in preparation).
- [107] M. Hasegawa, I. Mita, M. Kochi, R. Yokota, *Polymer* 1991, **32**, 3225.
- [108] E. D. Wachsman, C. W. Frank, *Polymer* 1988, **29**, 1191.
- [109] J. P. Lafamina, S. A. Kafafi, *J. Phys. Chem.*, 1993, **97**, 1455.
- [110] M. Hasegawa, K. Horie, *Prog. Polym. Sci.*, 2001, **26**, 259.
- [111] H. Luo, L. Dong, H. Tang, F. Teng, Z. Feng, *Macromol. Chem. Phys.* 1999, **200**, 629.
- [112] Z. Peng, Z. Bao, M. E. Galvin, *Chem. Mater.* 1998, **10**, 2086.



# *Chapter 4*

## **Characterization of Polyimide/ZnO Nanohybrid Films**



## 4.1 Introduction

Metal or semiconductor nanoparticles dispersed in polymer matrixes have been widely studied recently <sup>[1-5]</sup>. These nanocomposites exhibit interesting properties and could be widely applied in the microelectronic and optoelectronic industries. Polyimide (PI) is a promising matrix for these nanocomposites due to its good thermal stability and chemical resistance <sup>[5-7]</sup>. In addition, the mechanical, electrical and optical properties of pure PIs can be further improved by incorporating inorganic materials.

Zinc oxide (ZnO) has attracted much attention in recent years due to its excellent physical properties, such as a wide band gap (3.37 eV) at room temperature and a large exciton bonding energy (60meV). It can be used in ultraviolet light-emitting diodes, transparent electrodes and piezoelectric devices etc <sup>[8,9]</sup>. Many different methods have been reported to fabricate ZnO nanocrystals. Spanhel and Anderson <sup>[10]</sup> reported a simple sol-gel method to prepare quantum size ZnO particles. In addition to obtain a sharp size distribution, the use of surfactant- or polymer-stabilized ZnO nanoparticles has been reported <sup>[11-13]</sup>.

Several ZnO/organic composites have been reported, such as, poly(ethylene glycol) <sup>[14]</sup>, low density polyethylene <sup>[15]</sup>, poly(ethylene oxide) <sup>[16]</sup>, Nylon-6 and poly(styrene butylacrylate) <sup>[17]</sup>. Our laboratory successfully prepared highly transparent and stably luminescent ZnO/poly(hydroxyethyl methacrylate) nanocomposites <sup>[18]</sup>. However, the inferior thermal stability of organic matrices may restrict a composite's application in the electronic and optoelectronic industries. For electronic and optoelectronic application, high reliability usually requires a highly thermally stable polymer matrix. PI is a well-know thermally stable polymer.

This chapter describes two PIs with different flexibility, 3,3',4,4'-benzophenonetetracarboxylic acid dianhydride (BTDA)/4,4'-diaminodiphenylether (ODA) and pyromellitic dianhydride (PMDA)/ODA, acting as host polymers to synthesize a series of PI/ZnO nanocomposites. The thermal, mechanical and morphology characteristics of the hybrid films were investigated. In addition, the effect of PI structures on the ZnO size and the structural variation of ZnO nanoparticles before and after thermal imidization were presented.

## 4.2 Experimental section

### 4.2.1 Materials

Zinc acetate dihydrate (99.0% purity) from Showa, lithium hydroxide monohydrate (99.0%) from TEDIA, 3-(trimethoxysilyl)propyl methacrylate (TPM, 98%) from Aldrich, absolute ethanol (99.5%) and dimethyl sulfoxide (DMSO) from Nasa, 4,4'-diaminodiphenylether (ODA, 98%), 3,3',4,4'-benzophenonetetracarboxylic acid dianhydride (BTDA, 99%) and pyromellitic dianhydride (PMDA, 99%) from TCI were used as received without further purification.

### 4.2.2 Synthesis of ZnO-TPM nanoparticles

The ZnO nanoparticle colloid with average particle size 3.2 nm was first prepared by zinc acetate dihydrate, lithium hydroxide monohydrate and absolute ethanol according to the method of Spanhel and Anderson <sup>[10]</sup>. The produced ZnO nanoparticles were further stabilized by adding TPM. The TPM (molar ration of TPM to ZnO was 1:10) was diluted in 10 ml ethanol, and then dropwise added to the ZnO nanoparticle colloid under continuous stirring. The reaction proceeded for 12h. The synthetic TPM stabilized ZnO nanoparticle solution was filtered through a 0.1 $\mu$ m glass fiber filter. The nanoparticles were washed by heptane/ethanol several times. Finally, the solvent (ethanol) of the TPM stabilized ZnO solution was replaced by the same amount of DMSO using rotary evaporation. The details of the synthesis route and characterization of the stabilized ZnO has been reported in our previous research paper <sup>[18]</sup>.

### 4.2.3 Preparation of PI/ZnO nanohybrid films

The procedure for preparation of PI/ZnO nanohybrid films was shown in Figure 4.1. The polycondensation was carried out in a flask by adding the diamine ODA (2.002g, 0.01mol) and the dianhydride BTDA (3.222g, 0.01mmol) in DMSO (30ml) under a nitrogen stream at room temperature. BTDA was added to the solution by five portions. After the dissolution of all BTDA, the reaction mixture was further stirred for 2 hours at room temperature. Various amounts of the TPM-stabilized ZnO DMSO solution were dropwise added to the poly(amic acid) solution and further stirred for

12h. The modified and unmodified poly(amic acid) solutions were cast on glass plates, and then step-heated to 100°C, 150°C and 200°C, for 1h at each temperature, and finally heated to 300°C for 2h. The PI/ZnO nanohybrid films have an average thickness of 30–35  $\mu$  m. The hybrid films of the PMDA series were prepared in a similar manner.

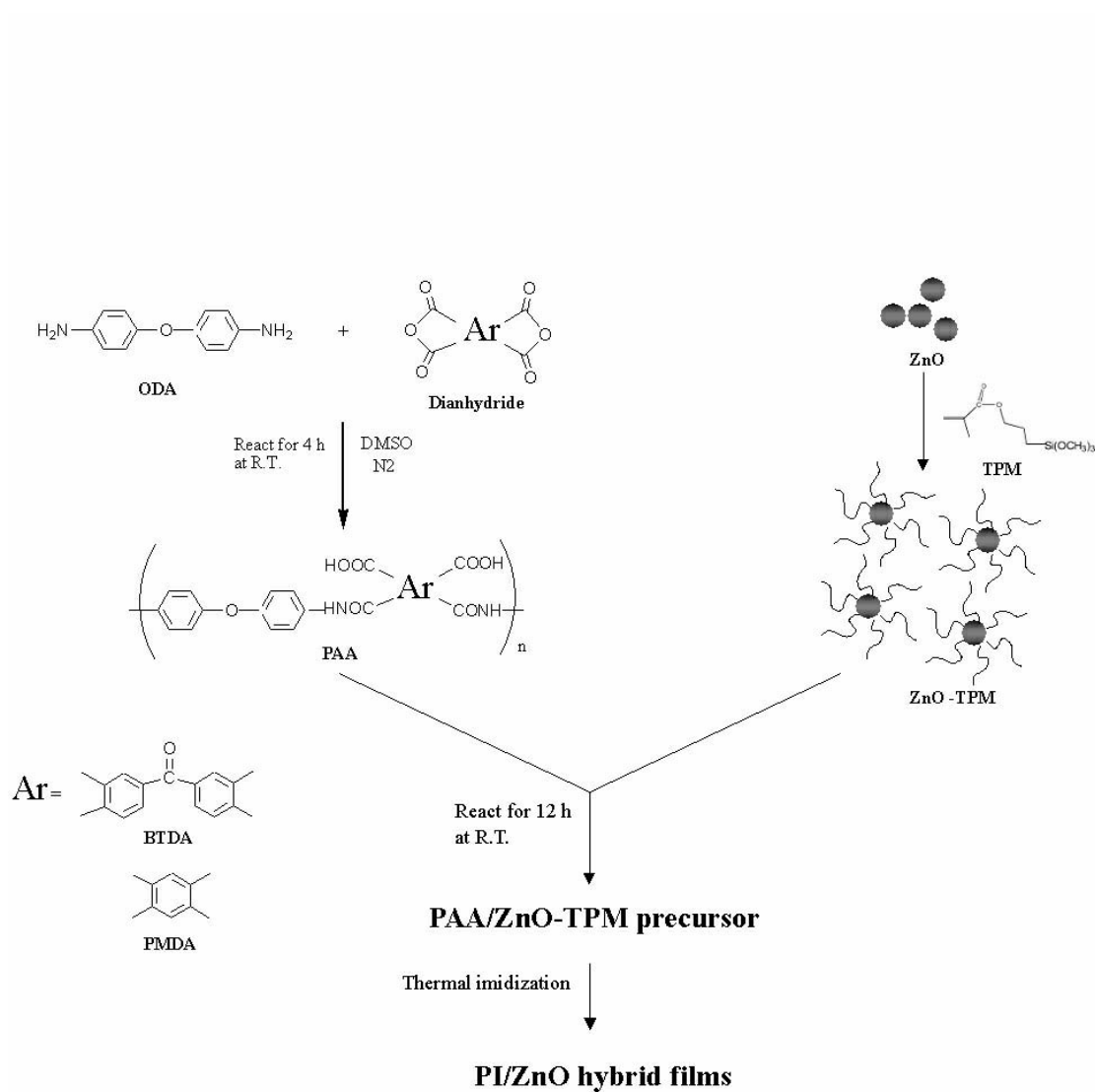


Figure 4.1 Monomer structures and the synthetic route of PI/ZnO hybrid films.

#### 4.2.4 Characterization

TA Instruments TGA 2950 was used to characterize the thermal stability and decomposition temperature of 5 wt.-% weight loss ( $T_d$ ) of the PIs at a heating rate of 20°C/min from 30 to 900°C under Nitrogen. The coefficient of linear thermal expansion (CTE) was measured by thermomechanical analysis (TMA) with a TA Instruments TMA 2940 at heating rate of 10°C/min. The glass transition temperature ( $T_g$ ) measurement was performed using a DuPont DMA Q800 Dynamic Mechanical Analyzer at 5°C/min and a frequency 1 Hz. Fourier transform infrared (FTIR) spectra were measured by Nicolet Protégé 460. The spectra of X-ray photoelectron spectroscopy (XPS) were obtained by using ESCA PHI 1600 spectrometer working in the constant analyzer energy mode with a pass energy of 50eV and MgK  $\alpha$  (1253.6 eV) radiation as the excitation source. The XPS measurement was done at room temperature and pressures below  $10^{-10}$  Torr. The take-off angle used in the XPS measurements was 90°. Transmission electron microscopy (TEM) images were performed by using a JEOL-200FX transmission electron microscope.

#### 4.3 Results and discussion

FTIR spectra of BTDA/ODA pure PI and BTDA-ODA/ZnO nanocomposites with different ZnO content are shown in Figure 4.2b–e. In Figure 4.2c–e, all the hybrid films exhibit the characteristic absorption peaks of imide group at 1772, 1719 and 1380  $\text{cm}^{-1}$ . The former two peaks are due to asymmetric and symmetric C=O stretching and the last peak is associated with the C–N stretching. The intensity of the absorption band 3200–3700  $\text{cm}^{-1}$  increases with enhancement of the ZnO content. This may be related to different state of hydrogen bonding in the hybrid films. The characteristic imide peaks (C=O) of these hybrid films are shifted toward lower wavenumber compared to that of the pure PI (Figure 4.2b). Hydrogen bond formation between the C=O of imide group and the OH group on the surface of ZnO nanoparticles can be attributed to this phenomenon<sup>[21]</sup>. In addition, the Si–O–Si or Si–O absorption at 1200–1050  $\text{cm}^{-1}$  in the TPM-stabilized ZnO nanoparticles were also found in the PI/ZnO hybrid films (Figure 4.2a). This consists with our previous study<sup>[18]</sup>, that the 3-(trimethoxysilyl)propyl methacrylate groups of TPM yield a thin layer of organic silica nanonetwork capping the ZnO nanoparticles via hydrolysis-condensation reaction.

Figure 4.3 shows the XPS wide-scan spectrum of the BTDA-ODA/ZnO-5wt.-%

hybrid film. It shows carbon, oxygen and zinc characteristic peaks. This confirms that ZnO indeed appear in the PI hybrid film. But with the different sputtering time to detect ZnO in different depth, no Si signal was ever observed in the Si core-level spectra. That is, Si was not able to be detected on the surface and in the bulk of the hybrid film. Two possibilities can explain for this: first, the TPM content on the surface of the hybrid films is too low to detect; second, the surface TPM network decomposes during thermal imidization.

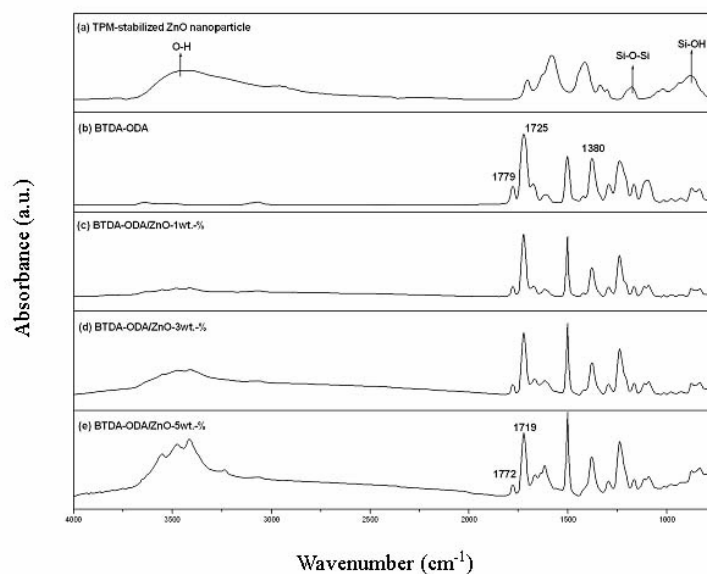


Figure 4.2 FT-IR spectra of BTDA-ODA/ZnO hybrid films.

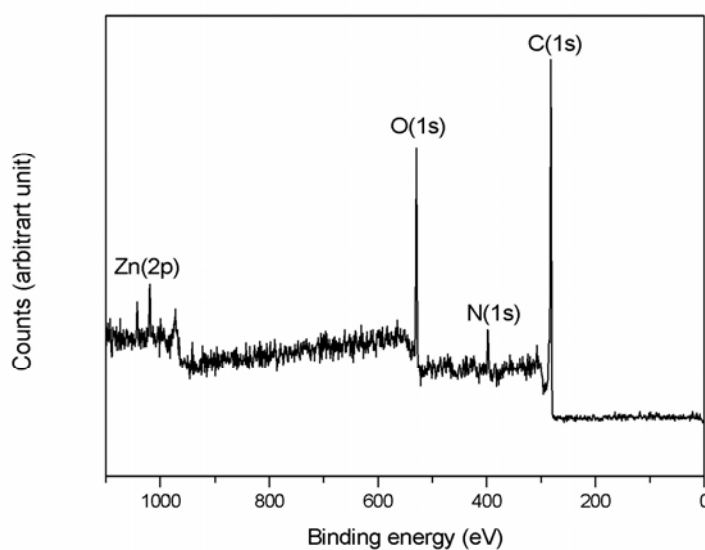


Figure 4.3 XPS wide-scan spectrum of BTDA-ODA/ZnO 5 wt.-% film.

Figure 4.4 shows thermal gravimetric profiles of the unmodified ZnO nanoparticle and TPM-stabilized ZnO nanoparticle. Both samples show obvious weight loss at temperatures between 300 to 700°C. This mass loss of the unmodified ZnO nanoparticle is attributed to desorption of acetate anions or acetic acid at the surface of the ZnO nanoparticle [20]. However, TPM-stabilized ZnO nanoparticles shows more weight loss 5 wt.-% in the range of 300–700°C comparing with unmodified ZnO nanoparticles. When further analyzed the isothermal gravimetric profiles of both samples at 300°C for 2hr under similar condition to the imidization, the data reveals that the TPM-stabilized ZnO nanoparticles show 1 wt.-% loss larger than the unmodified ZnO nanoparticles. Clearly, part of the TPM network (about 20%) decomposes during the imidization at 300°C for 2hr, but a significant portion of the TPM network stabilizer (about 80%) remains after the imidization.

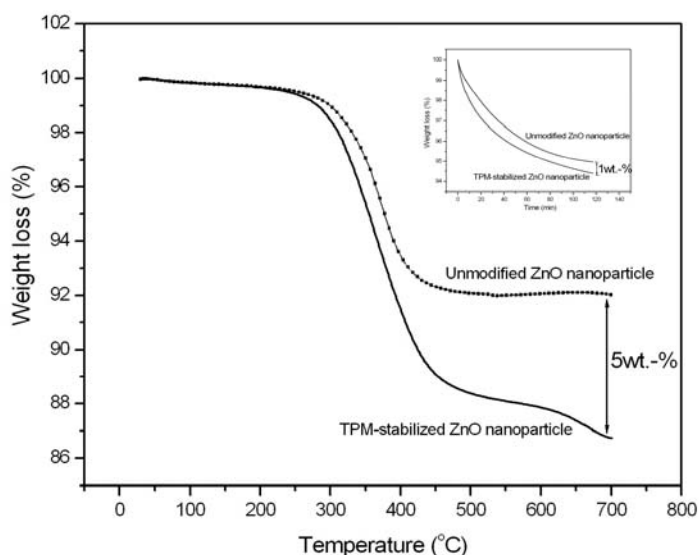


Figure 4.4 Thermal gravimetric profiles of unmodified ZnO nanoparticles and TPM-stabilized ZnO nanoparticles. The inset shows the thermal gravimetric profiles of both samples measured on 300°C isothermal 2hr.

Figure 4.5 shows core-level spectra of Zn 2p in the hybrid films with different Zn content. There are two Zn peaks identified; one at 1019 eV corresponding to Zn 2p<sub>3/2</sub>, and the other at 1042 eV is attributed to Zn 2p<sub>1/2</sub>. The peaks are slightly shifted toward lower energies compared to the spectrum of ZnO bulk (1022 and 1046 eV corresponds to the Zn2p<sub>2/3</sub> and Zn2p<sub>1/2</sub>, respectively) [9]. This shift can be attributed to the different chemical environment on the surface of ZnO nanoparticles [5,19] from



that of the bulk. In the polymer hybrid, the organic polymer component and the adsorbed organics of low surface energy dominate on the surface. It is more obviously in smaller nanoparticles. This may cause the change on the binding energy of core electrons in Zn atoms.

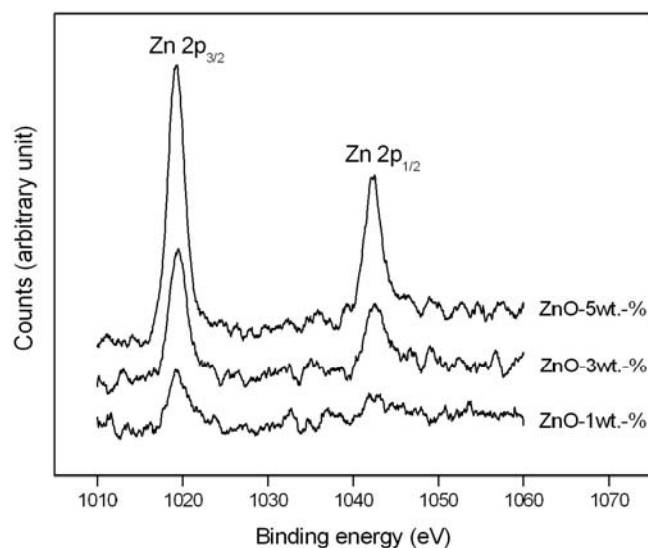


Figure 4.5 Zn 2p core-level spectra of various BTDA-ODA/ZnO hybrid films with different ZnO content.

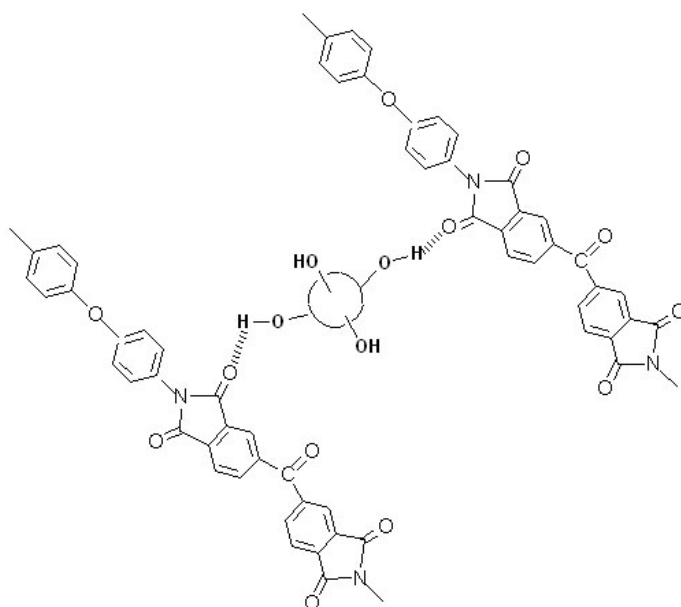


Figure 4.6 Illustration of the interaction between ZnO nanoparticles and PI chains.

According to the results of FTIR, XPS and TGA, the possible structure of the PI/ZnO nanocomposites can be inferred and is shown in Figure 4.6. The exposed OH groups on ZnO nanoparticle surface can bond to the imide group (C=O) of PI via interchain hydrogen bonding to form physical crosslinking. This creates a PI–ZnO interfacial domain with higher  $T_g$ .

Table 4.1 Coefficient of thermal expansion of pure PI and PI/ZnO nanohybrid films

ZnO content Wt.-%	BTDA/ODA		PMDA/ODA	
	CTE <sup>a</sup> (ppm/K)	CTE decreasing percentage	CTE (ppm/K)	CTE decreasing percentage
0	42.5	-	32.5	-
1	40.6	4%	25.5	21%
3	35.7	16%	17.3	47%
5	30.8	28%	b	-

a) The CTE values are determined from 50 to 250°C

b) The hybrid film was too brittle to be measured

The CTEs of the PI/ZnO nanohybrid film are listed in Table 4.1. Both series of the nanohybrid films show the CTEs decreasing with increasing ZnO content. In general, the CTEs of polymers are related to main chain free volume and relaxation<sup>[2]</sup>. For our case, ZnO nanoparticles dispersed in the PI matrix reduce the free volume of the molecular structure, and further restrict the segmental relaxation. In addition, the PMDA/ODA hybrid films show a larger CTE decrement than the BTDA/ODA hybrid films. The PMDA/ODA molecular structure is more rigid than BTDA/ODA and has denser molecular packing and less free volume. Even a small amount of 1 wt.-% ZnO nanoparticles doping significantly decreases the CTE of PMDA-ODA/ZnO hybrid film with decrement of 21%. The sample with 3 wt.-% of ZnO doping cause the CTE decrement up to 47%. On the other hand, BTDA/ODA matrix contains a kink point of C=O group in the dianhydride fragment. It disturbs chain packing and increases free volume. Hence, the percentage change in CTEs this series of hybrid film is much less than of the PMDA-ODA/ZnO hybrid film.

The dynamic mechanical analyses of PI/ZnO hybrid films are shown in Figure 4.7 and 4.8. In Figure 4.7, the storage modulus of both PMDA-ODA/ZnO and BTDA-ODA/ZnO nanohybrid films increase with enhancement of ZnO content. In

addition, all the hybrid films have a larger storage modulus than pure PI in the test temperature range. The  $\tan \delta$  curves of the all samples are shown in Figure 4.8. When increasing ZnO content, both series of hybrid films show higher transition temperatures and lower damping in comparison with the pure PI. This is due to the physical cross-linking through hydrogen bonding in the PI/ZnO hybrid film as shown in Figure 4.6. In addition, the series of BTDA/ODA hybrid films show the tendency of two damping peak (Figure 4.8a) with increasing ZnO content.

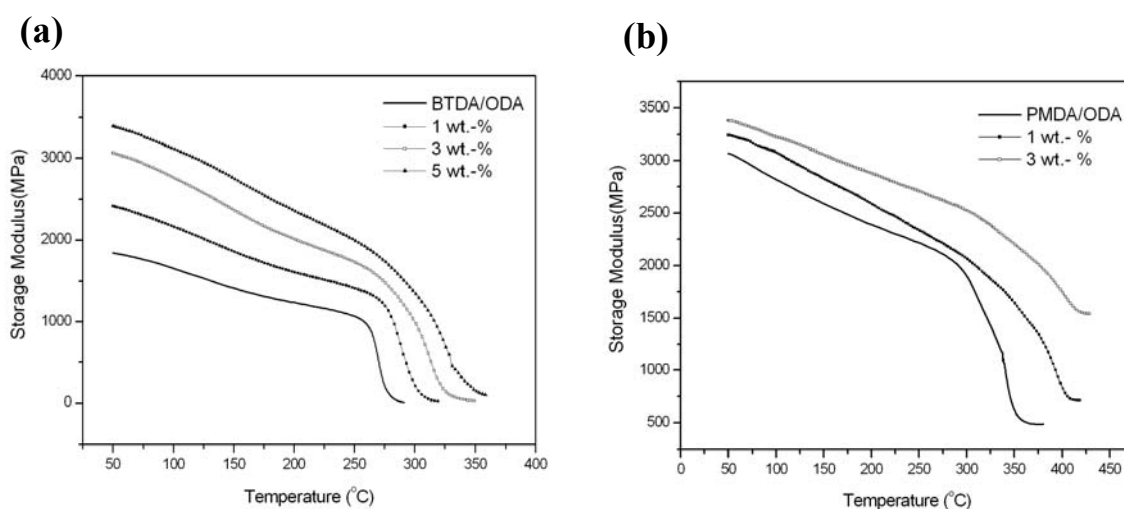


Figure 4.7 Dynamic mechanical storage moduli of BTDA-ODA/ZnO and PMDA-ODA/ZnO hybrid films.

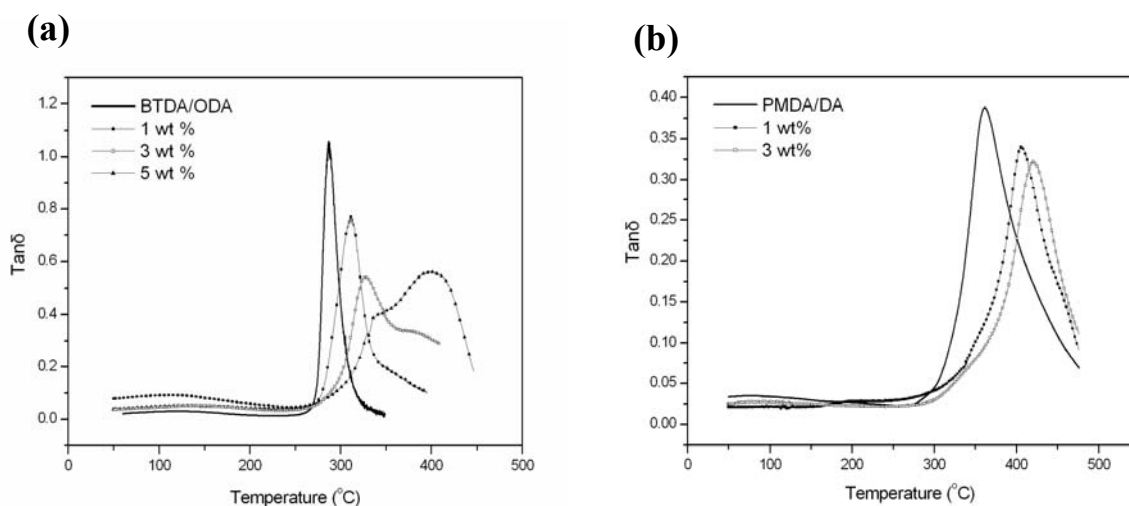


Figure 4.8 Dynamic mechanical  $\tan \delta$  curves of the PI/ZnO hybrid films BTDA-ODA/ZnO and PMDA-ODA/ZnO.

This phenomenon can be further analyzed by deconvolution of  $\tan \delta$  curves and the results are shown in Figure 4.9 and listed in Table 4.2. The  $\tan \delta$  curve of BTDA-ODA/ZnO nanohybrid films can be resolved into two curves,  $\tan \delta_1$  with  $T_{g1}$  and  $\tan \delta_2$  with  $T_{g2}$ . Both  $T_{g1}$  and  $T_{g2}$  shift to high temperature with increasing the ZnO content, and  $\tan \delta_1$  damping decreases as well as  $\tan \delta_2$  increases with ZnO content. As in our previous reported in PI/TiO<sub>2</sub> hybrid film,<sup>[6]</sup> the peaks of  $\tan \delta_1$  and  $\tan \delta_2$  are related to pure the PI matrix and the PI/inorganic interfacial domains, respectively. The virgin PMDA/ODA PI film is more rigid than BTDA/ODA and has higher  $T_g$ . It gives the chance of the two  $\tan \delta$  peaks overlap into one peak in the rigid PI/ZnO nanohybrid. Therefore, the series of PMDA/ODA hybrid films show only one  $\tan \delta$  in Figure 4.8b.

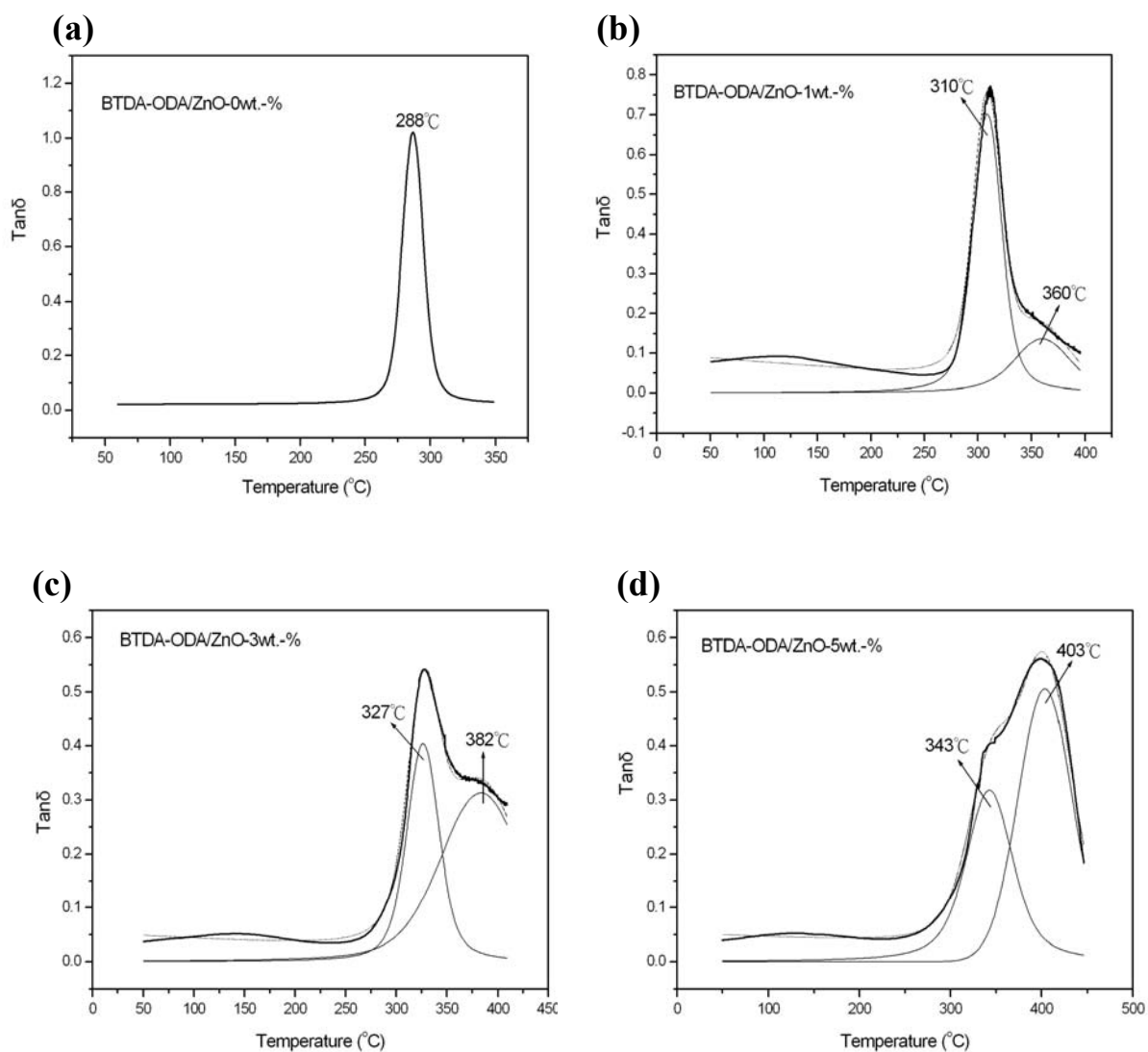


Figure 4.9 Deconvolution of  $\tan \delta$  curves of BTDA-ODA/ZnO nanohybrid films.

Table 4.2 Glass transition temperatures<sup>a</sup> of pure PI and PI/ZnO nanohybrid films

ZnO content Wt.-%	1st Transition				2nd transition	
	BTDA/ODA		PMDA/ODA		BTDA/ODA	
	$T_{g1}$ (°C)	$\Delta T_{g1}^b$ (°C)	$T_{g1}$ (°C)	$\Delta T_{g1}$ (°C)	$T_{g2}$ (°C)	$\Delta T_g^c$ (°C)
0	288	–	362	–	–	–
1	310	+22	405	+43	360	+50
3	327	+39	420	+58	382	+55
5	343	+55	d	–	403	+60

a)  $T_g$  data were determined by DMA measurement

b)  $\Delta T_{g1} = T_{g1}$  of hybrid film –  $T_{g1}$  of pure PI

c)  $\Delta T_g = T_{g2} - T_{g1}$

d) The hybrid film was too brittle to be measured

Figure 4.10a shows the thermal gravimetric profiles of the BTDA-ODA/ZnO nanohybrid films. The  $T_d$  decreases with increasing ZnO content, and shifts from 579 °C (pure BTDA/ODA) to 484 °C (5 wt.-% ZnO). The dramatic decrease in thermal stability of the hybrid films can be attributed to two reasons. First, the metallic compound-induced oxidation which causes oxidative degradation of PI films<sup>[5]</sup> and second, the desorption of the organic molecules which adsorbed at ZnO nanoparticles surfaces<sup>[20]</sup>. In Figure 4.10b, the PMDA-ODA/ZnO nanohybrid films show the similar phenomenon, but the  $T_d$  decrement is less significant as shown in Table 4.3. It seems that the rigid PMDA-ODA is more resistant to the ZnO oxidative degradation.

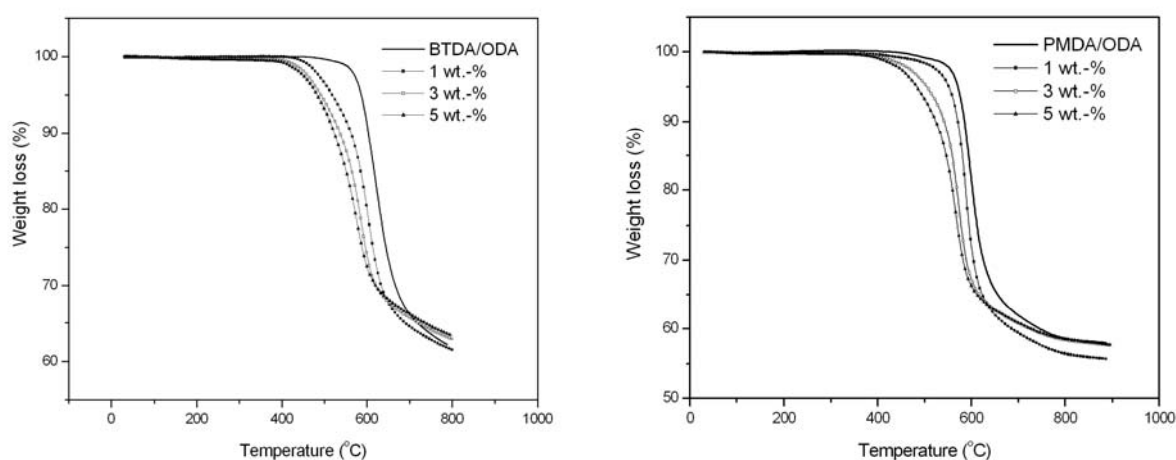


Figure 4.10 Dynamic thermal gravimetric profiles of BTDA-ODA/ZnO and PMDA-ODA/ZnO nanohybrid films.

Table 4.3 Thermogravimetric analysis of pure PI and PI/ZnO nanohybrid films

ZnO content Wt.-%	BTDA/ODA		PMDA/ODA	
	$T_d^a$ (°C)	$T_d$ decrease (°C)	$T_d$ (°C)	$T_d$ decrease (°C)
0	579	-	575	-
1	520	59	553	22
3	491	88	505	70
5	484	95	487	88

a) 5 wt.-% decomposition temperature measured under N<sub>2</sub>.

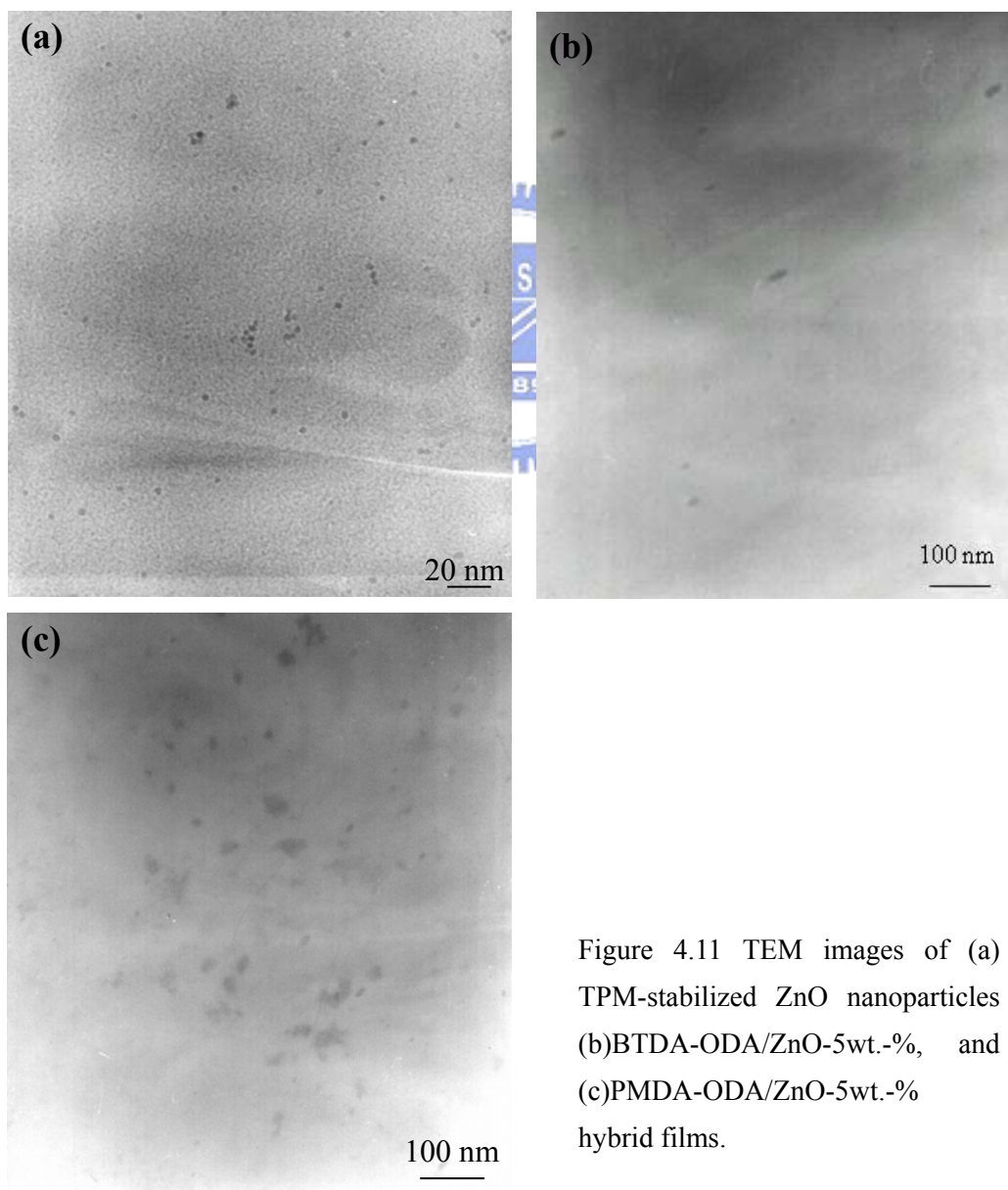



Figure 4.11 TEM images of (a) TPM-stabilized ZnO nanoparticles (b)BTDA-ODA/ZnO-5wt.-%, and (c)PMDA-ODA/ZnO-5wt.-% hybrid films.

TEM images of TPM stabilized ZnO nanoparticle, BTDA-ODA/ZnO–5wt.-%, and PMDA-ODA/ZnO–5wt.-% hybrid films are shown in Figure 4.11. The as-synthesized TPM-stabilized ZnO nanoparticle shows sphere with particle size 3–4 nm (Figure 4.11a). In Figure 4.11b, the ZnO particles show a uniform dispersion in the BTDA/ODA matrix, but the particle size is bigger (10–15 nm) than that of the as-synthesized particles, and some are elongated. The change in size and shape can be attributed to the high temperature and long time imidization process. During the period of the thermal treatment, the silica network caps are partially decomposed and released from the surface of ZnO nanoparticles. The less protected particles may develop the crystal growth of the individual self or aggregation with another resulting in change of particle size and shape<sup>[18,20]</sup>. The ZnO particles show notable aggregation as well as irregular shape in the PMDA/ODA matrix, and the average particle size (30–60 nm) is much larger than the ZnO nanoparticles in the BTDA-ODA/ZnO hybrid film. The rigid structure of PMDA-ODA causes the ZnO nanoparticle aggregation and crystal growth more easily than in BTDA-ODA, which has kink structure and more flexible.

#### 4.4 Conclusions



The data of FTIR, XPS, TGA, and DMA infer the morphology of PI/ZnO nanohybrid films being interchain hydrogen bonding between ZnO nanoparticles and PI matrix. The interchain hydrogen bonding being a kind of physical crosslinking exists in PI-ZnO interfacial domain. Owing to this physical crosslinking, the storage modulus, CTE decrement and  $T_g$  of the hybrid films can be effectively improved in comparison with that of pure PI. The improvements on these characteristics of PMDA-ODA/ZnO nanohybrid films are much more significant than that of BTDA-ODA/ZnO nanohybrid film. The physical crosslinking structure also causes BTDA-ODA/ZnO nanohybrid films having two  $T_g$ s, one for pure PI domain, the other higher  $T_g$  for the PI-ZnO interfacial domain. PMDA-ODA/ZnO nanohybrid films have only one  $T_g$  because the PMDA-ODA having high  $T_g$  cause two possible  $T_g$ s into one. Although the  $T_g$ s of the hybrid films are lower than pure PI, it is good enough for the practical application.

From TEM images, the ZnO particles show a uniform dispersion in the BTDA/ODA matrix, but most particles are bigger in size (10–15 nm) and some are elongated in comparison with as-synthetic TPM stabilized ZnO nanoparticle. It can be attributed to the high temperature and long time imidization process. However, the

aggregation and irregular shape of ZnO nanoparticles are more notable in the PMDA-ODA/ZnO hybrid film. This means that the matrix structures significantly affect the morphology and characteristic of the PI/ZnO nanohybrid films.





## References

---

- [113] K. Akamatsu, S. Ikeda, *Chem. Mater.* 2003, **15**, 2488.
- [114] C. T. Yen, W. C. Chen, *Polymer* 2003, **44**, 7079.
- [115] C. C. Chain, W. C. Chen, *Chem. Mater.* 2002, **14**, 4242.
- [116] L. Li, L. Qinghua, *Mater. Sci. Eng.* 2002, **22**, 61.
- [117] P. C. Chiang, W. T. Whang, *Polymer* 2003, **44**, 2249.
- [118] P. C. Chiang, W. T. Whang, *Thin Solid Film* 2003, **447**, 359.
- [119] P. C. Chiang, W. T. Whang, *Polymer* 2004, **45**, 4465.
- [120] C. H. Hung, W. T. Whang, *Mater. Chem. Phys.* 2003, **82**, 705.
- [121] N. S. Pesika, Z. Hu, *J. Phys. Chem. B* 2002, **106**, 6985.
- [122] L. Spanhel, M. A. Anderson, *J. Am. Chem. Soc.* 1991, **113**, 2826.
- [123] L. Guo, S. Yang, *Chem. Mater.* 2000, **12**, 2268.
- [124] E. M. Wang, P. G. Hoertz, *Langmuir* 2001, **17**, 8362.
- [125] C. G. Kim, K. Sung, *Chem. Commun.* 2003, **16**, 2068.
- [126] M. Abdullah, T. Morimoto, *Adv. Funct. Mater.* 2003, **13**, 800.
- [127] J. I. Hong, L. S. Schadler, *Appl. Phys. Lett.* 2003, **82**, 1956.
- [128] H. M. Xiong, X. Zhao, *J. Phys. Chem. B* 2001, **105**, 10169.
- [129] J. Zheng, R. W. Siegel, *J. Polym. Sci. Pol. Phys.* 2003, **41**, 1033.
- [130] C. H. Hung, W. T. Whang, *J. Mater. Chem.* (in press).
- [131] L. J. Meng, C. P. Moreira, *Appl. Surf. Sci.* 1994, **78**, 57.
- [132] V. Noack, *Chem. Mater.* 2002, **14**, 1411.
- [133] H. B. Park, J. K. Kim, *J. Membr. Sci.* 2003, **220**, 59.

# *Chapter 5*

## **Fabrication of ZnO Nanocrystals by Evaporating Oxidizing Two-step Approach**



## 5.1 Introduction

Semiconductor nanocrystals have wide application to electronic and optoelectronic devices because of their unique quantum confinement effects. In recent years, zinc oxide (ZnO) has attracted much attention due to its excellent physical properties, such as wide band gap (3.37 eV) at room temperature and large exciton bonding energy (60meV). It can be applied to ultraviolet light-emitting diodes, transparent electrodes, piezoelectric devices and so on.

Many different methods have been reported to fabricate ZnO nanocrystals: sol-gel technique <sup>[1]</sup>, chemical vapor deposition (CVD) <sup>[2]</sup>, thermal decomposition <sup>[3]</sup>, spray pyrolysis <sup>[4]</sup> and RF plasma <sup>[5]</sup>. Thermal evaporation is one of the simple ways to prepare ZnO nanostructures. Many researchers have reported using horizontal high-temperature tube furnace to fabricate different morphological ZnO nanostructures <sup>[6-11]</sup>. D. D. Yu et al. <sup>[6]</sup> have prepared ultraviolet-emitting ZnO nanowires by thermal evaporation of zinc powder mixed with selenium powder. N. Wang et al. <sup>[7]</sup> successfully synthesized ZnO nanowires, nanoribbons, and needle-like rods via thermal evaporation of a mixture of ZnO powder and graphite. Nanoribbon junction of ZnO has fabricated by using mixture of ZnO and SnO<sub>2</sub> powders as the source materials. V. A. L. Roy's group <sup>[8]</sup> has reported the morphology and luminescent properties of ZnO nanostructures prepared by thermal evaporation of Zn under different condition.

However, most preparation of ZnO nanostructures by using thermal evaporation are restricted to fabricate small amount ZnO nanostructures in a high temperature horizontal furnace. This chapter reports using a convenient thermal coater and an air-circulating to carry out thermal evaporation and oxidization processes, respectively, and successfully fabricated ZnO nanocrystals at low temperature on quartz and flexible polyimide (PI) film substrates. The structure and photoluminescence properties have been studied in this chapter.

## 5.2 Experimental section

Appropriate amounts of pure ZnO powder (99.99% purity) was placed in the W boat and thermal evaporated on quartz or PI substrates in a vacuum chamber of  $5 \times 10^{-6}$  torr. The deposition rate was controlled by the boat temperature and stabilized at 1Å/sec. The as-deposited ZnO products were further oxidized at 350°C for 2 hours in

an air-circulating. The fabricated products were analyzed by a X-ray powder diffraction (XRD) with Cu K $\alpha$  radiation (MacScience, MXP), a field-emission scanning electron microscope (FE-SEM) (Hitachi, JSM-6500F), a transmission electron microscope (TEM) (Philip, Jecnai 20), and a high resolution TEM (HRTEM) (Philip, Jecnai 20). The specimens for TEM and HRTEM were prepared by dispersing the products in methanol using an ultrasonic bath, and dropped the suspension onto a carbon film coated copper grids. The photoluminescent (PL) characteristic was measured by Hitachi F4500 spectrofluorophotometer with the excitation wavelength at 325 nm.

### 5.3 Results and discussion

Figure 5.1 shows the XRD patterns of the as-deposited and after oxidation samples. The as-deposited product displays the main diffraction peaks of metallic Zinc at  $2\theta=36.3^\circ$ ,  $39.1^\circ$  and  $43.3^\circ$ , which correspond to the (002), (100) and (101) planes of Zn hexagonal phase, and no diffraction peaks of ZnO are observed. It may suggest that Zn-O bonding of source materials would be damaged via thermal evaporating process. On the same stoichiometry, the probability which zinc atoms and oxygen atoms interact to form ZnO would be relatively low in a big vacuum chamber. Besides, oxygen atoms exhibit lighter atomic weight than zinc atoms that could be easier removed by vacuum equipments. Therefore the as-deposited products show metallic zinc features without extra oxygen supply. An air-circulating was used to further oxidize the as-deposited products. After oxidation at  $350^\circ\text{C}$  for 2h, no diffraction peaks of metallic zinc were detected. Instead, the main diffraction peaks corresponding (100), (002) and (101) planes of ZnO with a wurtzite hexagonal structure were detected. This means metallic zinc products can rapidly transformed into ZnO crystals at low temperature by using an air-circulating.

Figure 5.2 shows top view and side view FE-SEM images of the samples deposited on quartz at different deposition time, 2 min, 5 min and 10 min, and then oxidized at  $350^\circ\text{C}$  for 2h. From Figure 5.2a–c, it can be seen that the ZnO products consists of nanocrystals, and crystal aggregation become seriously with increasing the deposition time. The average sizes of crystal aggregate are 20–40 nm for 2 min deposition, 60–80 nm for 5 min and 120–150 nm for 10 min. In addition, it can be clearly seen the morphology transformation of the ZnO nanostructures by side view FE-SEM images and present in Figure 5.2d–f. When increases the deposition time from 2 min to 5 min, the morphology of ZnO nanostructures transform from island

shape into densely aggregated nanoparticles. Furthermore rod-like nanostructures were observed as deposited for 10 min.

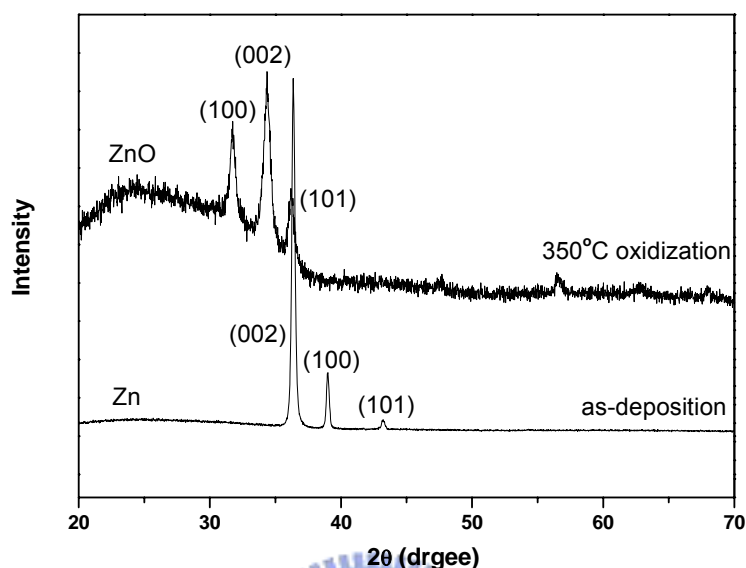


Figure 5.1 XRD pattern of ZnO samples as-deposited and after oxidized at 350°C for 2h.

Some literatures have reported the mechanism of crystal growth. Matijevic et al.<sup>[12]</sup> reported the two-stage growth, which primary particles would be formed first via nucleation and growth, and further aggregate to develop secondary particles. Oliveiva's group<sup>[13]</sup> mentioned that particles aggregation would favor c-axis probably because of crystal polarity. In the present case, it can be suggested that the morphology of ZnO nanostructures are formed before the oxidization process although the main composition of as-deposited products is metallic zinc. Metallic zinc and ZnO have the same hexagonal structure. After oxidization, oxygen atoms occupy one-half of the tetrahedral sites in zinc hexagonal structures, and then develop ZnO with wurtzite hexagonal structures. Hence only lattice volume would be increased after oxidization because of oxygen incorporation<sup>[14]</sup>.

The detailed microstructure features of ZnO nanocrystals which were deposited 10 min on quartz substrates are further studied by TEM. As shows in Figure 5.3a, the sample shows partial aggregation and the distribution are not uniform, but the average sizes of crystal aggregate were smaller than observation from FE-SEM, and no

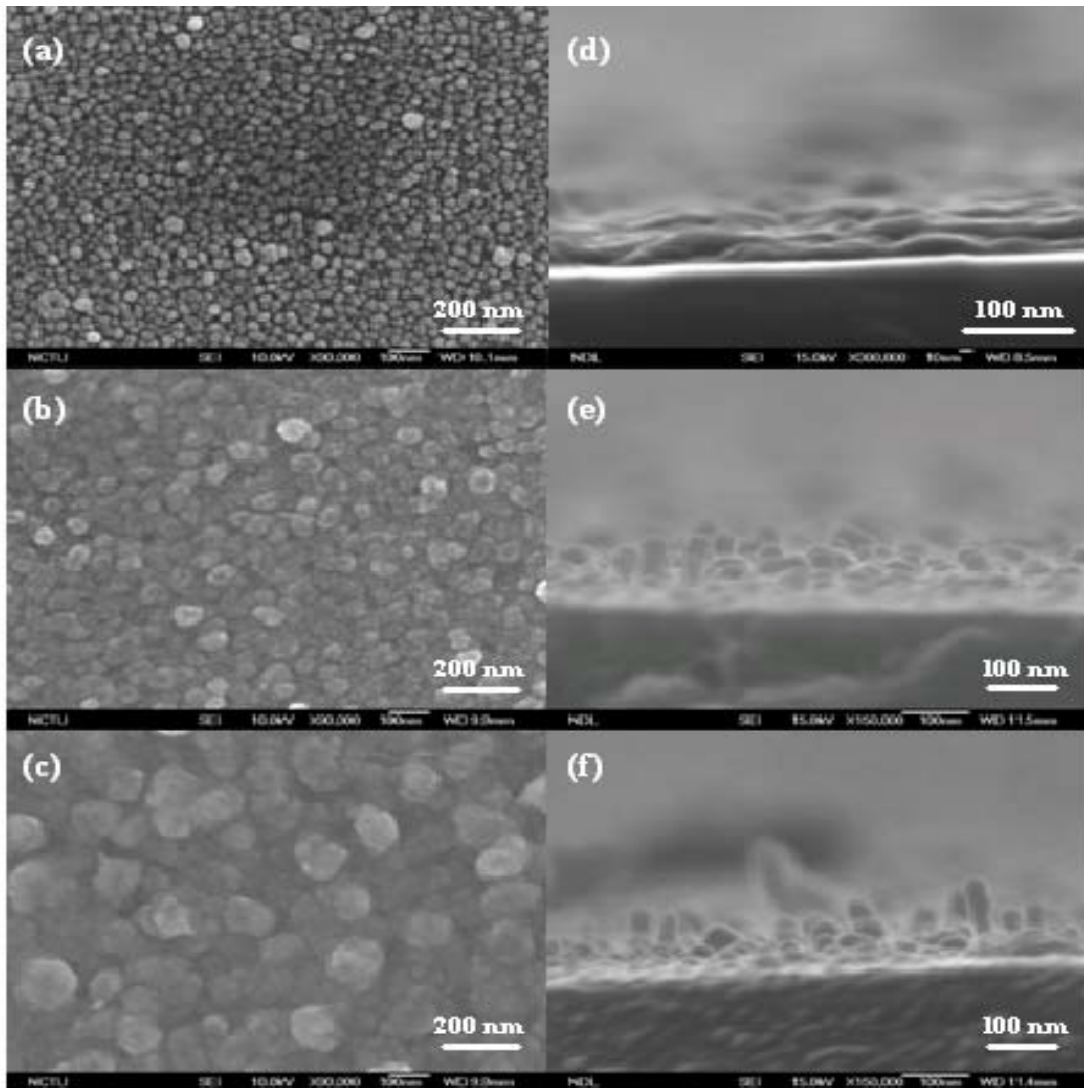


Figure 5.2 Top view (a–c) and side view (d–e) FE-SEM images of the ZnO samples fabricated on quartz substrate at three different deposition time 2 min, 5 min and 10 min, respectively, and then oxidized at 350°C for 2h.

rod-like structure was found. It suggests that an ultrasonic bath scatters the agglomerates of ZnO nanocrystals to cause loose structures. From the high magnified image (inset in Figure 5.3a) and the selected area electron diffraction pattern (inset in Figure 5.3b), the singular ZnO nanocrystal presents regular hexagonal shape and clear lattice fringes, indicating a single crystalline structure. The HRTEM images are shown in Figure 5.3b. It can be seen that the ZnO nanocrystal exhibits regular lattice order without stacking faults, and the spacing between adjacent lattice planes is about 2.6 Å, which corresponds to the (002) plane.

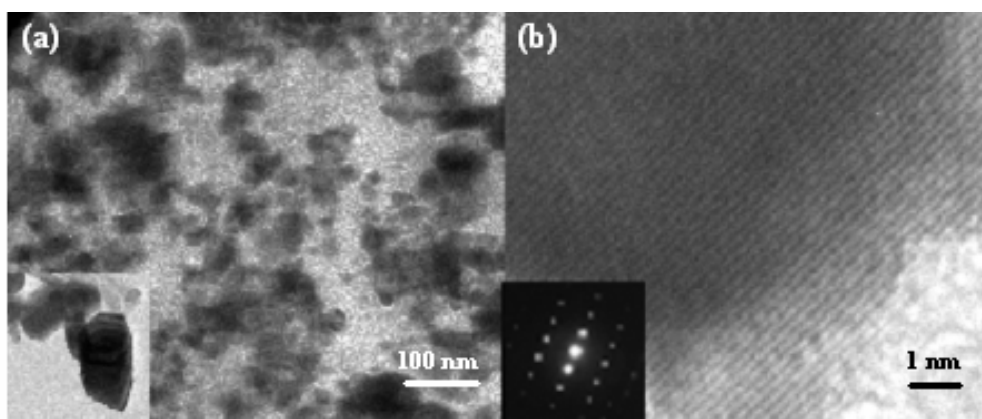


Figure 5.3 (a) Low magnification TEM image of the ZnO nanocrystals and high magnification TEM images (inset); (b) HRTEM image and the SAED pattern (inset).

Because the process at relative low temperature, ZnO nanocrystals were further prepared on a PI film. Figure 5.4 shows the FE-SEM and TEM images of ZnO nanocrystals which were deposited 10 min. From Figure 5.4a, it can be found the sizes of crystal aggregate are smaller comparing with Figure 5.2c. Besides, after dispersing by ultrasonic bath for 10 min, the TEM image shows individual and well distribution nanocrystals with size 20–30 nm. It may suggest that ZnO would harder deposit on organic PI film than quartz substrates resulting in lower adsorbability. Hence crystal aggregation is less significant. Because PI film is a flexible and thermal stable polymer film, this method can produce a mass production of ZnO nanocrystals by depositing ZnO on the roll-type of PI films.

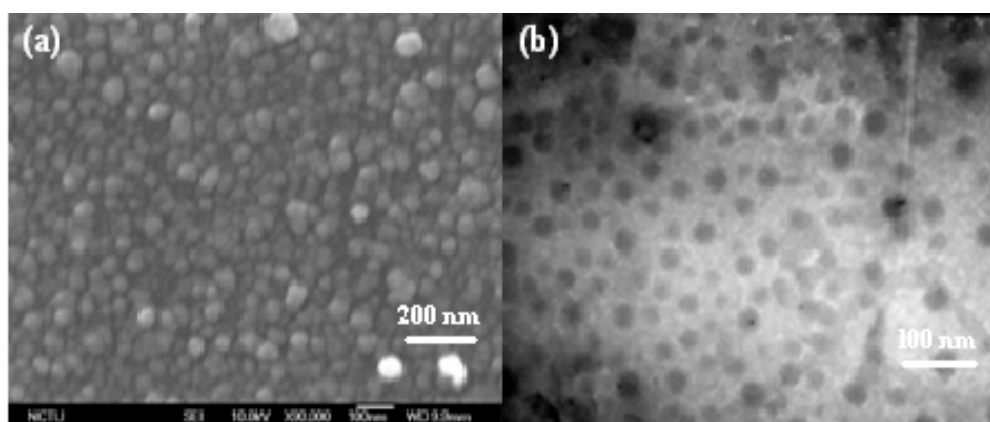


Figure 5.4 (a) FE-SEM images of the ZnO samples fabricated on PI substrates; (b) TEM image of the same sample.

Many literatures have reported that two emission band characteristics of ZnO nanostructures: the ultraviolet (UV) band emission results from near band-edge emission, while the green band emission has been attributed to the structural defects, such as oxygen vacancies<sup>[15,16]</sup>. Figure 5.5 shows the room temperature PL spectra of the ZnO nanocrystals for 10 min deposition on a quartz substrate. The produced ZnO nanocrystals exhibit strong UV emission at 395 nm, and no visible emission was detected. This indicates produced ZnO nanocrystals have negligible oxygen vacancy. On the other hand, the air-circulating can provide suitable oxidized environment to develop nearly defect-free ZnO nanocrystals.

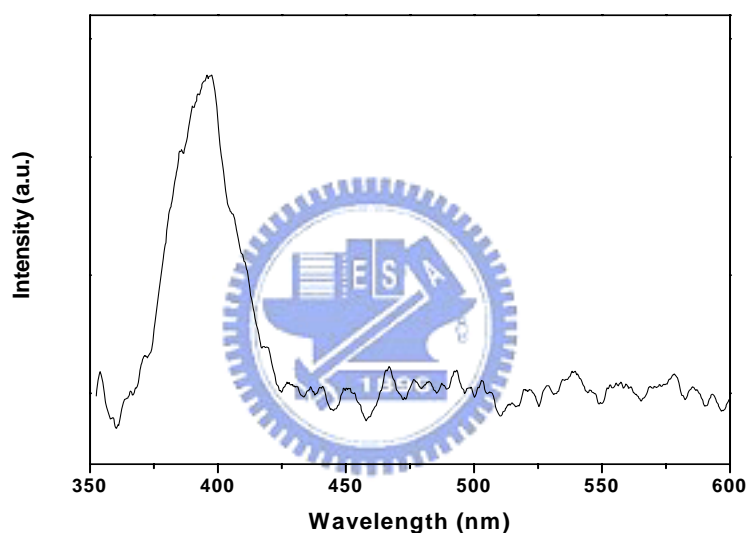


Figure 5.5 Room temperature PL spectra of the ZnO nanocrystals for deposited 10 min on quartz substrates.

## 5.4 Conclusions

ZnO nanocrystals were successfully prepared by using a thermal coater and an air-circulating. An air-circulating provides a milder and rapid oxidized environment to develop ZnO crystals, so that flexible and thermal stable PI films can also be used as substrates in this process. HRTEM and PL measurements show the produced ZnO nanocrystals are nearly defect-free single crystalline structures. Besides, deposited



ZnO on PI film substrates can obtain individual and well distribution nanocrystals after dispersing by an ultrasonic bath. Because a roll-type of PI film can be used as a substrate to deposit ZnO continually, it can be a simple and efficient method to fabricate ZnO nanocrystals on large scales.



## References

---

- [134] S. Chakrabarti, D. Ganguli, S. Chaudhuri, *J. Phys. D* 2003, **36**, 146.
- [135] S. W. Kim, S. Fujita, S. Fujita, *Appl. Phys. Lett.* 2002, **81**, 5036.
- [136] P. D. Cozzoli, M. L. Curri, A. Agostiano, G. Leo, M. Lomascolo, *J. Phys. Chem. B* 2003, **107**, 4756.
- [137] C. Panatarani, I. W. Lenggoro, K. Okuyama, *J. Nano. Res.* 2003, **5**, 47.
- [138] T. Sato, T. Tanigaki, H. Suzuki, Y. Saito, O. Kido, Y. Kimura, C. Kaito, A. Takeda, S. Kaneko, *J. Crystal Growth* 2003, **255**, 313.
- [139] Y. C. Kong, D. P. Yu, B. Zhang, W. Fang, S. Q. Feng, *Appl. Phys. Lett.* 2001, **78**, 407.
- [140] B. D. Yao, Y. F. Chan, N. Wang, *Appl. Phys. Lett.* 2002, **81**, 757.
- [141] V. A. L. roy, A. B. Djuricic, W. K. Chan, J. Gao, H. F. Lui, C. Surya, *Appl. Phys. Lett.* 2003, **83**, 141.
- [142] J. S. Lee, K. Park, M. I. Kang, I. W. Park, S. W. Kim, W. K. Cho, H. S. Han, S. Kim, *J. Crystal Growth* 2003, **254**, 423.
- [143] X. Chen, C. An, J. Liu, X. Wang, Y. Qian, *J. Crystal Growth* 2003, **253**, 357.
- [144] S. S. Xie, H. J. Yuan, et al., *Chem. Phys. Lett.* 2003, **371**, 337.
- [145] J. Park, V. Privman, E. Matijevic, *J. Phys. Chem. B* 2001, **105**, 11630.
- [146] A. P. A. Oliveira, J. F. Hochepped, F. Grillon, M. H. Berger, *Chem. Mater.* 2003, **15**, 3202.
- [147] T. W. Kim, T. Kawazoe, S. Yamazaki, J. Lim, T. Yatsui, M. Ohtsu, *Solid State Commun.* 2003, **127**, 21.
- [148] M. H. Huang, Y. Wu, H. Feick, N. Tran, E. Weber, P. Yang, *Adv. Mater.* 2001, **13**, 113.
- [149] B. Y. Geng, T. Xie, X. S. Peng, Y. Lin, X. Y. Yuan, G. W. Meng, L. D. Zhang, *Appl. Phys. A* 2003, **77**, 363.

# *Chapter 6*

## **Formation of Inverted Hexagonal Liquid Crystal in Mixtures of Amine-metal Hydroxides**



## 6.1 Introduction

One-dimensional (1D) nanostructures, such as nanorods and nanowires, are an interesting and increasingly important class of materials with diverse applications due to their anisotropic physical and photophysical properties. For instance, a nanoscale mechanical switch made from platinum and silver sulphide nanowires shows much better performance than that of regular semiconductor devices used nowadays <sup>[1]</sup>. Silicon nanowires are not toxic to cells and can promote bone growth when applying an electrical bias <sup>[2]</sup>. Bifunctional nickel/gold nanorods are potentially attractive carriers for the delivery of DNA into cells by the control of the nanorods' size and composition <sup>[3]</sup>. New negative-refraction materials were made by closely spaced pairs of parallel gold nanorods <sup>[4]</sup>. A transmission medium made from such a negative-refraction material would not reflect light and could, therefore, operate with sub-wavelength resolution. This can be used for the improvement of optical storage devices and biomedical sensors.

In recent years, many approaches have been developed for the preparation of 1D nanostructures such as vapour-phase transport <sup>[5]</sup>, arc-discharge <sup>[6]</sup>, laser ablation <sup>[7]</sup>, and wet chemical routes <sup>[8]</sup>. A promising template-based method is the use of lyotropic liquid crystals forming inverted hexagonal ( $H_{II}$ ) phases <sup>[9-13]</sup>. Generally,  $H_{II}$  phases consist of long mutually parallel aqueous cylinders surrounded by a continuous oil phase. In such systems, the reactive species are confined to the inner aqueous channels by a regular arrangement of organic molecules. This provides a nanostructured environment for the formation of 1D materials with controlled morphology.

Many reports on the preparation of  $H_{II}$  phases have been published to date. Ekwall *et al.* <sup>[14]</sup> showed the existence of  $H_{II}$  phases in ternary systems containing potassium oleate, water and decanol. Brown *et al.* <sup>[15]</sup> reported that for an Aerosol OT/xylene/water system, the  $H_{II}$  phase is formed up to fairly high water contents (up to 52 wt-%), and is in equilibrium with a lamellar phase in the direction of higher water content. Gin *et al.* synthesized a series of styrene derivatives forming  $H_{II}$  phases and further reported the effect of monomer structures as well as intermolecular interactions on the formation of the  $H_{II}$  phase <sup>[16-18]</sup>. The  $H_{II}$  phase is also found in poly oxyethylene alkyl ether/water <sup>[19, 20]</sup> and monoolein/water <sup>[21-24]</sup> systems. However, *in situ* preparation of 1D nanomaterials in  $H_{II}$  phases is still rare, the formation of ZnS, nanowires in oligo(ethylene oxide)oleyl ether/organic solvent/water mixtures <sup>[25]</sup> and the growth of PbS nanorods in AOT based ternary system <sup>[26]</sup> are just

two examples in recent years. The major reason is that they are generally formed by tiny relative amount of components and cover a small area in the phase diagram. In addition, the order of  $H_{II}$  phases is easily disrupted when doped with metallic ions.

In this chapter, the ternary system oleic acid/1-decanol/ammonium hydroxide solution, which is based on Ekwall's original  $H_{II}$  system consisting of potassium oleate/1-decanol/water <sup>[14]</sup> will be presented. Using mixtures of ammonia and oleic acid to prepare *in situ* the oleate amphiphile is more convenient and opens the possibility for the incorporation of various metal ions into the confined aqueous phase due to the formation of amine complexes.

## 6.2 Experimental section

### 6.2.1 Materials

Oleic acid (90% purity), nickel(II) chloride hexahydrate (99.9% purity), and copper(II) sulfate hydrate (98% purity) were purchased from Aldrich. Elaidic acid (97% purity) and stearic acid (98.5% purity) were obtained from Fluka. Zinc acetate dihydrate, cobalt(II) nitrate hexahydrate, 1-decanol (>99%) and silver nitrate of analytical grade were purchased from Merck. Cadmium nitrate tetrahydrate (99% purity) and 25 wt-% ammonium hydroxide of reagent grade was purchased from Riedel-de Haën. All materials were used as received without further purification. Water used in all the experiments was purified through a Pure Lab plus UV system (USF EIGA).


### 6.2.2 Preparation of $H_{II}$ phase liquid crystal

A series of samples were prepared by mixing the three compounds (oleic acid, 1-decanol, and ammonium hydroxide) at ambient temperature in the given ratio followed by subsequent centrifugation at 10000 rpm for 20 min to remove trapped air bubbles. The final samples are obtained as highly viscous, opaque gels. For metal doping, 0.1M solutions of the desired metals in 25 wt-% ammonium hydroxide were prepared and used instead of the ammonium hydroxide.

### 6.2.3 Characterization

Polarized Optical Microscopy (POM) textures were observed using a Zeiss Axioplan 2 equipped with Mettler Toledo FP82HT hot stage. The samples were first heated to the isotropic at a rate of 10 °C/min, and then cooled to 25 °C. The optical textures at different temperatures were recorded during cooling. To avoid the partial evaporation of ammonia, which would result in a change of the composition, the edges of the cover slides were sealed with silicon grease. Conductivity measurements were carried using METROHM 660 Conductometer. X-ray diffraction (XRD) patterns were measured on the BM26B beamline at the European Synchrotron Facility, E.S.R.F, Grenoble, using photons with energy of 10 keV. The data were collected in transmission using an image plate system. The samples were placed in 2 mm glass capillaries sealed with kapton foils. The modulus of the scattering vector,  $s$  ( $s = 2\sin\theta/\lambda$ , where  $\theta$  is the Bragg angle and  $\lambda$  the wavelength), was calibrated using silver behenate.

## 6.3 Results and discussion



Preliminary POM observations showed that mixtures of oleic acid/1-decanol/conc. ammonia present a fan-shaped texture characteristic of a columnar hexagonal phase in a wide compositional range. Figure 6.1 shows the phase diagram of the ternary mixture. It can be seen that the hexagonal phase is located between a fluid isotropic phase at low ammonium hydroxide content and a lamellar phase at high ammonium hydroxide concentrations.

It should be noted that compared to Ekwall's original system<sup>[15]</sup>, the columnar phase covers a surprisingly large, roughly triangular area in the phase diagram, marked by the compositions 21/55/24 (oleic acid/1-decanol/ammonium hydroxide), 28/27/45, and 62/5/33. The samples in this region are highly viscous and opaque, which becomes more pronounced with decreasing 1-decanol content. It can be safely assumed that the interplay between ammonium hydroxide and 1-decanol concentrations is responsible for the stability region of the hexagonal phase. For instance, the weakly acidic COOH moiety does not self-ionize sufficiently to act as a good hydrophilic head group and, consequently, a fluid isotropic phase is formed at low ammonium hydroxide concentration. Besides, a specific organic solvent is usually necessary in a ternary LC system to provide an appropriate environment for

the intermolecular interactions between gelator molecules and the organic solvent molecules <sup>[27]</sup>. In the present case, 1-decanol acts as the solvent as shown by the strong dependence of the sample's viscosity and the isotropic temperature ( $T_i$ ) on the 1-decanol content. The  $T_i$  increases from 56 °C at 55 wt-% to 142 °C at 5 wt-% 1-decanol. It must be noted that the system tolerates up to 45 wt-% of ammonium hydroxide before the hexagonal phase collapses. This renders the system particularly interesting as a template for the precipitation of anisotropic materials.

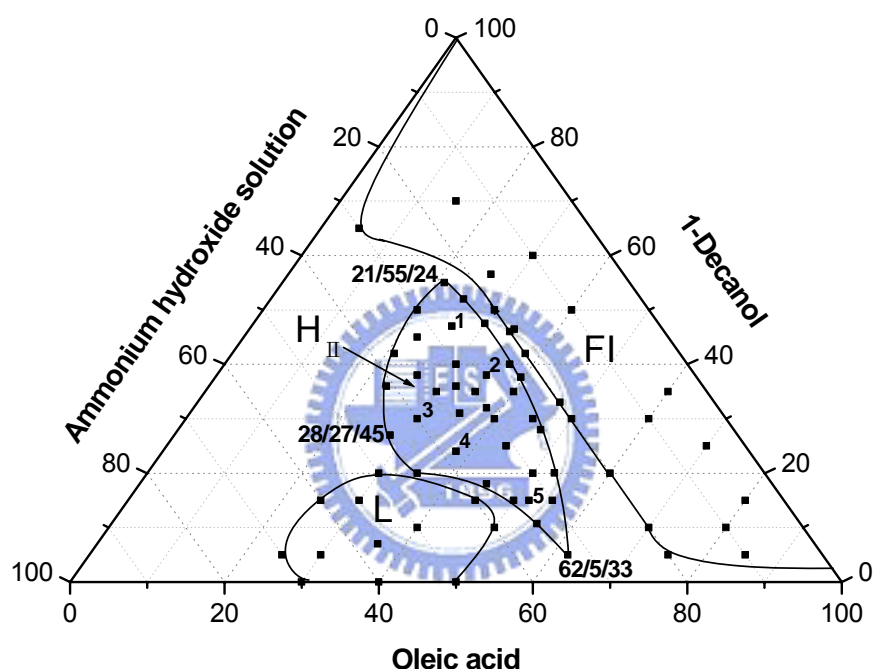


Figure 6.1 Phase diagram for the ternary mixture oleic acid/1-decanol/ ammonium hydroxide system at 25 °C. Phase notations are as follow: FI, fluid isotropy; H<sub>II</sub>, inverted hexagonal phase; and L, lamellar phase. The numbers in the region of the H<sub>II</sub> phase refer to the sample listed in Table 1.

Figure 6.2 shows typical POM textures obtained for the oleic acid/1-decanol/ ammonium hydroxide (35/38/27) sample. When cooling the mixtures from the isotropic phase, fan-shaped textures characteristic of columnar phases develop. The formation of these textures depends on the composition of the samples. Thus, at low 1-decanol contents (high  $T_i$ ), a smooth texture is obtained by simply cooling the

sample to 25 °C, while at high 1-decanol contents (low  $T_i$ ) the sample needs to be annealed for hours. Moreover, at high temperatures the development of the domains is slow and is characterized by the appearance of stripes which can be an indication of a rectangular columnar phase (Figure 6.2a) [28]. By further cooling the striations disappearance giving rise to the typical texture characteristic to columnar hexagonal mesophases [28a]. The supramolecular organization of five samples (denoted hereafter by numbers) with different composition was studied by performing X-ray diffraction experiments. The results are summarized in Table 6.1.

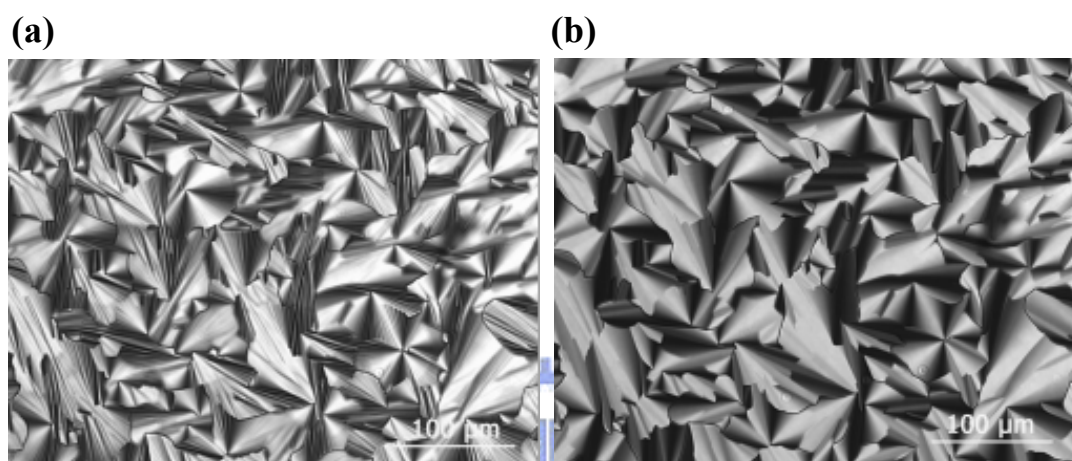


Figure 6.2 POM textures of oleic acid/1-decanol/ ammonium hydroxide (35/38/27) at (a) 70 °C and (b) 25 °C recorded during the cooling from  $T_i$  (95 °C).

Table 6.1 Phase behaviour of the ternary mixtures

No	Composition (wt %) oleic acid/1-decanol/ammonium hydroxide	$T_i^a$ °C	hkl	$d_{hkl}$ , Å		ICD <sup>b</sup> , Å	$R_w^c$ , Å	$L^d$ , Å
				$d_{hkl}^{exp}$ , Å	$d_{hkl}^{calc}$ , Å			
1	25/48/27	78	100	34.39	34.39	39.7	10.8	9.0
			110	19.73	19.85			
			200	17.11	17.19			
2	35/38/27	95	100	35.0	35.0	40.4	11.0	9.2
			110	20.33	20.2			
			200	17.60	17.5			
3	30/30/40	106	100	36.73	36.73	42.4	14.1	7.1
			110	21.28	20.20			
			200	18.58	18.36			
4	37/25/38	120	100	37.37	37.37	43.2	14.0	7.6
			110	21.58	21.27			
			200	18.65	18.68			
5	52/15/33	128	100	38.27	38.27	44.2	13.3	8.8
			110	22.06	22.09			
			200	19.01	19.13			

<sup>a</sup> isotropic temperature, <sup>b</sup> a-lattice parameter of the  $H_{II}$  phase, <sup>c</sup> water channel radius;

<sup>d</sup> hydrophobic tail length



Figure 6.3A shows the diffraction of sample 5 recorded at 25 °C. The diffraction pattern shows a set of reflections with  $s$ -spacings given by the ratio: 1:  $\sqrt{3}$ : 2. These can be indexed to 100, 110 and 200 reflections of a hexagonal columnar mesophase<sup>[16]</sup>. In the wide-angle diffraction region of the same pattern a broad halo is found at 4.3 Å, which can be assigned to fluid hydrocarbon chains<sup>[29]</sup>. The diffraction pattern recorded at 55 °C shows different features (Figure 6.3B). The two reflections (34.6 and 31.5Å) in the small-angle region (see inset) could be indexed to a rectangular columnar phase; however this indexing cannot be established on the basis of these two peaks alone.

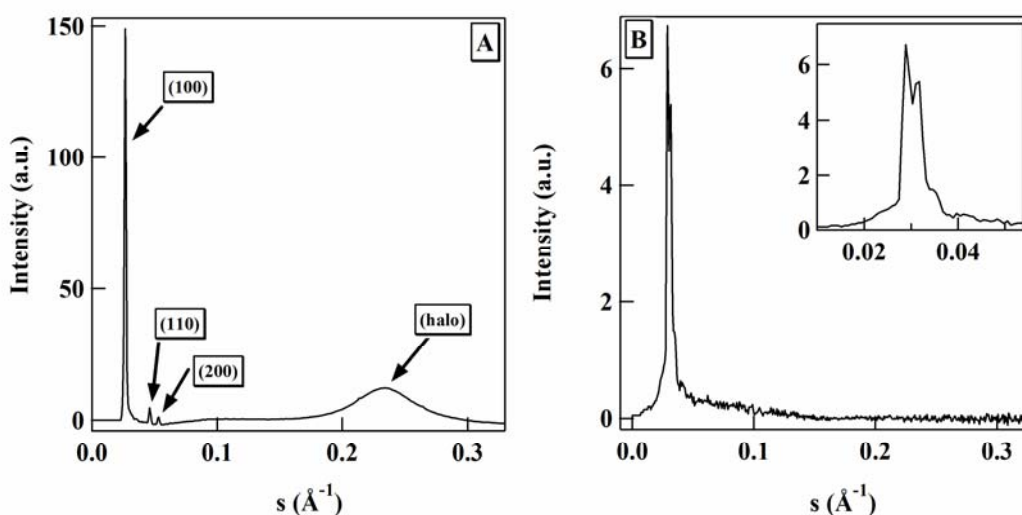


Figure 6.3 X-ray diffraction patterns of oleic acid/1-decanol/ ammonium hydroxide solution (52/15/33) at (a) 25 °C and (b) 55 °C: The inset gives a closer view of the low-angle part of the curve showing the splitting of the first diffraction peak.

The question now arises as to whether the observed columnar phases are of the normal ( $H_I$ ) or of the inverted ( $H_{II}$ ) type. The  $H_{II}$  phase is characterized by a continuous oil phase surrounding water columns with the hydrocarbon chains of the amphiphiles facing outwards. A differentiation of the two phases should, therefore, be possible through conductivity measurements. A normal  $H_I$  sample was prepared from oleic acid/hexanol/water (49/2/29)<sup>[15]</sup> and showed a conductivity of 1.18 mS/cm. In comparison, the liquid crystalline samples in this study show a significantly lower conductivity in the range of several  $\mu$ S/cm. Another test to identify the outer phase is the miscibility. For that, a small amount of water or hexane was added to a sample.

While hexane was easily absorbed by the sample, the water droplet persists even under violent shaking. All these results confirm the formation of an  $H_{II}$  phase in the system oleic acid/1-decanol/ ammonium hydroxide.

Figure 6.4 shows a schematic representation of the proposed LC structure. The kink in the middle of the alkyl chain of oleic acid contributes to the volume factor and results in larger critical packing parameter, which favours the formation of inverted structures <sup>[27]</sup>. However, replacing oleic acid by stearic acid or elaidic acid also resulted in the formation of gel-like samples that show fan-shaped textures, a comparable phase behaviour, and similar miscibility with water and hexane. As expected, the  $T_i$  of these three systems follows the trend of the melting points of the pure acids. For example, in the composition 30/40/30 (acid/1-decanol/ammonium hydroxide), the  $T_i$  for the system containing stearic acid (mp 62–71 °C) is 100 °C, for elaidic acid (mp 42–44 °C) 91 °C, and for oleic acid (13–14 °C) 85 °C.

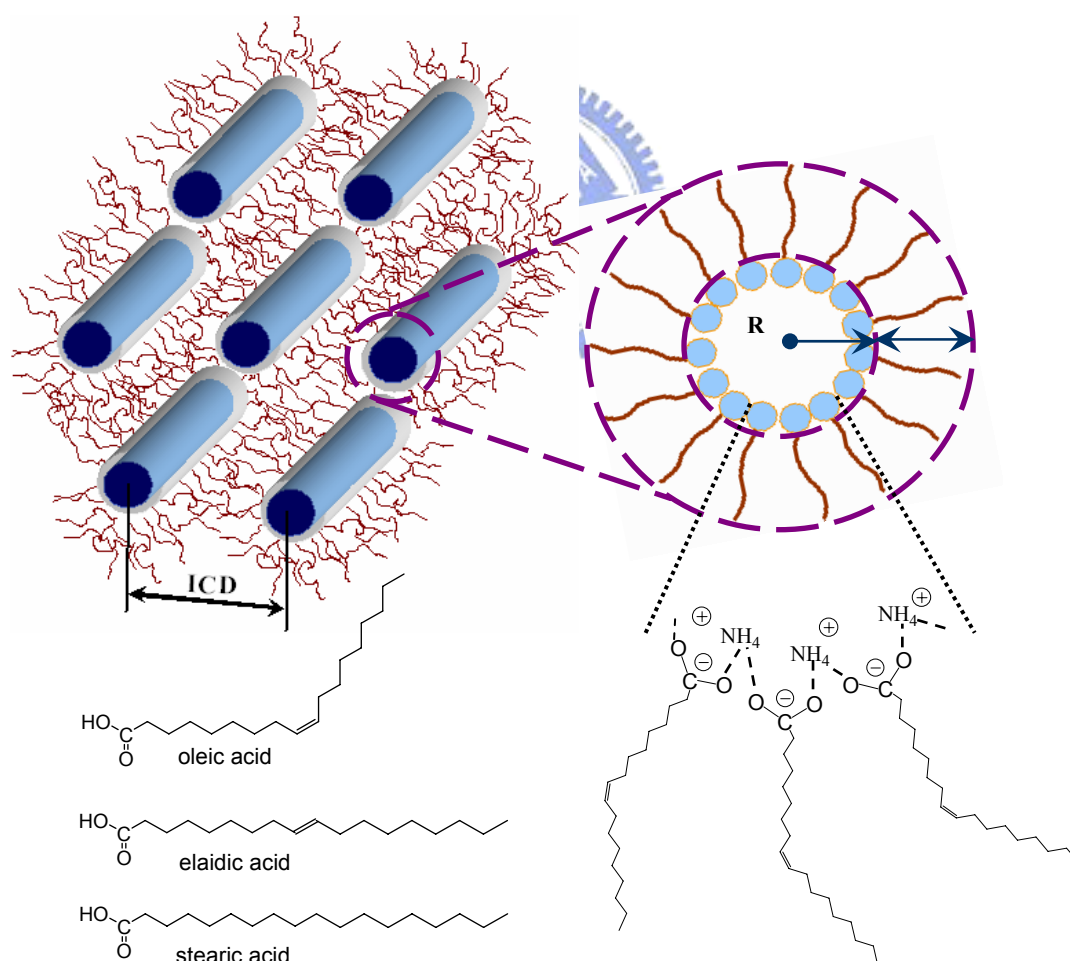


Figure 6.4 Schematic representation of a three-dimensional network of the inverted hexagonal phase. The notations are as follows: ICD, interchannel distance;  $R_w$ , water channel radius and  $L$ , hydrophobic tail length.

The hexagonal lattice parameter,  $a$  or interchannel distance (ICD), the water channel radius ( $R_w$ ) and the hydrophobic tail length ( $L$ ) (c.f. Figure 6.4) were calculated from the XRD data based on the following equations<sup>[16, 30]</sup>:

$$ICD = \frac{d_{100}}{\cos 30^\circ}$$

$$R_w^2 = \frac{\sqrt{3}ICD^2 \phi_A}{2\pi}$$

$$L = \frac{ICD}{2} - R_w$$

where  $\phi_A$  is the fractional volume of the ammonium hydroxide solution,  $V_A / (V_O + V_D + V_A)$ , where the indices A refer to ammonium hydroxide, O to oleic acid, and, D to 1-decanol. In accordance with literature<sup>[30]</sup>, the fractional volume is replaced by the fractional weight,  $W_A / (W_O + W_D + W_A)$ , due to the similar densities (oleic acid: 0.89 g/ml, 1-decanol: 0.83 g/ml, and ammonium hydroxide: 0.91 g/ml). The  $R_w$  and  $L$  are roughly proportional to the contents of ammonium hydroxide solution and oleic acid, respectively. In addition, the calculated ICD values which range from 39.7 to 44.2 Å consistent with the reported ICD values of  $H_{II}$  phase<sup>[16]</sup>.

Sample 3 was used to test possible metal doping. For this, 10 mM solutions of  $Ag^+$ ,  $Cu^{2+}$ ,  $Ni^{2+}$ ,  $Co^{2+}$ ,  $Zn^{2+}$ , and  $Cd^{2+}$  in conc. ammonia were used instead of the plain ammonia. In all cases, the presence of the fan-shaped textures and the similar  $T_i$  confirms that the ion doping does not disrupt the order of the  $H_{II}$  phase. Even at concentrations of 50 and 100 mM, highly viscous, opaque gel and the fan-shaped textures are observed. However, the  $T_i$  dropped from 102 °C at 10 mM  $Ag^+$  to 73 °C at 50 mM  $Ag^+$ . The phase diagrams have been reproduced for at 10 mM metal concentration and similar results as compared to the metal free systems were obtained. This confirms that the  $H_{II}$  phase prepared by oleic acid/1-decanol/ammonium hydroxide ternary system has a wide region of stability with respect to the ion doping.

## 6.4 Conclusions

The ternary system oleic acid/1-decanol/ammonium hydroxide exhibits an inverse hexagonal ( $H_{II}$ ) liquid crystalline phase, which is predominate at room temperature and exists in a wide compositional range. Polarized optical microscopy and x-ray diffraction confirms the formation of the hexagonal phase, while conductivity measurements reveal the inverse nature. The system can tolerate up to 45 wt-% of ammonium hydroxide before the hexagonal phase collapses. Using mixtures of ammonia and oleic acid to prepare *in situ* the oleate amphiphile is more convenient than using authentic alkali oleates. In particular, this allows for the incorporation of up to 100 mM solutions of metal ions such as  $Ag^+$ ,  $Cu^{2+}$ ,  $Ni^{2+}$ ,  $Co^{2+}$ ,  $Zn^{2+}$ , and  $Cd^{2+}$  into the confined aqueous phase due to the formation of ammine complexes. We expect that this inverse hexagonal system will serve as versatile tool for the preparation of nanorods and nanowires.



## References

---

- [150] K. Terabe, T. Hasegawa, T. Nakayama, M. Aono, *Nature* 2005, **433**, 47.
- [151] D. K. Nagesha, M. A. Whitehead, J. L. Coffey, *Adv. Mater.* 2005, **17**, 921.
- [152] A. Salem, P. C. Searson, K. W. Leong, *Nature Mater.* 2003, **2**, 668.
- [153] V. M. Shalaev, W. S. Cai, U. K. Chettiar, H. K. Yuan, A. K. Sarychev, *Opt. Lett.* 2005, **30**, 3356.
- [154] S. Cjattopadhyay, S. C. Shi, Z. H. Lan, C. F. Chen, K. H. Chen, *J. Am. Chem. Soc.* 2005, **127**, 2810.
- [155] Y. Zhou, S. H. Yu, X. P. Cui, C. Y. Wang, Z. Y. Chen, *Chem. Mater.* 1999, **11**, 545.
- [156] A. M. Morales, C. M. Lieber, *Science* 1998, **279**, 208.
- [157] C. J. Murphy, N. R. Jana, *Adv. Mater.* 2002, **14**, 80.
- [158] S. I. Stupp, P. V. Braun, P. Osenar, *Science* 1996, **380**, 325.
- [159] S. I. Stupp, P. V. Braun, P. Osenar, V. Tohver, S. B. Kennedy, *J. Am. Chem. Soc.* 1999, **121**, 7302.
- [160] P. V. Braun, P. Osenar, S. I. Stupp, *Nature* 1996, **380**, 325.
- [161] X. Jiang, Y. Xie, J. Lu, L. Zhu, W. He, Y. Qian, *J. Mater. Chem.* 2001, **11**, 1775.
- [162] J. Ma, D. Zhang, L. Qi, H. Cheng, *J. Colloids Interface Sci.* 2002, **264**, 413.
- [163] P. Ekwall, L. Mandell, K. Fontell, *Acta. Chem. Scand.* 1968, **22**, 373.
- [164] G. H. Brown, *Proc. Int. Liq. Cryst. Conf. Part 1* 1968, 346.
- [165] D. H. Gary, D. L. Gin, *Chem. Mater.* 1998, **10**, 1827.
- [166] M. A. Reppy, D. H. Gary, B. A. Pindzola, J. L. Smithers, D. L. Gin, *J. Am. Chem. Soc.* 2001, **123**, 363.
- [167] D. L. Gin, W. Gu, B. A. Pinzola, W. J. Zhou, *Acc. Chem. Res.* 2001, **34**, 973.
- [168] H. Kunieda, Y. Yamaguchi, K. Ozawa, M. Suzuki, *Colloids Surf. A.* 1999, **160**, 15.
- [169] H. Kunieda, K. Shigeta, K. Ozawa, M. Suzuki, *J. Phys. Chem. B* 1997, **101**, 7952.
- [170] H. Qiu, M. Caffrey, *J. Phys. Chem. B* 1998, **102**, 4819.
- [171] S. Mele, S. Murgia, M. Monduzzi, *Colloids Surf. A* 2003, **228**, 57.
- [172] J. Barauskas, V. Razumas, Z. Talaikytė, A. Bulovas, T. Nylander, *Chem. Phys. Lipids* 2003, **123**, 87.
- [173] J. Borné, T. Nylander, A. Khan, *Langmuir* 2001, **17**, 7742.
- [174] X. Jiang, Y. Xie, J. Lu, L. Zhu, W. He, Y. Qian, *Chem. Mater.* 2001, **13**, 1213.
- [175] N. M. Huang, R. Shahidan, P. S. Khiew, L. Peter, C. S. Kan, *Colloids Surf. A*

- 2004, **247**, 55.
- [176] R. Kumar, O. P. Katare, *AAPS PharmSciTech* 2005, **6**, E298.
- [177] a) P. G Schouten, J. F. Van der Pol, J. W. Zwikker, W. Drenth, S. J. Picken, *Mol. Cryst. Liq. Cryst.* 1991, **195**, 291. b) L. Mamlok, J. Malthete, N. H. Tinh, C. Destrade, A. M. Levelut, *J. Phys. Lett.* 1982, **43**, 641. c) R. I. Gearba, A. Bondar, B. Goderis, W. Bras, D. A. Ivanov, *Chem. Mater.* 2005, **17**, 2825.
- [178] W. Srisiri, T. M. Sisson, D. F. O'Brien, K. M. McGrath, Y. Q. Han, S. M. Gruner, *J. Am. Chem. Soc.* 1997, **119**, 4866.
- [179] H. Qiu, M. Caffrey, *Chem. Phys. Lipids* 1999, **100**, 55.



# *Chapter 7*

## **Preparation of Silver Nanocables from Self-assembling Tubular Silver ion Precursors**



## 7.1 Introduction

The nanowires with sheaths, named nanocables, are a new kind of practical one-dimension nanostructure. Their functions can be further improved through a rational design of wire and sheath from different materials. For example, chemically inert materials, such as silica around metallic or semiconductor nanowires can provide an electric insulation and prevent surface oxidation<sup>[4-6]</sup>. Polymer sheaths, like poly(vinyl acetate) (PVAc)<sup>[7]</sup> and poly(vinyl alcohol)<sup>[8]</sup> have been used to increase the dispersability of metal or semiconductor cores in organic solvents. In addition, a fully organic system, polypyrrole wrapped around poly(methyl methacrylate) (PMMA), has also been reported<sup>[9]</sup>. The PMMA not only acts as an insulator, but also increases the mechanical properties of the conducting polymer composite and makes it easier to process.

Recently, different methods such as laser ablation combined with thermal evaporation<sup>[1-4]</sup>, sol-gel reactions<sup>[12]</sup>, templating<sup>[6,7,9-13]</sup>, hydrothermal conversion<sup>[8,14]</sup>, and capillary force<sup>[15,16]</sup> have been employed for the preparation of nanocables. Using structure-directing templates is a highly efficient method, since the cable structure is readily formed. For example, Ni/Cu<sup>[11]</sup>, Co/Ge<sup>[12]</sup> and Ni/V<sub>2</sub>O<sub>5</sub><sup>[13]</sup> nanocables have been prepared in the pores of commercial membranes by electrochemical deposition. Likewise, Ag nanocables were prepared by thermal decomposition of AgNO<sub>3</sub> absorbed in mesoporous silica<sup>[6]</sup>. When using self-assembling templates, the desired core-shell structure becomes thermodynamically favorable and forms by itself. This way, CdSe/PVAc nanocables have been made under  $\gamma$ -irradiation<sup>[7]</sup>.

This chapter will describe a simple yet versatile wet chemical approach for the one pot preparation of Ag nanocables using the self-assembly of *in situ* prepared diamminesilver-(I) oleate.

## 7.2 Experimental section

### 7.2.1 Materials

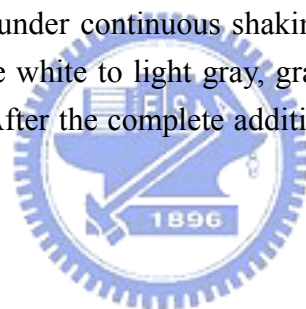
Oleic acid (90% purity) was purchased from Aldrich. Analytical grade formaldehyde solution (37 wt.-% in water) and silver nitrate were obtained from Merck. Reagent grade ammonium hydroxide solution (25 wt.-% in water) was



purchased from Riedel-de Haën. Reagent grade ethanol and potassium hydroxide were purchased from KMF (Siegburg, Germany). All materials were used as received without further purification. Water was purified through a Pure Lab plus UV system (USF EIGA). All the reactions in this study were carried out at ambient conditions.

## 7.2.2 Preparation of silver nanocables

In a typical procedure, the diamminesilver(I) complex (**1**), namely Tollen's reagent, was prepared by the dropwise addition of ammonium hydroxide solution into 1.8g of a 0.1M aqueous  $\text{AgNO}_3$  solution until the brown precipitate disappears. The thus prepared complex was thoroughly mixed with oleic acid and stirred for 1 hour to obtain a defined molar ratio of oleic acid to  $\text{Ag}^+$ . This led to the formation white, viscous gels of diamminesilver(I) oleate (**2**). For the reduction of the silver ions, 0.1g of the complex **2** were dispersed in 5g of ethanol to form an opalescent suspension. Then, two drops of formaldehyde were added, followed by the slow and dropwise addition of 0.1 ml 1M KOH under continuous shaking at 300 rpm. The color of the suspension changed from pale white to light gray, gray and finally to dark gray with increasing volume of KOH. After the complete addition of KOH, the suspension was kept shaking for 1 hour.



## 7.2.3 Characterization

The structure of diamminesilver(I) oleate (**2**) was identified by Fourier transform infrared (FTIR) spectroscopy using a Nicolet Thermo Nexus. The samples for FTIR measurements were washed by water and ethanol, and then dried under vacuum at room temperature for 8h, after which the samples had the appearance of wax-like solids. The optical microscopy textures were obtained using a Zeiss Axioplan 2 with calibrated image processing software. The products were visualized at room temperature between a glass slide and cover slip. Bright-field transmission electron microscopy (TEM) images were recorded using a Philip CM 10 transmission electron microscope. The Dark-filed TEM image and the elemental profile across a nanocable were obtained by FEI TECNAI F20. The samples before reduction were prepared by dispersing the viscous white gels in ethanol. The samples after reduction were first centrifuged at 4000 rpm for 10 min, and then redispersed in ethanol. Carbon-coated copper grids were used as support.

### 7.3 Results and discussion

The molar ratio of oleic acid/ $\text{Ag}^+$  shows a great influence on the product morphology. Below 30, the product agglomerates irreversibly and precipitates in water. Above 30, a homogenous, viscous white gel is obtained. Figure 7.1 shows images of the dark-field optical microscopy for the diamminesilver-(I) oleate gel at a molar ratio of 30. At low magnification, the gel seems to consist of spherical vesicles (Figure 7.1a). Higher magnifications (Figure 7.1b) reveal that these vesicles are composed of nanometer-sized strings, which bundle up to form thicker aggregates. When this gel is dispersed in ethanol, the agglomerated bundles will separate to individual filaments (Figure 7.1c). In contrast to other objects composed of oleic acid moieties, these filaments are hard and break under the microscope when stressed. This will be covered further on.

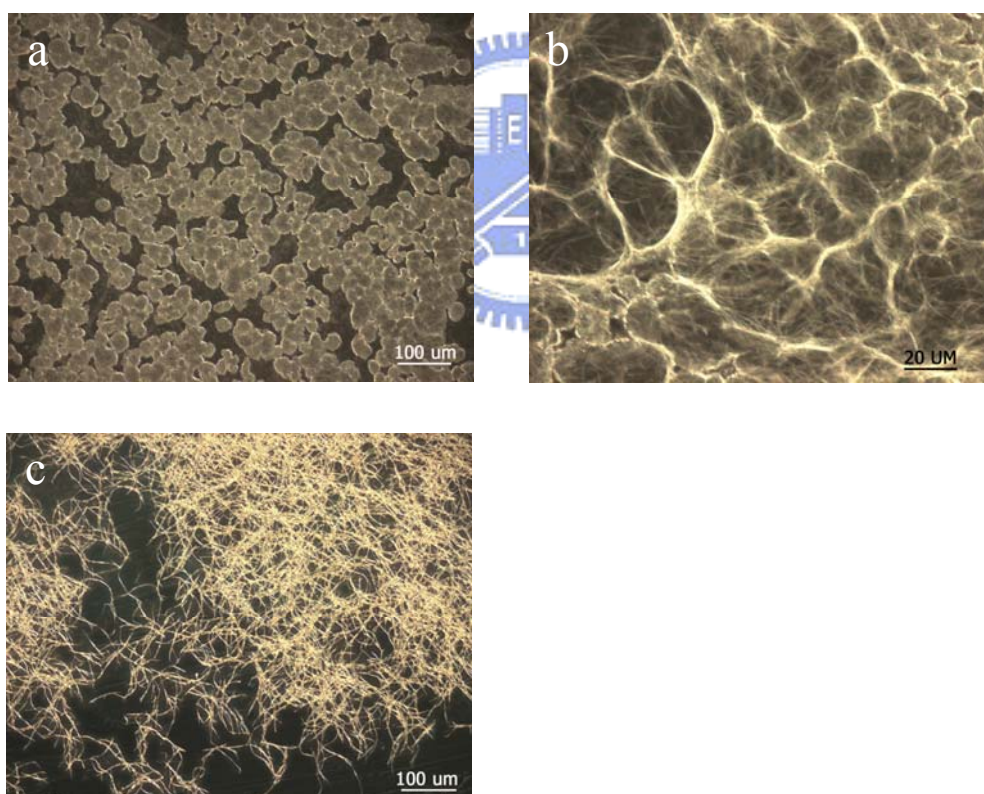


Figure 7.1 Images of the dark-field optical microscopy for a diamminesilver-(I) oleate gel at a molar ratio of 30 before (a, b) and after (c) dispersion in ethanol.

Figure 7.2 shows unstained micrographs of the oleic acid/Ag<sup>+</sup> mixtures. At a molar ratio of 30 (oleic acid/Ag<sup>+</sup>), large bundles of nanowires are formed (Figure 6.2a). These bundles are composed of solid nanowires and hollow nanotubes as observed in high resolution TEM (data not shown). The length ranges from 5–8 μm and the diameters from 280–500 nm. When the molar ratio of oleic acid/Ag<sup>+</sup> reaches 50, long nanowires with high aspect ratios are obtained (Figure 7.2b). High resolution TEM reveals that these nanowires possess hollow cavities (Figure 7.2c and 7.2d). The lengths of these nanotubes are in the order of several ten microns, with outer diameters of 155–200 nm, i.e. an aspect ratio of ca. 250. The wall thickness is 60–70 nm.

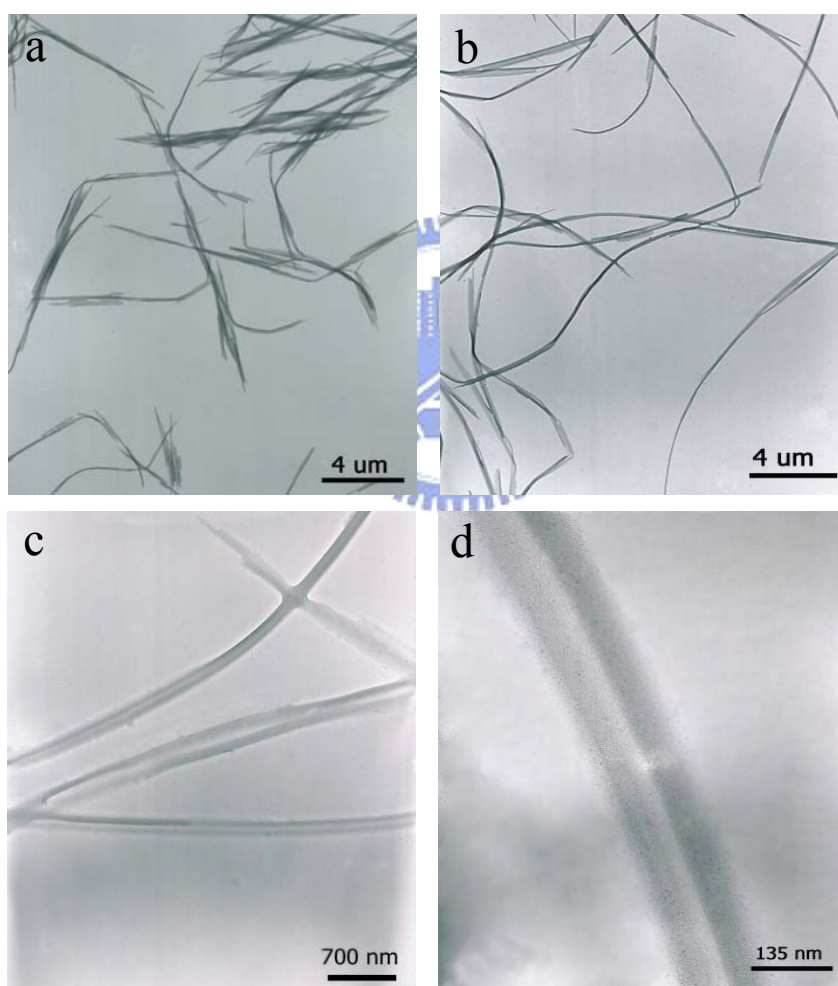


Figure 7.2 TEM micrographs (unstained) of a diamminesilver(I) oleate gel at a molar ratio oleic acid/Ag<sup>+</sup> of 30 (a) and 50 (b-d).

To form nanowires, the nanotube dispersions were treated with formaldehyde. As expected, the reaction conditions had a great influence on the morphology of the reduction products (Figure 7.3). Apart from an oleic acid/ $\text{Ag}^+$  ratio of larger than 30, gradual addition of the reagents under gentle agitation is required to obtain well-defined nanocables. The diameters of these cables match the ones found for the hollow tubes observed before reduction. In the TEM micrograph, a sharp contrast between sheath and core can be clearly observed. The cores are straight and uniform with diameter of 30–45 nm throughout their entire length. The silver profile across a nanocable (Figure 7.3d bottom) further confirms the presence of a solid, inner silver core, while there are some silver particles distributed on the outer sheath. However, the sheath does not seem to be entirely depleted of silver. It remains unclear, whether this is unreacted  $\text{Ag}^+$ -oleate or small silver agglomerations.

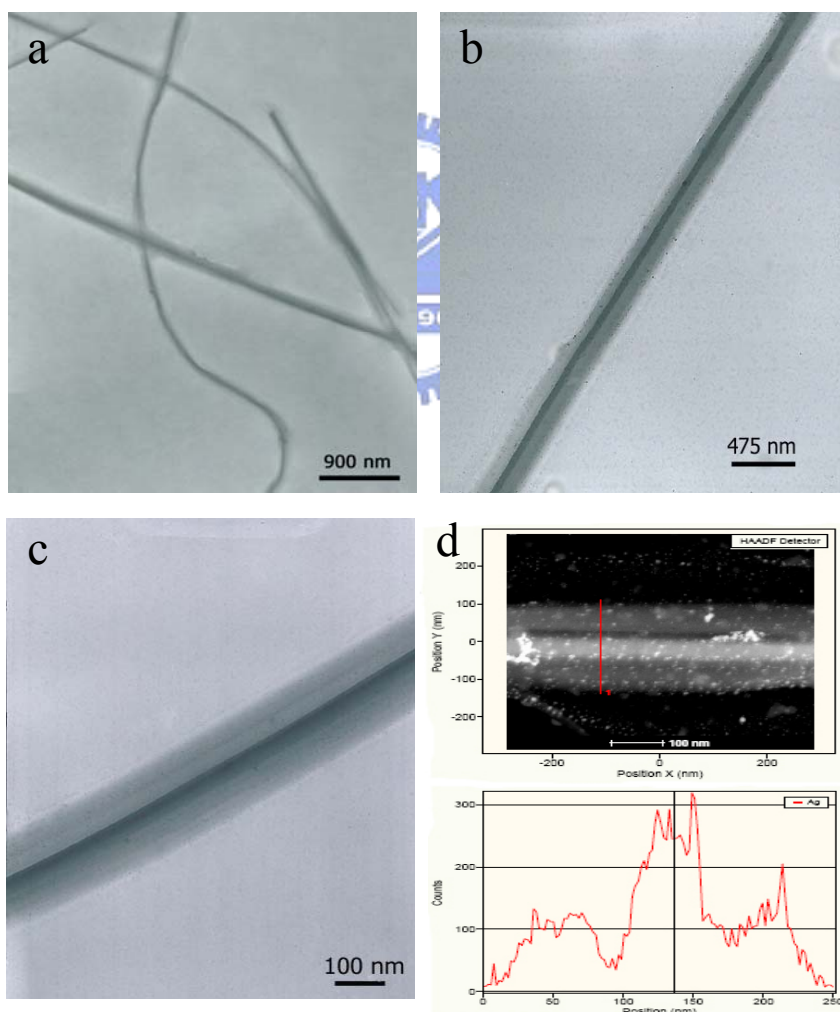


Figure 7.3 Bright-field TEM micrographs of nanocables after reduction of a gel with a molar ratio oleic acid/ $\text{Ag}^+$  of 50 (a-c) and a dark-field TEM micrographs (d, top) and the corresponding silver profile across the nanocable (d, bottom).

In contrast, if all the reagents are added at one time under violent stirring, a different morphology is found (Figure 7.4). The product now consists of short rods of 200 nm length (aspect ratio  $\sim 5$ ) and even spherical particles of 10–70 nm in diameter. Clearly, adding all reducing agent at once induces fast nucleation, which results in the formation of spherical particles.<sup>[17]</sup> It is important to note that the spheres are not randomly distributed, but lined up in string-like aggregates (Figure 7.4b), which bear close resemblance to the original tubular structure (Figure 7.4b). Higher magnifications (Figure 7.4c) reveal that the rod-like objects are also composed of small spherical nanoparticles of approximately 10 nm diameter arranged linearly in a tubular structure.

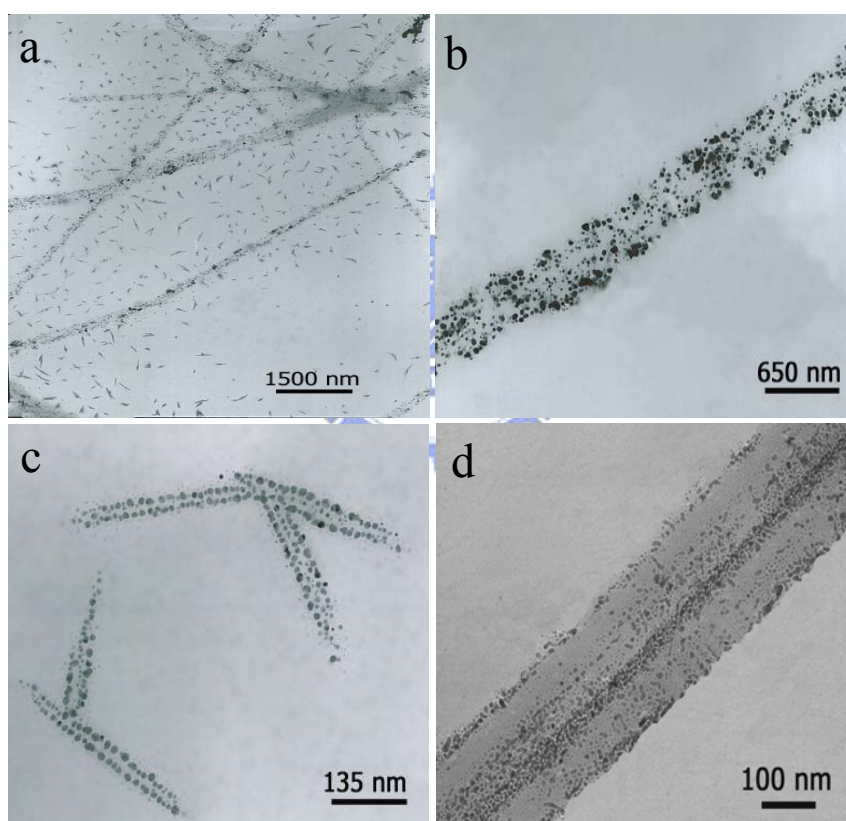


Figure 7.4 TEM micrographs of the reduction products made by fast addition of KOH (a-c) and substituting  $\text{NaBH}_4$  for formaldehyde (d).

Similar results are obtained when formaldehyde is replaced by  $\text{NaBH}_4$ . Instead of fully developed cables, again particles are found all over the tube (Figure 7.4d). At close examination, several features become evident: (i) most particles are located in

the core of the cable, (ii) the outer surface is densely covered with particles, and (iii) between core and surface, the particles are arranged in stripes parallel to the core. This situation is also seen when formaldehyde is used in low quantities, and appears to be an intermediate state on the way towards the formation of fully the developed cables. The question now arises as to how the tubes and cables are formed.

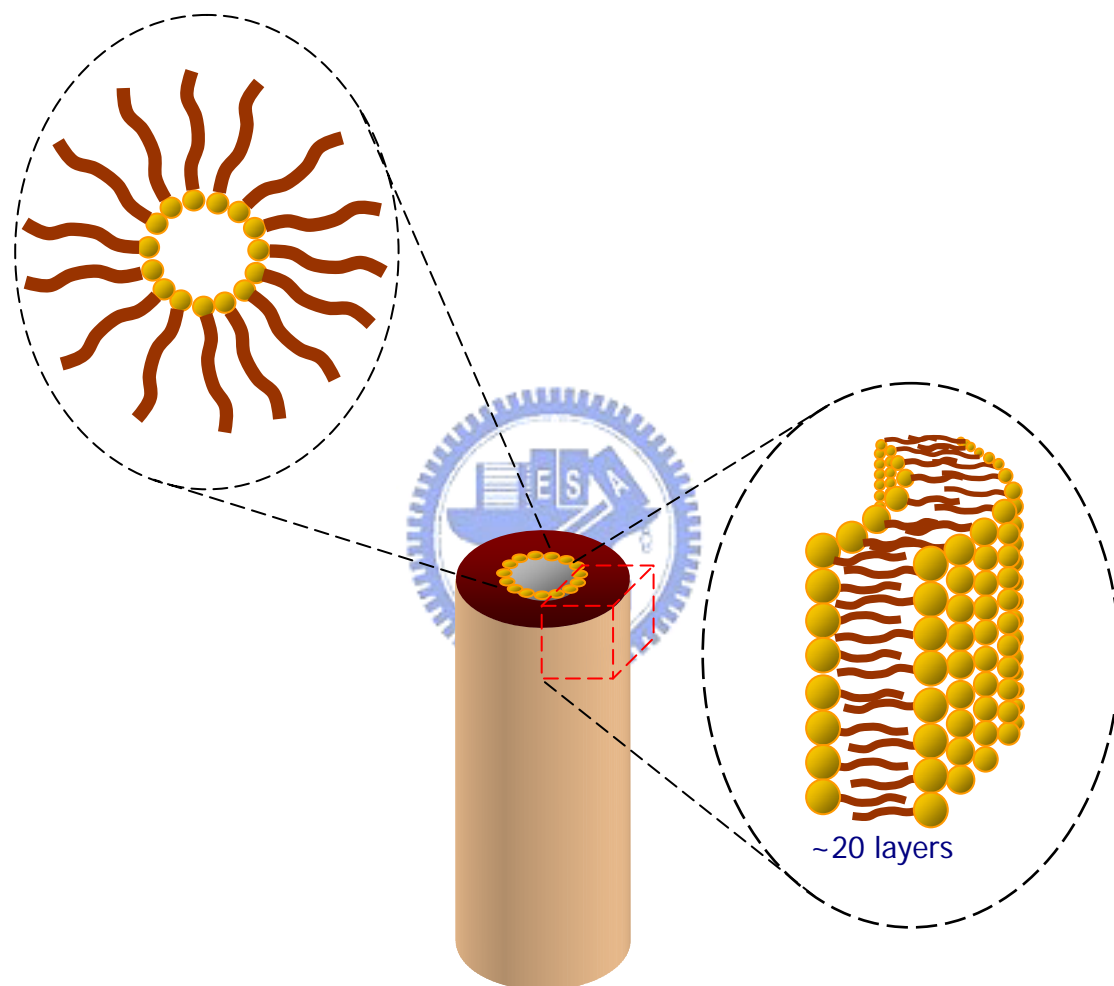


Figure 7.5 Schematic structure of the oleic acid/Ag<sup>+</sup> nanotube.

It has been reported that metal salts of long chain fatty acids form bilayer aggregates<sup>[18]</sup> and can assemble to inverted cylindrical structures<sup>[19]</sup>. The XRD pattern of the nanotube suspensions shows one sharp reflection (100) at 3.18 nm. An individual metal oleate is approximate 2 nm long<sup>[20]</sup>, which suggests the presence of interdigitated bilayers<sup>[21]</sup>. With an observed wall thickness of 60–70nm, the sheath in the presented cables seems to be composed of approximately 20 layers. The layer theory is supported by the formation of particles in a string-like alignment in the sheath. Theoretically, a tubular superstructure composed of a bundle of smaller tubes could also account for the observed string-like arrangement of particles, but such a structure was not seen in high resolution TEM. Furthermore, the inner core diameter seems to be the smallest arrangement of diamminesilver(I) oleate with a dense enough packing of the alkyl chains to form bilayers. The hollow core before reduction (Figure 7.2d) as well as the silver wire (Figure 7.3c) are, on the other hand, prominent features in the TEM micrographs, and a multi bundle structure should, therefore, be clearly noticeable. Base on these considerations we assume the tubes to have a multi lamellar wall structure as depicted in Figure 7.5.

Upon addition of the reducing agent, the silver ions are reduced to metallic silver. As seen in Figure 7.4d, this nucleation might take place all over the tube. Slow addition of the reducing agent allows Ostwald ripening to come in to play and provides the mechanism for silver ions to be transported to the centre. As seen in Figure 7.4d, the particle density in the core is higher than anywhere else. This allows for the formation of large particles by agglomeration of smaller ones early in the process. These then grow at the expense of the remaining small particles in the structure. No particles outside the template were found in any of the experiments under the described conditions.

To gain more insight into the structure of the tubes, the FTIR spectra of the nanotubes were compared with oleic acid and the final nanocable (Figure 7.6). The characteristic vibration of oleic acid is a broad OH stretch at  $\sim 3000\text{ cm}^{-1}$  and a sharp C=O stretch at  $1710\text{ cm}^{-1}$ . These signals were not found in the spectra of the nanotubes. For the nanotube, the new strong signals at 1563, 1467 and  $1419\text{ cm}^{-1}$  could be assigned to the asymmetric ( $1563\text{ cm}^{-1}$ ) and the symmetric ( $1467$  and  $1419\text{ cm}^{-1}$ ) stretching vibration of the ionized carboxylate group<sup>[20]</sup>. The characteristic signals of NH bending and stretching were also found at  $1517$  and  $3410\text{ cm}^{-1}$ , respectively.

The asymmetric and symmetric carboxylate vibrations can be used to determine

the type of coordination by calculating the difference  $\Delta = \nu_{\text{as}}(\text{COO}) - \nu_{\text{s}}(\text{COO})$ . The  $\Delta$  values indicate the four main coordination types: ionic ( $\Delta = 164 \text{ cm}^{-1}$ ), monodentate ( $\Delta = 200\text{--}300 \text{ cm}^{-1}$ ), chelating bidentate ( $\Delta = 40\text{--}110 \text{ cm}^{-1}$ ) and bridging bidentate ( $\Delta = 140\text{--}170 \text{ cm}^{-1}$ ) [21]. In the present nanotubes, there are two symmetric stretching vibration, thus two  $\Delta$  values of  $\Delta_1 = 96$  and  $\Delta_2 = 144 \text{ cm}^{-1}$  are obtained. The first one can be assigned to a chelating bidentate type, while the second one indicates a bridging bidentate (Figure 7.7). These results further corroborate the formation of diamminesilver-(I) oleate. After reduction to nanocables, a slight change in the FTIR spectrum is observed as compared to the nanotubes. A new signal at  $1577 \text{ cm}^{-1}$  appeared, while the signal at  $1419 \text{ cm}^{-1}$  shifted to  $1407 \text{ cm}^{-1}$ , and the signal at  $3410 \text{ cm}^{-1}$  shifted to  $3439 \text{ cm}^{-1}$  and became stronger. In addition, a new peak at  $1635 \text{ cm}^{-1}$  was found, which might be assigned to C=O vibration of an amide group. It can, therefore, be safely assumed that the sheath consists of oleate molecules, which are partially crosslinked by silver atoms. This would explain the stiffness observed in the optical microscope.

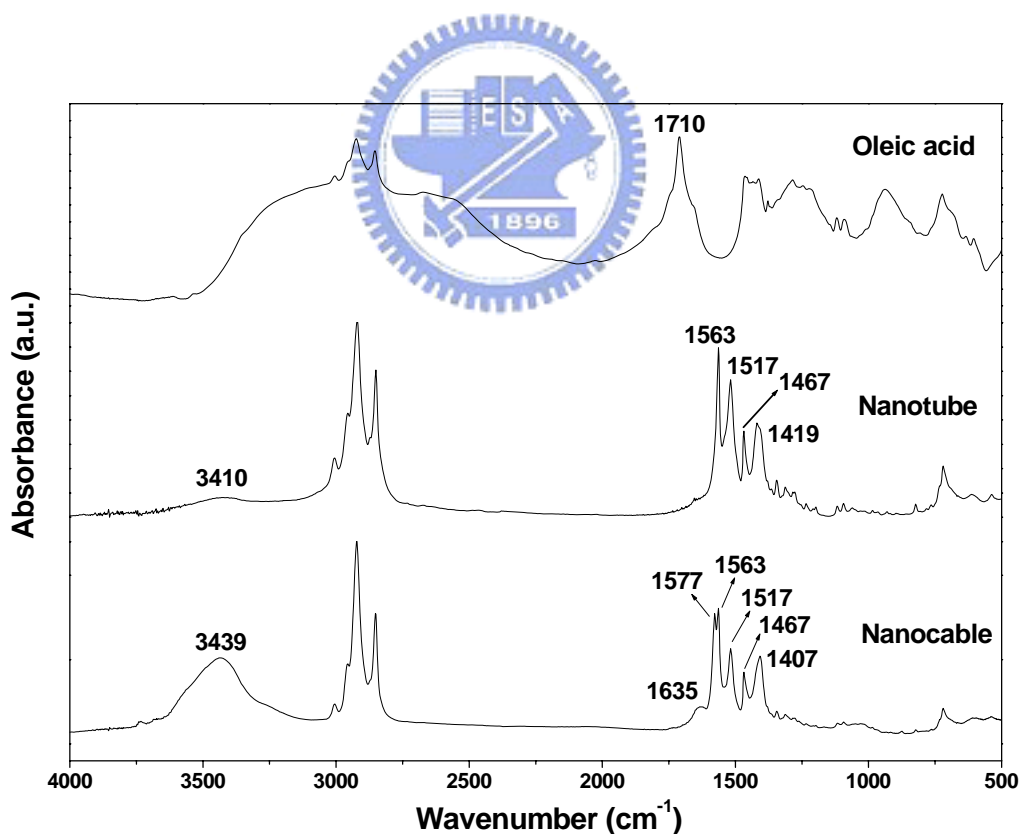


Figure 7.6 FT-IR spectra of oleic acid, the nanotubes, and silver nanocables.



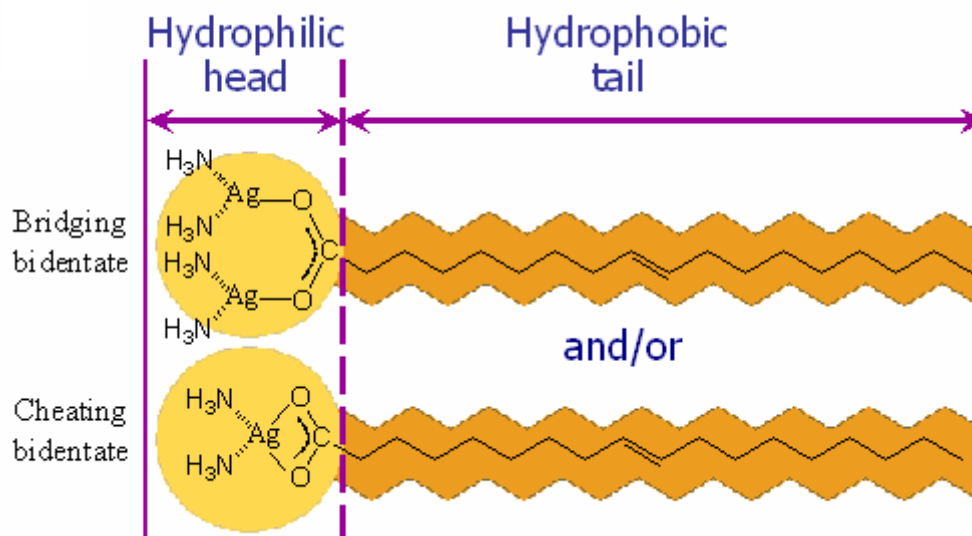


Figure 7.7 Coordination types of diamminesilver-(I) oleate.

## 7.4 Conclusions

A convenient approach to prepare Ag nanocables have been demonstrated by using the self-assembly of tubular diamminesilver-(I) oleate as templates. To obtain the well-defined nanocables, two steps are important. First, in the preparation of the diamminesilver-(I) oleate precursors, the molar ratio oleic acid/ $\text{Ag}^+$  must reach 50, so that ordered nanotubes with high aspect ratios can be formed. Second, in order to avoid fast nucleation resulting in the formation of spherical particles, the reduction conditions must be carefully controlled by the slow and dropwise addition of the reducing agent under gently shaking. The prepared nanotubes seem to have a multi wall structure. During the reduction, the intermediate state of stripe-arranged particles is formed at early stage, and finally leads to nanocables via Ostwald ripening and particle agglomeration. We believe that this approach could be extended to prepare a variety of metal nanocables by an appropriate choice of the inorganic/organic system and experimental conditions. In addition, metal nanowires also can be prepared by this method, since the organic sheath can be easily removed by dissolving in suitable organic solvents.

## References

---

- [180] A. M. Morales, C. M. Lieber, *Science* 1998, **279**, 208.
- [181] Y. Zhang, K. Suenaga, C. Colliex, S. Iijima, *Science* 1998, **281**, 973.
- [182] W. S. Shi, H. Y. Peng, L. Xu, N. Wang, Y. H. H. Tang, S. T. Lee, *Adv. Mater.* **2000**, *12*, 1927.
- [183] J. Q. Hu, X. M. Meng, Y. Jiang, C. S. Lee, S. T. Lee, *Adv. Mater.* 2003, **15**, 70.
- [184] Y. Yin, Y. Lu, Y. Sun, Y. Xia, *Nano Lett.* 2002, **2**, 427.
- [185] M. H. Huang, A. Choudrey, P. Yang, *Chem. Commun.* 2000, 1063.
- [186] Y. Xie, Z. Qiao, M. Chen, x. Liu, Y. Qian, *Adv. Mater.* 1999, **11**, 1512.
- [187] L. B. Luo, S. H. Yu, H. S. Qian, T. Zhou, *J. Am. Chem. Soc.* 2005, **127**, 2822.
- [188] J. Jang, B. Lim, J. Lee, T. Hyeon, *Chem. Commun.* 2001, 83.
- [189] M. Anderson, V. alfredsson, P. Kjelin, A. E. C. Palmqvist, *Nano Lett.* 2002, **2**, 1403.
- [190] Q. Wand, G. Wang, X. Han, X. Wang, J. G. Hou, *J. Phys. Chem. B* 2005, **109**, 23326.
- [191] T. A. Crowley, B. Daly, M. A. Morris, D. Ertz, O. Kazakova, J. J. Boland, B. Wu, J. D. Holmes, *J. Mater. Chem.* 2005, **15**, 2408.
- [192] K. Takahashi, Y. Wang, G. Cao, *J. Phys. Chem. B* 2005, **109**, 48.
- [193] S. H. Yu, X. Cui, L. Li, K. Li, B. Yu, M. Antonietti, *Adv. Mater.* 2004, **16**, 1636.
- [194] B. Yang, S. Kamiya, Y. Shimizu, N. Koshizaki, T. Shimizu, *Chem. Mater.* 2004, **16**, 2826.
- [195] D. Ugarte, W. A. de Heer, *Science* 1996, **274**, 1897.
- [196] N. R. Jana, *Small* 2005, **1**, 875.
- [197] J. H. Fuhrhop, D. Spiroski, C. Boettcher, *J. Am. Chem. Soc.* 1993, **115**, 1600.
- [198] D. H. Gary, D. L. Gin, *Chem. Mater.* 1998, **10**, 1827.
- [199] H. Qiu, M. Caffrey, *J. Phys. Chem. B* 1998, **102**, 4819.
- [200] G. John, M. Masuda, Y. Okada, K. Yase, T. Shimizu, *Adv. Mater.* 2001, **13**, 715.

# Summary

*Chapter 2* presents the study of a series of BAO-based PI-LED devices. These PIs exhibit obvious fluorescent property and the intensities decrease with increasing crystalline degree. It suggests that high crystalline degree would decrease the population of the imide rings-aminophenyl rings face-to-face stacking. Hence, the CT interactions and fluorescence intensity would be reduced. The resultant PIs not only can be a light-emitting layer in a single layer LED, but also act as an electron transport and an electron/hole blocking layer in a double layer PPV-PVA based LED. The incorporation of BAO-ODPA layer into the PPV-PVA LED provides a significant improvement in the EL efficiency by two orders of magnitude.

In *Chapter 3*, single layer PI-LEDs have been successfully prepared by vapor deposition polymerization from diamine BAO and BAPF with dianhydride 6FDA. Using VDP process, smoother surface morphology of the LED devices can be obtained than using wet coating process presented in *Chapter 2*. Effective active PI thin film can be performed as low as 150 Å and shows a low threshold voltage as 4.5V. Both BAO-6FDA and BAPF-6FDA single layer LED show broad EL spectra. Thicker PI film exhibits higher efficiencies in both types of LEDs. It could be resulted from the more CT sites in the thicker PI film in favor of increasing the intermolecular CT. BAPF-6FDA LED has a higher EL efficiency than BAO-6FDA LED because of the more balanced charge injection from both electrodes and the stronger intermolecular CT.

In *Chapter 4*, a series of thermal and mechanical properties of PI/ZnO nanohybrid films were established. The interchain hydrogen bonding being a kind of physical crosslinking exists in PI-ZnO interfacial domain. Owing to this physical crosslinking, the storage modulus, CTE decrement and  $T_g$  of the hybrid films can be

effectively improved in comparison with that of pure PI. The improvements on these characteristics of PMDA-ODA/ZnO nanohybrid films are much more significant than that of BTDA-ODA/ZnO nanohybrid film. The physical crosslinking structure also causes BTDA-ODA/ZnO nanohybrid films having two  $T_g$ s, one for pure PI domain, the other higher  $T_g$  for the PI-ZnO interfacial domain. PMDA-ODA/ZnO nanohybrid films have only one  $T_g$  because the PMDA-ODA having high  $T_g$  cause two possible  $T_g$ s into one. Although the  $T_d$ s of the hybrid films are lower than pure PI, it is good enough for the practical application. From TEM images, the ZnO particles show a uniform dispersion in the BTDA/ODA matrix, but most particles are bigger in size (10–15 nm) and some are elongated in comparison with as-synthetic TPM stabilized ZnO nanoparticle. It can be attributed to the high temperature and long time imidization process. However, the aggregation and irregular shape of ZnO nanoparticles are more notable in the PMDA-ODA/ZnO hybrid film. This means that the matrix structures significantly affect the morphology and characteristic of the PI/ZnO nanohybrid films.

*Chapter 5* describes preparation of ZnO nanocrystals by using a thermal coater and an air-circulating. An air-circulating provides a milder and rapid oxidized environment to develop ZnO crystals, so that flexible and thermal stable PI films can also be used as substrates in this process. HRTEM and PL measurements show the produced ZnO nanocrystals are nearly defect-free single crystalline structures. Besides, deposited ZnO on PI film substrates can obtain individual and well distribution nanocrystals after dispersing by an ultrasonic bath. Because a roll-type of PI film can be used as a substrate to deposit ZnO continually, it can be a simple and efficient method to fabricate ZnO nanocrystals on large scales.

In *Chapter 6* shows that the ternary system oleic acid/1-decanol/ammonium hydroxide exhibits an inverse hexagonal ( $H_{II}$ ) liquid crystalline phase, which is predominate at room temperature and exists in a wide compositional range. Polarized optical microscopy and x-ray diffraction confirms the formation of the hexagonal phase, while conductivity measurements reveal the inverse nature. The system can tolerate up to 45 wt-% of ammonium hydroxide before the hexagonal phase collapses. Using mixtures of ammonia and oleic acid to prepare *in situ* the oleate amphiphile is more convenient than using authentic alkali oleates. In particular, this allows for the incorporation of up to 100 mM solutions of metal ions such as  $Ag^+$ ,  $Cu^{2+}$ ,  $Ni^{2+}$ ,  $Co^{2+}$ ,  $Zn^{2+}$ , and  $Cd^{2+}$  into the confined aqueous phase due to the formation of ammine complexes. We expect that this inverse hexagonal system will serve as versatile tool for the preparation of nanorods and nanowires.

In *Chapter 7*, a convenient approach to prepare Ag nanocables have been demonstrated by using the self-assembly of tubular diamminesilver-(I) oleate as templates. To obtain the well-defined nanocables, two steps are important. First, in the preparation of the diamminesilver-(I) oleate precursors, the molar ratio oleic acid/ $\text{Ag}^+$  must reach 50, so that ordered nanotubes with high aspect ratios can be formed. Second, in order to avoid fast nucleation resulting in the formation of spherical particles, the reduction conditions must be carefully controlled by the slow and dropwise addition of the reducing agent under gently shaking. The prepared nanotubes seem to have a multi wall structure. During the reduction, the intermediate state of stripe-arranged particles is formed at early stage, and finally leads to nanocables via Ostwald ripening and particle agglomeration. We believe that this approach could be extended to prepare a variety of metal nanocables by an appropriate choice of the inorganic/organic system and experimental conditions. In addition, metal nanowires also can be prepared by this method, since the organic sheath can be easily removed by dissolving in suitable organic solvents.



## Publication

---

- [1] **S. C. Hsu**, W. T. Whang, S. C. Chen, " Electroluminescence characteristics of aromatic polyimides by vapor deposition polymerization", *Journal of Polymer Research* 2003, **10**, 7.
- [2] **S. C. Hsu**, W. T. Whang, C. H. Hung, P. C. Chiang, Y. N. Hsiao, " Effect of the polyimide structure and ZnO concentration on the morphology and characteristics of polyimide/ZnO nanohybrid films", *Macromolecular Chemistry and Physics* 2005, **206**, 291.
- [3] **S. C. Hsu**, W. T. Whang, C. H. Hung, " Large-scale fabrication of ZnO nanocrystals by a simple two-step evaporation oxidation approach", *Materials Characterization* (Accepted).



# Shou-Chian Hsu

---

National Chiao Tung University, Department of Materials Science and Engineering  
1001 TA HSUEH ROAD, HSINCHU, TAIWAN 30050, ROC  
Tel : +886-3-5712121 # 55347 E-mail : [u8818552.mse88g@nctu.edu.tw](mailto:u8818552.mse88g@nctu.edu.tw)

---

## EDUCATION

- **Doctor of Science**  
National Chiao Tung University - Hsinchu, Taiwan *Sep 2000 ~ Jul 2006*  
Major in materials science and engineering  
*(Exchange student to DWI an der Aachen, Germany, from Sep 2004 to Mar 2006)*
- **Master of Science** *Sep 1999 ~ Jun 2000*  
National Chiao Tung University - Hsinchu, Taiwan  
Major in materials science and engineering
- **Bachelor of Science** *Sep 1997 ~ Jun 1999*  
National Taiwan University of Science and  
Technology - Taipei, Taiwan  
Major in chemical engineering
- **Associate Degree** *Sep 1992 ~ Jun 1997*  
National I-Lan Institute of Technology - I-Lan, Taiwan  
Major in chemical engineering

## CAPABILITIES

- Synthesis of inorganic nanoparticles, nanorods and nanowires
- Design and preparation of organic/inorganic nanocomposites
- Fabrication of organic light-emitting devices
- Operation and maintenance of thermal coater and sputtering
- Work individually or as a team member in a laboratory setting
- Report research results in both Chinese and English written and oral forms

## CONFERENCES

- **Electronic Display Forum 2003** - Tokyo, Japan  
Co-sponsored by Japan Electronics and Information Technology Industries  
Association and Semiconductor Equipment and Materials International
- **The Development and Tread of OLED 2003** - Taipei, Taiwan  
Sponsored by Photonics Industry and Technology Development Association

- PROJECTS**
- Preparation of polymer/inorganic hybrid quantum dot laser 2003
  - Thin Film Polymer Light Emitting Laser 2002
  - Preparation and characteristic study of light-emitting aromatic polyimides 2000

**PhD THESIS**                      Synthesis and characterization of polyimide light-emitting diodes and nanocomposites

- PUBLICATIONS**
- Large-scale fabrication of ZnO nanocrystals by a simple two-step evaporation oxidation approach, *Materials Characterization* (Accepted).
  - Effect of the polyimide structure and ZnO concentration on the morphology and characteristics of polyimide/ZnO nanohybrid films, *Macromolecular Chemistry and Physics* 2005, **206**, 291.
  - Electroluminescence characteristics of aromatic polyimides by vapor deposition polymerization, *Journal of Polymer Research* 2003, **10**, 7.

- HONORS**
- The scholarship holder of the Carg foundation in Germany 2006
  - The president of Taiwanese Student Association in Aachen, Germany 2005
  - The scholarship holder of 2004 NSC-DAAD Sandwich Program 2004
  - Admission into PhD program after first academic year in mater program 2000